ScuDo
Scuola di Dottorato ~ Doctoral School
WHAT YOU ARE, TAKES YOU FAR

Doctoral Dissertation
Cotutelle Doctoral Program Between the Politecnico di Torino (Italy) and
Sharif University of Technology (Iran) in Mechanical Engineering

Solution of Coupled Thermoelasticity Problem in Rotating Disks

By

Ayoob Entezari

******

Supervisors:
Prof. Erasmo Carrera
Prof. Mohammad Ali Kouchakzadeh

Advisor:
Dr. Matteo Filippi

Doctoral Examination Committee:
Prof. Maria Cinefra, Referee, Politecnico di Torino, Italy.
Prof. Elvio Bonisoli, Referee, Politecnico di Torino, Italy.
Prof. Hassan Haddadpour, Referee, Sharif University of Technology, Iran.
Prof. Ali Hosseini Kordkheili, Referee, Sharif University of Technology, Iran.

Politecnico di Torino
2017

Declaration

I hereby declare that, the contents and organization of this dissertation constitute my own original work and does not compromise in any way the rights of third parties, including those relating to the security of personal data.

Ayoob Entezari
2017

* This dissertation is presented in partial fulfillment of the requirements for **Ph.D. degree** in the Graduate School of Politecnico di Torino (ScuDo).

I would like to dedicate this dissertation to my beloved wife, Elham, and my sweet daughter, Helena.

Acknowledgements

I would like to express my special appreciation and thanks to my supervisor Professor Dr. Erasmo Carrera, you have been a tremendous mentor for me. I would like to thank you for encouraging my research and for allowing me to grow as a visiting researcher. Your advice on both research as well as on my career have been priceless. I would also like to thank Dr. Matteo Filippi for your brilliant advice and comments. All of you have been there to support me for my Ph.D. dissertation.

Abstract

The main purpose of this dissertation is to study coupled thermoelastic behaviors in disks subjected to thermal shock loads based on the generalized and classic theories of coupled thermoelasticity. To this end, this research has been carried out in two stages.

In the first stage, thermoelasticity problems in an axisymmetric rotating disk with constant thickness made of a homogeneous isotropic material are analytically solved and closed-form formulations are presented for temperature and displacement fields. Since, the analytical solution is not always feasible, the finite element (FE) method can be employed for more sophisticated coupled thermoelasticity problems. Accordingly, in the second stage of the research, a novel refined 1D finite element approach with 3D-like accuracies are developed for theories of coupled thermoelasticity. Then, the developed FE models are applied for a 3D solution of the dynamic generalized coupled thermoelasticity problem in disks. Use of the reduced models with low computational costs may be of interest in a laborious time history analysis of the dynamic problems.

The obtained analytical and numerical solutions are in good agreement with the results available in the literature. It is further shown that the proposed analytical and FE methods are quite efficient with very high rate of convergence.

Contents

List of Figures

List of Tables

Chapter 1

Introduction

1.1 Rotating disk

Rotating disks subjected to thermal loads are widely used in many engineering fields such as aerospace, mechanical, naval, chemical plant, electronics, and biomaterials. Normally, these components can be manufactured by using any metal. However, for some specific applications such as in aerospace where light-weight and stiffness becomes necessary in high temperature environment, the components need to be made using special material such as a functionally graded material (FGM). For an example, in a turbine rotor, there is always a possibility that the heat from the external surface transmits to the shaft and from it to the bearings causing adverse effects on its functioning and efficiency.

In practical problems such as a realistic turbine rotor, usually, the disk profile is complex and designed as a combination of concave, convex and linear sections. In addition, there are other complex components such as shafts, air seals, spacers and blades along with the disks that represent extra distributed and concentrated loads on the disk surface. Moreover, in operation, when the rotating disk is exposed to a hot gas flow, there is a 3D temperature field on the disk, which can significantly affect the mechanical properties of the material.

Furthermore, in some of the applications, such as gas turbine engines, the disks may be subjected to sudden temperature changes in short periods of time as a result of start-up and shut-down procedures of the engines. These sudden changes in temperature can cause time dependent thermal stresses in the disks. Thermal stresses

due to large temperature gradients are higher than the steady-state stresses. These large stresses occur before reaching the steady-state condition. In such conditions, the disk should be designed with consideration of transient effects.

1.2 Theories of thermoelasticity

In the *static uncoupled thermoelasticity*, thermal effects on a body are restricted to strains due to a steady-state temperature distribution. As a more general theory of thermoelasticity, considering the transient heat conduction equation leads to time-dependent temperature distributions which can be used to obtain the transient thermal stresses. Such problems are called *quasi-static uncoupled thermoelasticity* problems. Alternatively, if external thermo-mechanical loads applied to the body vary adequately rapidly with the time so that inertia effects are excited, the inertia terms must be taken into account in the equations of motion. This theory is known as the *dynamic uncoupled thermoelasticity*. It is obvious that in all these theories, the temperature field is independently obtained from the heat conduction equation, while the displacement and stress fields are assumed to be dependent of the temperature.

When a structure is exposed to high-speed thermo-mechanical loads, the theories of uncoupled thermoelasticity may not provide entirely true physical behaviors. To avoid this drawback, interactions of the mechanical state of the elastic body on the temperature filed may be also simulated using the theories of *coupled thermoelasticity*. In these theories, the time derivatives of strain appear in the heat conduction equation so as to lead to the coupling between elasticity and energy equations. Accordingly, to find the solution for temperature and displacement fields and finally stresses, these coupled equations must be solved concurrently.

The thermoelasticity equations with the coupling effect was introduced by Duhamel [27] in 1837, for the first time, and then 120 years later, Biot [10], in 1956, presented the theory of classical thermoelasticity based on the principles of the irreversible thermodynamics. A history of thermoelasticity can be further found in the textbooks [11, 41].

Thus, under thermo-mechanical shock loading, the inertia and coupling effects can play important role in the thermoelastic behavior of a body. However, it has been shown that the coupling term may be more effective on the temperature and stress

distributions than the inertia term in such situations (see [11, 41]).
Applications of the coupled thermoelasticity in advanced structural design problems have attracted the attention of many researchers during the second half of the last century. These applications can range from aerospace structures to fast-burst reactors, pulsed lasers, and particle accelerators which can supply sudden heat pulses in extremely short periods of time [8]. For instance, in ultra-fast pulsed lasers which is employed for nondestructive detection [12], measurement of material properties [44] and micro-machining [66], the heat pulse may be imposed in an order of Picosecond or less. The nature of the heat transfer mechanism instantaneously after the imposition of the pulse and the resulting temperature distribution at the surface of the body are some matters of interest in such applications.
Due to the parabolic nature of the heat conduction equation in the classical theory of thermoelasticity, the thermal disturbances are predicted to propagate with infinite speed through the elastic body. This prediction may be sufficiently accurate for most engineering applications. However, it is not physically realistic and acceptable in some practical problems involving high thermal loads at extremely short time intervals or very low temperatures near the absolute zero. Indeed, in such cases, the classical theory is not well able to detect thermal wave disturbances (see [22]).
To overcome this drawback, several non-classical models of the coupled thermoelasticity with the finite speed of the thermal wave propagation were introduced. Typically, these models are known as the *generalized theories of thermoelasticity*. Among these theories, Lord-Shulman (LS), Green-Lindsay (GL) and Green-Naghdi (GN) are the most well-known models. The detailed discussions of the generalized thermoelasticity with finite wave speeds have been presented in [45].

1.3 Literature review

In general, analytical solutions of the coupled thermoelasticity problems are mathematically laborious, so that many simplifying assumptions may be required to achieve a closed form solution for such problems. A survey of the literature indicates that the number of articles using analytical methods to solve the problems is limited. Most of the analytical studies are restricted to the basic problems such as the infinite space, half-space and layer, where the boundary conditions are simple

(see [39, 58]). For some bounded problems with simple initial and boundary conditions, analytical solutions of the coupled thermoelastic equations have been reported by a few investigators. Among them it may be referred to the exact solutions for beam [29], and rectangular plate [47] problems, as well as a one-dimensional (1D) axisymmetric solution for spherical [57] and cylindrical [42] problems.

Indeed, the exact solution for more sophisticated geometries and boundary conditions as well as for all theories of coupled thermoelasticity is not available in the literature. Accordingly, the development of alternative solution techniques including semi-analytical and numerical methods has been essential. In order to obtain numerical solution of the coupled thermoelastic problems, the finite difference (FD), the finite element (FE) and the boundary element (BE) methods have been used. Among the procedures, however, the FE method is more widely employed for this class of problems due to the adaptability of this method.

The finite element formulation of the thermoelasticity problems can be derived from the variational approach and the weighted residual techniques. For elastic continuum, the variational approach is based on the application of variational calculus, which deals with the extremization of the total potential and kinetic energies, while in the weighted residual methods; the governing equations are multiplied by a weighting function and then averaged over the domain.

In the beginning, based on the variational principle, Wilson and Nickell [64] developed FE formulations for the heat conduction equation without the mechanical coupling term, and Fujino and Ohsaka [37] presented a FE solution to static uncoupled thermoelasticity problems. Later, Nickell and Sackman [52] further presented FE formulations through the variational approach to solve the coupled thermoelastic equations in a half-space problem. A complete discussion of the variational approach used to thermoelasticity has been presented in the book by Hetnarski and Ignaczak [40].

On the other hand, the weighted residual methods along with an unconditionally stable implicit-explicit procedure were employed to the dynamic coupled thermoelasticity problem by Liu and Chang [50]. Furthermore, Eslami and Salehzadeh [31] applied the weighted residual method based on Galerkin technique to develop a finite element formulation for coupled thermoelasticity. Then, this formulation was employed to solve a 1D rod problem by Eslami and Vahedi [34].

Due to the contentious definition of functional for the first law thermodynamics, in deriving the coupled thermoelastic equations by the variational calculus approach,

some drawbacks may be incurred. However, the weighted residual techniques such as Galerkin method which convert directly the governing equations to a weak formulation are quite efficient in the convergence rate compared to the conventional method [41].

Although the present dissertation is not a review study, but in the following, it attempts to survey a number of articles in which the FE method has been used to solve the transient thermoelasticity problems. It should be also noted that the following papers are listed in chronological order and essentially, more emphasis is on the type of problem solved by researchers.

The coupled thermoelastic problem in a long cylinder exposed to a specified thermomechanical boundary conditions was solved by Li *et al.* [48]. They used several different techniques for the spatial and time discretization in the FE method to demonstrate the proper numerical techniques for this problem. Carter and Booker [19] also solved the 1D classical coupled thermoelastic equations for an infinite cylinder. However, all these studies had been done assuming that the thermal disturbances propagate with infinite speed in the elastic medium.

A FE formulation of GL thermoelasticity model was presented by Prevost and Tao [54]. They applied an implicit-explicit scheme to solve the equations for a semi-infinite slab problem subject to surface thermal load. Chen and Weng [23] proposed a transfinite element method, in which the combination of the FE method and Laplace transform technique is employed, to analyze the generalized coupled thermoelasticity problems based on LS, GL and GN models. That is, the problems can be solved in the Laplace transform domain by the FE method and then the transformed solution are numerically inverted to find the physical time domain response. Using this approach, Chen and Weng presented solutions for the cylinder with infinite length and layer problems in [23].

Farhat *et al.* [35] obtained the FE equations for the classical coupled thermoelasticity by Galerkin method and then proposed an implicit-implicit staggered technique to solve the equations. In this paper, the accuracy of the proposed algorithm has been demonstrated by solving half-space and infinitely long shaft problems. Likewise, the FE method along with an explicit time integration architecture were applied by Tamma and Namburu [59] to solve the GL thermoelasticity problem in an 1D half-space.

For a hollow sphere problem subjected to specified boundary conditions, Eslami and Vahedi [32] presented the FE formulation of the classical coupled thermoelas-

ticity under spherical symmetry condition by using Galerkin method. Eslami *et al*. [33] studied the coupled thermoelastic behavior of an axially symmetric cylindrical shell, as well. In these studies, the FE equations were solved by a time marching technique. In addition, using an axisymmetric FE formulation, the coupled thermoelastic response of a functionally graded cylinder subjected to specified boundary conditions was investigated by Reddy and Chin [55].

Cannarozzi and Ubertini [13] derived a variational form of the coupled quasi-static thermoelasticity, in which the elastic equation is stated as the hybrid stress formulation while the mixed flux-temperature formulation is used for the heat equation. In the FE implementation, they developed three quadrilateral elements and assessed characteristics of the proposed approach through some numerical test cases. Based on the first-order shear deformation theory, Chakraborty *et al*. [21] presented a FE formulation for dynamic uncoupled thermoelasticity in functionally graded beam structures. In this paper, a beam element was developed to obtain a convergence stiffness matrix and eliminate the shear locking effect of the element. In addition, Chakraborty and Gopalakrishnan [20] investigated generalized thermoelastic responses in an anisotropic layered medium based on LS and GL theories. They used the spectral FE method to capture the propagation of thermoelastic waves inside the medium.

In a series of papers, using Galerkin FE method, Eslami *et al*. rendered a 1D classical and generalized thermoelasticity solution for annular isotropic [4] and functionally graded [7] disk problems, functionally graded layer problems [5], functionally graded sphere problems [6] and functionally graded beams [3]. These authors employed the same procedure as proposed by [23] to obtain the solutions.

In addition, the magneto-thermoelastic behavior of a semi-infinite plate subjected to a magnetic and a thermal shock was investigated by Tian and Shen [60]. They considered the GL model as the generalized thermoelasticity theory and solved the dynamic FE equations directly in time-domain. Abbas *et al*. presented generalized thermoelastic solutions for axisymmetric cylinder [1] and half-space [2] problems based on the LS and GL models. In these studies, the weak formulations were obtained by Galerkin finite element method and then the Newmark time integration scheme was employed to solve the equations. The thermoelastic response of a 1D layered region subjected to thermal shock load was analyzed by Hosseini Zad [43] based on the different theories of coupled thermoelasticity. Darabseh *et al*. [26] considered the coupled thermoelastic problem in a functionally graded

thick hollow cylinder under thermal loading. These authors used the GL theory of thermoelasticity and solved the governing equations by using Galerkin FE method. Galerkin FE method along with a traditional time domain integral method were employed by Guo [38] to solve the LS coupled thermoelastic problems in one- and two-dimensional models. Based on the LS and GL generalized theories, Filopoulos *et al*. [36] derived coupled thermoelastic models for nonlocal thermo-mechanical problems in micro-structures. Moreover, they solved a 1D slender bar problem to demonstrate how their models work.

The generalized coupled thermoelastic problem in an axisymmetric infinite cylinder subjected to specified boundary conditions was analyzed by Zenkour and Abbas [65] based on LS theory. In this paper, the transient solution of the FE equations was evaluated directly from the model at any time. The classical coupled thermoelastic problem in a plate subjected to a hypersonic re-entry flow was analyzed by Li *et al*. [49]. They employed the Newmark method and Crank-Nicolson scheme to discretize the equation of motion and heat conduction equation in the time domain, respectively. In this paper, the Rayleigh damping was taken into account in the equation of motion as well.

Furthermore, the effect of material microstructure on the classic coupled thermoelastic behavior in a 1D half-space was studied by Papathanasiou *et al*. [53]. These investigators used the gradient elasticity theory to model the microstructure influences and applied the FE and time integration methods to solve the governing equations. The classical coupled thermoelastic response in a functionally graded annular plate imposed to lateral thermal shock load was investigated by Jafarinezhad and Eslami [46]. In this paper, the first order shear deformation plate theory was used to obtain the equations of motion and the temperature distribution across the thickness was be approximated by a second order polynomial. These authors utilized the same procedure as used in [3–7, 23].

Analysis of the works reviewed above concerning solution of the coupled thermoelasticity problems may lead to the following inferences

- Due to use of the coupled thermoelasticity theories in advanced structural design, they are still topics of active research.
- The major presented studies deal with the coupled thermoelasticity response in the basic problems including an infinite medium, a half-space and a layer as well as in the axisymmetric problems. Moreover, two- or three-dimensional

coupled thermoelastic solutions for some simple problems may be found in just a few number of articles.

- analytical solution of the coupled thermoelasticity problem in the disks has never before been presented.
- After over half a century of application of FE method in thermoelasticity, this method is still applied as a powerful numerical tool in such problems.
- Most of the investigators applied Galerkin technique to the governing equations to obtain a weak formulation of the problem, especially for the theories of generalized thermoelasticity.

1.4 Objectives and scope of research

The main objective of this dissertation is to study coupled thermoelastic behaviors in disks subjected to thermal shock loads based on the generalized and classic theories of coupled thermoelasticity. To this end, this research has been carried out in two stages. In the first stage, thermoelasticity problems in a rotating disk are analytically solved. In the second stage of the research, a novel refined 1D finite element approach with 3D capabilities are developed and employed for more sophisticated problems in which the analytical solution is not always possible.
Thus, the dissertation has been organized as follows. In Chapter 2, thermoelasticity problems in an axisymmetric rotating disk with constant thickness made of a homogeneous isotropic material are analytically solved. In this chapter, based on the classical and generalized coupled theories, and dynamic and quasi-static uncoupled theories, closed-form formulations are presented for temperature and displacement fields. In Chapter 3, a 1D refined FE method in the Carrera Unified formulation (CUF) framework is used for static structural analysis of rotors and rotating disks with variable thickness. Chapter 4 presents 1D FE-CUF approach for the generalized coupled thermoelasticity problems. Chapter 5 provides some numerical evaluations related to the proposed FE formulation for the coupled thermoelastic problems and finally Chapter 6 gives a summary of conclusion.

Chapter 2

Analytical solution of coupled thermoelasticity problems in disks

In this chapter, the coupled and uncoupled thermoelasticity problems for a rotating disk subjected to thermal and mechanical shock loads are analytically solved. Axisymmetric thermal and mechanical boundary conditions are considered in general forms of arbitrary heat transfer and traction, respectively, at the inner and outer radii of the disk. To solve the thermoelasticity problems based on the classical and generalized coupled theories, and dynamic and quasi static uncoupled theories, an analytical procedure based on the Fourier-Bessel transform is employed. Then, closed-form formulations are presented for temperature and displacement fields.

2.1 Governing equations

Consider an annular rotating disk, made of isotropic material, under axisymmetric thermal and mechanical shock loads applied to its inner or outer radii. The equation of motion in radial direction for the rotating disk with constant thickness can be written as [41]

$$\frac{\partial \sigma_{rr}}{\partial r} + \frac{1}{r}(\sigma_{rr} - \sigma_{\theta\theta}) + \rho r \omega^2 = \rho \frac{\partial^2 u}{\partial t^2} \tag{2.1}$$

where σ_{rr} and $\sigma_{\theta\theta}$ are radial and tangential stress components, r is radial coordinate, ρ is density, ω is constant angular velocity of the rotating disk, and t is the time variable. The relations between the radial displacement u and the strains are

$$\varepsilon_{rr} = \frac{\partial u}{\partial r} \quad , \quad \varepsilon_{\theta\theta} = \frac{u}{r} \tag{2.2}$$

where ε_{rr} and $\varepsilon_{\theta\theta}$ are the radial and tangential strain components, respectively. The stress components for the plane stress state, according to Hooke's law are

$$\begin{aligned} \sigma_{rr} &= \left(2\mu + \tilde{\lambda}\right)\varepsilon_{rr} + \tilde{\lambda}\,\varepsilon_{\theta\theta} - \tilde{\beta}T \\ \sigma_{\theta\theta} &= \tilde{\lambda}\,\varepsilon_{rr} + \left(2\mu + \tilde{\lambda}\right)\varepsilon_{\theta\theta} - \tilde{\beta}T \end{aligned} \tag{2.3}$$

Here, T is the temperature change and $\tilde{\lambda}$ and $\tilde{\beta}$ are obtained as

$$\tilde{\lambda} = \frac{2\mu}{\lambda + 2\mu}\lambda \quad , \quad \tilde{\beta} = \frac{2\mu}{\lambda + 2\mu}\left(3\lambda + 2\mu\right)\alpha \tag{2.4}$$

where λ and μ are Lame constants, and α is the coefficient of linear thermal expansion. Equations (2.1) to (2.3) may be combined to yield the equation of motion in term of the displacement component as

$$\left\{\left(\tilde{\lambda} + 2\mu\right)\left[\frac{\partial^2}{\partial r^2} + \frac{1}{r}\frac{\partial}{\partial r} - \frac{1}{r^2}\right] - \rho\frac{\partial^2}{\partial t^2}\right\}u - \tilde{\beta}\frac{\partial T}{\partial r} = -\rho r\omega^2 \tag{2.5}$$

For the axisymmetric problem, the classical coupled heat conduction equation in polar coordinates in the absence of heat source is obtained to be

$$\left\{\kappa\left[\frac{\partial^2}{\partial r^2} + \frac{1}{r}\frac{\partial}{\partial r}\right] - \rho c\frac{\partial}{\partial t}\right\}T - \tilde{\beta}T_0\left\{\frac{\partial^2}{\partial r\partial t} + \frac{1}{r}\frac{\partial}{\partial t}\right\}u = 0 \tag{2.6}$$

where κ, c and T_0 are the thermal conductivity, specific heat and reference temperature, respectively.

Equations (2.5) and (2.6) constitute the governing coupled system of equations for the classical theory of thermoelasticity in the problem of isotropic rotating disk with constant thickness.

The classical coupled theory of thermoelasticity is based on the conventional energy equation (Eq. (2.6)). The parabolic nature of the energy equation in this theory, leads to the prediction of infinite propagation speeds for the thermal distur-

bances. This prediction is physically unrealistic and problems arise when we deal with special applications involving very short transient durations and sudden mechanical and thermal shock loads. On this basis, some modified coupled thermoelasticity models with the finite speed of wave propagation such as Lord-Shulman (LS), Green-Lindsay (GL), and Green–Naghdi (GN) theories have been proposed. The generalized coupled heat conduction equation based on the LS theory for the axisymmetric problem in the absence of heat source is

$$\begin{array}{l} \left\{\kappa\left[\frac{\partial^2}{\partial r^2}+\frac{1}{r}\frac{\partial}{\partial r}\right]-\rho c\frac{\partial}{\partial t}\left(1+t_0\frac{\partial}{\partial t}\right)\right\}T \\ -\tilde{\beta}T_0\left\{t_0\left[\frac{\partial^3}{\partial r\partial t^2}+\frac{1}{r}\frac{\partial^2}{\partial t^2}\right]+\frac{\partial^2}{\partial r\partial t}+\frac{1}{r}\frac{\partial}{\partial t}\right\}u=0 \end{array} \tag{2.7}$$

where t_0 is relaxation time associated with LS model. The relaxation time represents the time-lag needed to establish steady state heat conduction in an element of volume when a temperature gradient is suddenly imposed on the element. Equations (2.5) and (2.7) are the governing equations of the generalized coupled thermoelasticity based on LS model in the problem of isotropic rotating disk with constant thickness.

For the coupled equations (2.5) and (2.7), The general forms of thermal and mechanical boundary conditions can be considered as heat transfer and traction, respectively, at the inner and outer radii of the disk as follows

$$\begin{array}{l} k_{11}\left.\frac{\partial T}{\partial r}\right|_{r=r_i}+k_{12}T(r_i,t)=f_1(t)\ \ ,\ \ k_{21}\left.\frac{\partial T}{\partial r}\right|_{r=r_o}+k_{22}T(r_o,t)=f_2(t) \\ k_{31}\left.\frac{\partial u}{\partial r}\right|_{r=r_i}+k_{32}u(r_i,t)=f_3(t)\ \ ,\ \ k_{41}\left.\frac{\partial u}{\partial r}\right|_{r=r_o}+k_{42}u(r_o,t)=f_4(t) \end{array} \tag{2.8}$$

where r_i and r_o are the inner and outer radii of the disk, respectively. $f_1(t)$ to $f_4(t)$ are time dependent known functions applied to the inner and outer radii. k_{ij} are constant thermal and mechanical parameters related to the conduction and convection coefficients, and mechanical properties. In general, following initial conditions may be assumed for the coupled equations (2.5) and (2.7)

$$\begin{array}{ll} T(r,0)=g_1(r), & \dot{T}(r,0)=g_2(r) \\ u(r,0)=g_3(r), & \dot{u}(r,0)=g_4(r) \end{array} \tag{2.9}$$

Here $g_1(r)$ to $g_4(r)$ are known functions of the space coordinate r. The superscript dot $(\cdot)$ denotes the differentiation with respect to time.

The governing equations may be introduced in nondimensional form for simplicity.

The nondimensional parameters are defined as

$$\begin{array}{lll} \hat{r}=\frac{r}{l}, & \hat{t}=\frac{tV_e}{l}, & \hat{t}_0=\frac{t_0V_e}{l} \\ \hat{\sigma}_{rr}=\frac{\sigma_{rr}}{\tilde{\beta}T_0}, & \hat{\sigma}_{\theta\theta}=\frac{\sigma_{\theta\theta}}{\tilde{\beta}T_0}, & \hat{T}=\frac{T}{T_0} \\ \hat{u}=\frac{(\tilde{\lambda}+2\mu)u}{l\tilde{\beta}T_0}, & \hat{\omega}=\sqrt{\frac{\rho l^2}{\tilde{\beta}T_0}}\omega & \end{array} \tag{2.10}$$

where $l=\kappa/\rho cV_e$ and $V_e=\sqrt{(\tilde{\lambda}+2\mu)/\rho}$ represent the unit length and the speed of elastic wave propagation, respectively. The hat values indicate nondimensional parameters. Using the nondimensional parameters, the governing coupled system of Eqs. (2.5) and (2.7), and stress-displacement relations take the form

$$\begin{array}{l} \left\{\frac{\partial^2}{\partial\hat{r}^2}+\frac{1}{\hat{r}}\frac{\partial}{\partial\hat{r}}-\frac{\partial}{\partial\hat{t}}\left(1+\hat{t}_0\frac{\partial}{\partial\hat{t}}\right)\right\}\hat{T} \\ -C\left\{\hat{t}_0\left[\frac{\partial^3}{\partial\hat{r}\partial\hat{t}^2}+\frac{1}{\hat{r}}\frac{\partial^2}{\partial\hat{t}^2}\right]+\frac{\partial^2}{\partial\hat{r}\partial\hat{t}}+\frac{1}{\hat{r}}\frac{\partial}{\partial\hat{t}}\right\}\hat{u}=0 \end{array} \tag{2.11}$$

$$\left\{\frac{\partial^2}{\partial\hat{r}^2}+\frac{1}{\hat{r}}\frac{\partial}{\partial\hat{r}}-\frac{1}{\hat{r}^2}-\frac{\partial^2}{\partial\hat{t}^2}\right\}\hat{u}-\frac{\partial\hat{T}}{\partial\hat{r}}=-\hat{r}\hat{\omega}^2 \tag{2.12}$$

$$\begin{array}{l} \hat{\sigma}_{rr}=\frac{\partial\hat{u}}{\partial\hat{r}}+\frac{\tilde{\lambda}}{(\tilde{\lambda}+2\mu)}\frac{\hat{u}}{\hat{r}}-\hat{T} \\ \hat{\sigma}_{\theta\theta}=\frac{\tilde{\lambda}}{(\tilde{\lambda}+2\mu)}\frac{\partial\hat{u}}{\partial\hat{r}}+\frac{\hat{u}}{\hat{r}}-\hat{T} \end{array} \tag{2.13}$$

where $C=T_0\tilde{\beta}^2/\rho c(\tilde{\lambda}+2\mu)$ is called the thermoelastic coupling (or damping) parameter. For a certain isotropic material, the thermoelastic coupling parameter is a function of the reference temperature T_0.

From nondimensional Eqs. (2.11) and (2.12), the thermal disturbances propagate with the speed of $V_t=\sqrt{1/\hat{t}_0}$ and the speed of propagation of the elastic disturbances is unity. The value of V_t is finite for the Lord–Shulman theory. When the relaxation time is zero, the system of Eqs. (2.11) and (2.12) reduces to that of the classical coupled thermoelasticity which predicts an infinite speed of propagation of thermal disturbances.

The boundary and initial conditions (2.8) and (2.9) in terms of the nondimensional

parameters can be written in the form

$$\begin{aligned}
&\hat{k}_{11}\left.\frac{\partial \hat{T}}{\partial \hat{r}}\right|_{\hat{r}=a}+\hat{k}_{12}\hat{T}(a,t)=\hat{f}_1(\hat{t})\\
&\hat{k}_{21}\left.\frac{\partial \hat{T}}{\partial \hat{r}}\right|_{\hat{r}=b}+\hat{k}_{22}\hat{T}(b,t)=\hat{f}_2(\hat{t})\\
&\hat{k}_{31}\left.\frac{\partial \hat{u}}{\partial \hat{r}}\right|_{\hat{r}=a}+\hat{k}_{32}\hat{u}(a,t)=\hat{f}_3(\hat{t})\\
&\hat{k}_{41}\left.\frac{\partial \hat{u}}{\partial \hat{r}}\right|_{\hat{r}=b}+\hat{k}_{42}\hat{u}(b,t)=\hat{f}_4(\hat{t})\\
&\hat{T}(\hat{r},0)=\hat{g}_1(\hat{r}),\quad \dot{\hat{T}}(\hat{r},0)=\hat{g}_2(\hat{r})\\
&\hat{u}(\hat{r},0)=\hat{g}_3(\hat{r}),\quad \dot{\hat{u}}(\hat{r},0)=\hat{g}_4(\hat{r})
\end{aligned}\tag{2.14}$$

Here a and b are the nondimensional inner and outer radii, respectively. The hat values are nondimensional parameters that are defined as

$$\begin{aligned}
&\hat{k}_{11}=\tfrac{k_{11}}{\kappa}, && \hat{k}_{12}=\tfrac{k_{12}l}{\kappa}, && \hat{f}_1(\hat{t})=\tfrac{l f_1(t)}{\kappa T_0}\\
&\hat{k}_{21}=\tfrac{k_{21}}{\kappa}, && \hat{k}_{22}=\tfrac{k_{22}l}{\kappa}, && \hat{f}_2(\hat{t})=\tfrac{l f_2(t)}{\kappa T_0}\\
&\hat{k}_{31}=\tfrac{k_{31}}{(\tilde{\lambda}+2\mu)}, && \hat{k}_{32}=\tfrac{k_{32}l}{(\tilde{\lambda}+2\mu)}, && \hat{f}_3(\hat{t})=\tfrac{f_3(t)}{\beta T_0}\\
&\hat{k}_{41}=\tfrac{k_{41}}{(\tilde{\lambda}+2\mu)}, && \hat{k}_{42}=\tfrac{k_{42}l}{(\tilde{\lambda}+2\mu)}, && \hat{f}_4(\hat{t})=\tfrac{f_4(t)}{\beta T_0}\\
&\hat{g}_1(\hat{r})=\tfrac{g_1(r)}{T_0}, && \hat{g}_2(\hat{r})=\tfrac{l g_2(r)}{T_0 V_e}\\
&\hat{g}_3(\hat{r})=\tfrac{(\tilde{\lambda}+2\mu)g_3(r)}{l\beta T_0}, && \hat{g}_4(\hat{r})=\tfrac{(\tilde{\lambda}+2\mu)g_4(r)}{\beta T_0 V_e}
\end{aligned}\tag{2.15}$$

As is evident from Eqs. (2.11) and (2.12), The theories of coupled thermoelasticity take into account the time rate of change of the first invariant of strain tensor in the first law of thermodynamics causing the coupling between elasticity and energy equations. This situation occurs when the rate of application of a thermo-mechanical load is rapid enough to produce thermal stress waves. To obtain the solution for temperature and displacements and finally the stresses, these coupled equations must be solved simultaneously.

If the time rate of change of imposed thermo-mechanical loads is not large enough to excite the thermal stress wave propagation, the effect of coupling term in the energy equation (2.11) can be negligible. In this case, the energy equation of the classical coupled theory reduces to

$$\left\{\frac{\partial^2}{\partial \hat{r}^2}+\frac{1}{\hat{r}}\frac{\partial}{\partial \hat{r}}-\frac{\partial}{\partial \hat{t}}\right\}\hat{T}=0 \tag{2.16}$$

Equations (2.12) and (2.16) are the governing equations of the dynamic uncoupled thermoelasticity for the rotating disk.
In most practical engineering problems the imposed thermo-mechanical load is vary sufficiently slowly with the time so as not to excite inertia effects. Such problems are called quasi-static. Neglecting the inertia term, the equation of motion (2.12) reduces to

$$\left\{\frac{\partial^2}{\partial \hat{r}^2}+\frac{1}{\hat{r}}\frac{\partial}{\partial \hat{r}}-\frac{1}{\hat{r}^2}\right\}\hat{u}-\frac{\partial \hat{T}}{\partial \hat{r}}=-\hat{r}\hat{\omega}^2 \tag{2.17}$$

Therefore, the quasi-static uncoupled thermoelasticity problem in the rotating disk can be described by Eqs. (2.16) and (2.17). For a steady-state condition the heat conduction Eq. (2.16) is further reduced to

$$\left\{\frac{\partial^2}{\partial \hat{r}^2}+\frac{1}{\hat{r}}\frac{\partial}{\partial \hat{r}}\right\}\hat{T}=0 \tag{2.18}$$

This equation along with the imposed boundary conditions fully defines the field of temperature distribution in the disk for the steady state.

2.2 Solution of coupled thermoelasticity

The governing Equations (2.11) and (2.12) are a system of second order linear partial differential equations (PDE) with nonconstant (radius dependent) coefficients subjected to the nonhomogeneous initial and boundary conditions. These equations can be solved using the analytical method based on the finite Hankel transform, which can change the partial differential equations into solvable ordinary differential equations. To this end, first, the principle of superposition can be used to simplify the coupled initial-boundary value problem (IBVP) into simpler sub-IBVPs.
Therefore, using the principle of superposition, the heat conduction Equation (2.11) along with the corresponding boundary and initial conditions (2.14) in terms of the nondimensional parameters (without the hat sign for convenience), can be decomposed into two following sub-IBVPs

$$\begin{aligned}
&\tfrac{\partial^2 T_1}{\partial r^2}+\tfrac{1}{r}\tfrac{\partial T_1}{\partial r}-\dot{T}_1-t_0\ddot{T}_1=0\\
&k_{11}\tfrac{\partial T_1}{\partial r}\Big|_{r=a}+k_{12}T_1(a,t)=f_1(t)\ ,\quad k_{21}\tfrac{\partial T_1}{\partial r}\Big|_{r=b}+k_{22}T_1(b,t)=f_2(t)\\
&T_1(r,0)=0\ ,\ \dot{T}_1(r,0)=0
\end{aligned} \tag{2.19}$$

$$\begin{aligned}
&\tfrac{\partial^2 T_2}{\partial r^2}+\tfrac{1}{r}\tfrac{\partial T_2}{\partial r}-\dot{T}_2-t_0\ddot{T}_2=C\left\{t_0\left(\ddot{u}_{,r}+\tfrac{\ddot{u}}{r}\right)+\dot{u}_{,r}+\tfrac{\dot{u}}{r}\right\}\\
&k_{11}\left.\tfrac{\partial T_2}{\partial r}\right|_{r=a}+k_{12}T_2(a,t)=0\ \ ,\ \ k_{21}\left.\tfrac{\partial T_2}{\partial r}\right|_{r=b}+k_{22}T_2(b,t)=0\\
&T_2(r,0)=g_1(r)\ \ ,\ \ \dot{T}_2(r,0)=g_2(r)
\end{aligned}\tag{2.20}$$

Note that in the first sub problem, the PDE is homogeneous while the boundary and initial conditions are nonhomogeneous and homogeneous, respectively. In the second sub problem, the PDE is nonhomogeneous and may include the coupled terms while the boundary and initial conditions are homogeneous and nonhomogeneous, respectively. Similarly, Eqs. (2.12) and (2.14) may be decomposed into two following sub-IBVPs

$$\begin{aligned}
&\tfrac{\partial^2 u_1}{\partial r^2}+\tfrac{1}{r}\tfrac{\partial u_1}{\partial r}-\tfrac{u_1}{r^2}-\ddot{u}_1=0\\
&k_{31}\left.\tfrac{\partial u_1}{\partial r}\right|_{r=a}+k_{32}u_1(a,t)=f_3(t)\ \ ,\ \ k_{41}\left.\tfrac{\partial u_1}{\partial r}\right|_{r=b}+k_{42}u_1(b,t)=f_4(t)\\
&u_1(r,0)=0\ \ ,\ \ \dot{u}_1(r,0)=0
\end{aligned}\tag{2.21}$$

$$\begin{aligned}
&\tfrac{\partial^2 u_2}{\partial r^2}+\tfrac{1}{r}\tfrac{\partial u_2}{\partial r}-\tfrac{u_2}{r^2}-\ddot{u}_2=T_{,r}-r\omega^2\\
&k_{31}\left.\tfrac{\partial u_2}{\partial r}\right|_{r=a}+k_{32}u_2(a,t)=0\ \ ,\ \ k_{41}\left.\tfrac{\partial u_2}{\partial \hat{r}}\right|_{r=b}+k_{42}u_2(b,t)=0\\
&u_2(r,0)=g_3(r)\ ,\ \dot{u}_2(r,0)=g_4(r)
\end{aligned}\tag{2.22}$$

The final solution for the temperature and displacement fields is obtained from total of two solutions of these sub-IBVPs as follows

$$T(r,t)=T_1(r,t)+T_2(r,t)\ \ ,\ \ u(r,t)=u_1(r,t)+u_2(r,t)\tag{2.23}$$

where, The solutions of homogeneous equation corresponding to heat conduction and motion equations are shown by $T_1(r,t)$ and $u_1(r,t)$, respectively. $T_2(r,t)$ and $u_2(r,t)$ are solutions of nonhomogeneous form of heat conduction and motion equations, respectively.

Equations (2.19) and (2.21) are called Bessel equations and can be separately solved using finite Hankel transform. Using the definition of the finite Hankel transform, the transformed temperature and displacement can expressed as

$$\begin{aligned}
&\mathscr{H}[T_1(r,t)]=\overline{T}_1(t,\xi_m)=\textstyle\int_a^b rT_1(r,t)K_0(r,\xi_m)dr\\
&\mathscr{H}[u_1(r,t)]=\overline{u}_1(t,\eta_n)=\textstyle\int_a^b ru_1(r,t)K_1(r,\eta_n)dr
\end{aligned}\tag{2.24}$$

Here $K_0(r,\xi_m)$ and $K_1(r,\eta_n)$ are the kernel functions related to Eqs. (2.19) and (2.21), respectively, and result in the following relations [25]

$$\begin{aligned} K_0(r,\xi_m) = J_0(\xi_m r)\left(k_{21}\left.\frac{\partial Y_0(\xi_m r)}{\partial r}\right|_{r=b} + k_{22}Y_0(\xi_m b)\right) \\ -Y_0(\xi_m r)\left(k_{21}\left.\frac{\partial J_0(\xi_m r)}{\partial r}\right|_{r=b} + k_{22}J_0(\xi_m b)\right) \end{aligned} \tag{2.25}$$

$$\begin{aligned} K_1(r,\eta_n) = J_1(\eta_n r)\left(k_{41}\left.\frac{\partial Y_1(\eta_n r)}{\partial r}\right|_{r=b} + k_{42}Y_1(\eta_n b)\right) \\ -Y_1(\eta_n r)\left(k_{41}\left.\frac{\partial J_1(\eta_n r)}{\partial r}\right|_{r=b} + k_{42}J_1(\eta_n b)\right) \end{aligned} \tag{2.26}$$

where $J_\nu(\xi_m r)$ and $Y_\nu(\xi_m r)$ (or $J_\nu(\eta_n r)$ and $Y_\nu(\eta_n r)$ are the Bessel functions of the first and second kind, and of order ν,($\nu = 0$ and 1). ξ_m and η_n are positive roots of the following equations, respectively [25]

$$\begin{aligned} &\left(k_{11}\left.\frac{\partial Y_0(\xi_m r)}{\partial r}\right|_{r=a} + k_{12}Y_0(\xi_m a)\right)\left(k_{21}\left.\frac{\partial J_0(\xi_m r)}{\partial r}\right|_{r=b} + k_{22}J_0(\xi_m b)\right) \\ &-\left(k_{21}\left.\frac{\partial Y_0(\xi_m r)}{\partial r}\right|_{r=b} + k_{22}Y_0(\xi_m b)\right)\left(k_{11}\left.\frac{\partial J_0(\xi_m r)}{\partial r}\right|_{r=a} + k_{12}J_0(\xi_m a)\right) = 0 \end{aligned} \tag{2.27}$$

$$\begin{aligned} &\left(k_{31}\left.\frac{\partial Y_1(\eta_n r)}{\partial r}\right|_{r=a} + k_{32}Y_1(\eta_n a)\right)\left(k_{41}\left.\frac{\partial J_1(\eta_n r)}{\partial r}\right|_{r=b} + k_{42}J_1(\eta_n b)\right) \\ &-\left(k_{41}\left.\frac{\partial Y_1(\eta_n r)}{\partial r}\right|_{r=b} + k_{42}Y_1(\eta_n b)\right)\left(k_{31}\left.\frac{\partial J_1(\eta_n r)}{\partial r}\right|_{r=a} + k_{32}J_1(\eta_n a)\right) = 0 \end{aligned} \tag{2.28}$$

Equations (2.27) and (2.28) have an infinite number of the roots, because the Bessel functions are periodic. According to the properties of Sturm-Liouville problem, the kernel functions are orthogonal with respect to the weight function r. Taking the finite Hankel transform of Eqs. (2.19) and (2.21), and then using the operational properties on the derivatives [25], leads to

$$t_0\ddot{\overline{T}}_1 + \dot{\overline{T}}_1 + \xi_m^2\overline{T}_1 = A_1(t) \tag{2.29}$$

$$\ddot{\overline{u}}_1 + \eta_n^2\overline{u}_1 = A_2(t) \tag{2.30}$$

where

$$A_1(t) = \frac{2}{\pi}\left(f_2(t) - \frac{d_2}{d_1}f_1(t)\right) \tag{2.31}$$

$$A_2(t) = \frac{2}{\pi}\left(f_4(t) - \frac{d_4}{d_3}f_3(t)\right) \tag{2.32}$$

and

$$\begin{aligned} d_1 &= k_{11}\frac{\partial J_0(\xi_m r)}{\partial r}\bigg|_{r=a} + k_{12}J_0(\xi_m a) \;\;,\;\; d_2 = k_{21}\frac{\partial J_0(\xi_m r)}{\partial r}\bigg|_{r=b} + k_{22}J_0(\xi_m b) \\ d_3 &= k_{31}\frac{\partial J_1(\eta_n r)}{\partial r}\bigg|_{r=a} + k_{32}J_1(\eta_n a) \;\;,\;\; d_4 = k_{41}\frac{\partial J_1(\eta_n r)}{\partial r}\bigg|_{r=b} + k_{42}J_1(\eta_n b) \end{aligned} \tag{2.33}$$

$\bar{T}_1$ and $\bar{u}_1$ are obtained by solving the nonhomogeneous second order differential equations (2.29) and (2.30), respectively, as follows

$$\bar{T}_1(t) = \frac{1}{\Delta}\int_0^t A_1(\tau)\left[e^{\frac{1}{2t_0}\tau + \frac{\Delta}{2t_0}(2t-\tau)} - e^{\frac{1+\Delta}{2t_0}(\tau - t)}\right] d\tau \tag{2.34}$$

$$\bar{u}_1(t,\eta_n) = \frac{1}{\eta_n}\int_0^t A_2(\tau)\sin\left(\eta_n(t-\tau)\right) d\tau \tag{2.35}$$

where $\Delta = \sqrt{1-4t_0\xi_m^2}$. The inverse finite Hankel transforms of Eqs. (2.24) can be defined by the following series

$$\begin{aligned} \mathscr{H}^{-1}[\bar{T}_1(t,\xi_m)] = T_1(r,t) &= \sum_{m=1}^{\infty} \tilde{a}_m \bar{T}_1(t,\xi_m) K_0(r,\xi_m) \\ \mathscr{H}^{-1}[\bar{u}_1(t,\eta_n)] = u_1(r,t) &= \sum_{n=1}^{\infty} \tilde{b}_n \bar{u}_1(t,\eta_n) K_1(r,\eta_n) \end{aligned} \tag{2.36}$$

where the coefficients of the series can be computed as

$$\tilde{a}_m = 1\Big/\|K_0(r,\xi_m)\|^2 \quad , \quad \tilde{b}_n = 1\Big/\|K_1(r,\eta_n)\|^2 \tag{2.37}$$

$\|K_0(r,\xi_m)\|^2$ and $\|K_1(r,\eta_n)\|^2$ are the square of the norm of $K_0(r,\xi_m)$ and $K_1(r,\eta_n)$, respectively, on the interval $[a,b]$ with weight function r, and are defined as

$$\|K_0(r,\xi_m)\|^2 = \int_a^b r[K_0(r,\xi_m)]^2 dr \quad , \quad \|K_1(r,\eta_n)\|^2 = \int_a^b r[K_1(r,\eta_n)]^2 dr \tag{2.38}$$

Due to the orthogonality properties of the kernel functions, the solutions of Eqs. (2.20) and (2.22), $T_2(r,t)$ and $u_2(r,t)$, can be expanded in terms of functions $K_0(r,\xi_m)$ and $K_1(r,\eta_n)$, respectively as follows

$$T_2(r,t) = \sum_{m=1}^{\infty}\sum_{n=1}^{\infty} Q_{mn}(t) K_0(r,\xi_m) \;\;,\;\; u_2(r,t) = \sum_{m=1}^{\infty}\sum_{n=1}^{\infty} S_{mn}(t) K_1(r,\eta_n) \tag{2.39}$$

where $Q_{mn}(t)$ and $S_{mn}(t)$ are unknown time dependent functions to be found. Substituting Eqs. (2.36) and (2.39) into Eqs. (2.20) and (2.22) and simplifying yields

$$\begin{aligned}&\left(t_0\ddot{Q}_{mn}+\dot{Q}_{mn}+\xi_m^2 Q_{mn}\right)K_0(r,\xi_m)\\&=-C\left\{t_0\ddot{S}_{mn}+\dot{S}_{mn}+t_0\tilde{b}_n\ddot{\bar{u}}_1+\tilde{b}_n\dot{\bar{u}}_1\right\}\left(\frac{\partial K_1(r,\eta_n)}{\partial r}+\frac{K_1(r,\eta_n)}{r}\right)\end{aligned} \tag{2.40}$$

$$\left(\ddot{S}_{mn}+\eta_n^2 S_{mn}\right)K_1(r,\eta_n)=r\omega^2-\frac{\partial K_0(r,\xi_m)}{\partial r}\left(Q_{mn}+\tilde{a}_m\bar{T}_1\right) \tag{2.41}$$

Using the orthogonality conditions for $K_0(r,\xi_m)$ and $K_1(r,\eta_n)$, multiplying both sides of Eqs. (2.40) and (2.41) by $rK_0(r,\xi_k)$ and $rK_1(r,\eta_j)$, respectively, and integrating from a to b, yields

$$t_0\ddot{Q}_{mn}+\dot{Q}_{mn}+\xi_m^2 Q_{mn}=CU_1\left\{t_0\ddot{S}_{mn}+\dot{S}_{mn}+t_0\tilde{b}_n\ddot{\bar{u}}_1+\tilde{b}_n\dot{\bar{u}}_1\right\} \tag{2.42}$$

$$\ddot{S}_{mn}+\eta_n^2 S_{mn}=U_2\left(Q_{mn}+\tilde{a}_m\bar{T}_1\right)+U_3\omega^2 \tag{2.43}$$

where

$$\begin{aligned}U_1&=-\frac{\int_a^b rK_0(r,\xi_m)\left\{\frac{\partial K_1(r,\eta_n)}{\partial r}+\frac{K_1(r,\eta_n)}{r}\right\}dr}{\left\|K_0(r,\xi_m)\right\|^2}\\U_2&=-\frac{\int_a^b rK_1(r,\eta_n)\frac{\partial K_0(r,\xi_m)}{\partial r}dr}{\left\|K_1(r,\eta_n)\right\|^2}\quad,\quad U_3=\frac{\int_a^b r^2K_1(r,\eta_n)dr}{\left\|K_1(r,\eta_n)\right\|^2}\end{aligned} \tag{2.44}$$

Also, according to the orthogonality conditions, by substituting Eqs. (2.39) into (2.20) and (2.22), respectively, the initial conditions for Eqs. (2.42) and (2.43) can be obtained. To solve the coupled Eqs. (2.42) and (2.43), they are decoupled by eliminating Q_{mn} from Eq. (2.42) using Eq. (2.43). Upon elimination, the decoupled equation is written as

$$\begin{aligned}&t_0{S^{(4)}}_{mn}+{S^{(3)}}_{mn}+\left(\xi_m^2+t_0\eta_n^2-Ct_0U_1U_2\right)\ddot{S}_{mn}+\left(\eta_n^2-CU_1U_2\right)\dot{S}_{mn}+\xi_m^2\eta_n^2S_{mn}\\&=CU_1U_2\tilde{b}_n\left(t_0\ddot{\bar{u}}_1+\dot{\bar{u}}_1\right)+U_2\tilde{a}_m\left(t_0\ddot{\bar{T}}_1+\dot{\bar{T}}_1+\xi_m^2\bar{T}_1\right)+\xi_m^2\omega^2U_3\end{aligned} \tag{2.45}$$

Substituting Eqs. (2.29) into Eq. (2.45) yields

$$\begin{aligned}&t_0{S^{(4)}}_{mn}+{S^{(3)}}_{mn}+\left(\xi_m^2+t_0\eta_n^2-Ct_0U_1U_2\right)\ddot{S}_{mn}+\left(\eta_n^2-CU_1U_2\right)\dot{S}_{mn}+\xi_m^2\eta_n^2S_{mn}\\&=CU_1U_2\tilde{b}_n\left(t_0\ddot{\bar{u}}_1+\dot{\bar{u}}_1\right)+U_2\tilde{a}_mA_1(t)+\xi_m^2\omega^2U_3\end{aligned} \tag{2.46}$$

$Q_{mn}(t)$ can be obtained by solving Eq. (2.46) for $S_{mn}(t)$ and substituting into Eq. (2.43) as

$$Q_{mn}(t)=\frac{1}{U_2}\left(\ddot{S}_{mn}+\eta_n^2S_{mn}-\omega^2U_3\right)-\tilde{a}_m\bar{T}_1 \tag{2.47}$$

Euation (2.46) is a nonhomogeneous ordinary differential equation with constant coefficients and has general and particular solutions. The complete solution of this equation may be represented as

$$S_{mn}(t) = S^g_{mn}(t) + S^p_{mn}(t) \tag{2.48}$$

where $S^g_{mn}(t)$ is a general solution of Eq. (2.46), with the right-hand terms equal zero. $S^p_{mn}(t)$ is particular solutions which is related to boundary conditions of the problem and angular velocity of the disk. The characteristic polynomial corresponding to Eq. (2.46) is

$$t_0 s^4 + s^3 + \left(\xi_m^2 + t_0\eta_n^2 - CU_1U_2t_0\right)s^2 + \left(\eta_n^2 - CU_1U_2\right)s + \xi_m^2\eta_n^2 = 0 \tag{2.49}$$

Solving Eq. (2.49) for every value of m and n gives four pairs of complex conjugate roots $s_{(mn,i)}(i = 1,\cdots,4)$, with a negative real part and an imaginary part. These roots cause four modes of mechanical oscillation related to the function $S_{mn}(t)$. The period and frequency of the oscillation only depend on the imaginary part. The damping of this oscillation is caused by the negative real part, which means the thermomechanical oscillation is stable.

Thus, the general solution of Eq. (2.46) with the right-hand terms equal zero is obtained as

$$S^g_{mn}(t) = \sum_{i=1}^{4} c_i e^{s_{mn,i}t} \tag{2.50}$$

where the constant coefficients c_i are determined by substituting the complete solution of Eq. (2.46) into the initial conditions.

Finally, the closed form solutions for the nondimensional temperature and displacement fields obtained from solving the governing coupled system of Eqs. (2.11) and (2.12), can be stated as follows

$$\begin{aligned} T(r,t) &= \sum_{m=1}^{\infty} \tilde{a}_m \bar{T}_1(t,\xi_m)K_0(r,\xi_m) + \sum_{m=1}^{\infty}\sum_{n=1}^{\infty} Q_{mn}(t)K_0(r,\xi_m) \\ u(r,t) &= \sum_{n=1}^{\infty} \tilde{b}_n \bar{u}_1(t,\eta_n)K_1(r,\eta_n) + \sum_{m=1}^{\infty}\sum_{n=1}^{\infty} S_{mn}(t)K_1(r,\eta_n) \end{aligned} \tag{2.51}$$

The expressions for the stress components in the disk are determined by substituting Eqs. (2.51) into (2.13). When the relaxation time is zero ($\hat{t}_0 = 0$), the same mathematical procedure may be used to solve the classical coupled thermoelastic equations.

2.3 Solution of uncoupled thermoelasticity

In the case of dynamic uncoupled thermoelasticity problem in the rotating disk ($C = 0$ and the effect of inertia term is considered), the solutions to uncoupled equations (2.12) and (2.16) can be separately obtained using the finite Hankel transform in a similar manner to that of coupled problems.
For the case of the quasi-static thermoelasticity problem, the differential equation of heat conduction (2.16) is a Bessel-type equation. This equation can be solved in a similar way to the previous problems to yield the temperature field. The equation of motion (2.17) can be written in the following form

$$\frac{\partial}{\partial r}\left[\frac{1}{r}\frac{\partial}{\partial r}(ru)\right] = \frac{\partial T}{\partial r} - r\omega^2 \tag{2.52}$$

Integrating Eq. (2.52) twice and designating the two integration constants as $c_1(t)$ and $c_2(t)$ gives the radial displacement as

$$u(r,t) = \frac{1}{r}\int_a^r T(r,t)rdr - \frac{1}{8}r^3\omega^2 + rc_1(t) + \frac{c_2(t)}{r} \tag{2.53}$$

By substituting Eq. (2.53) into Eqs. (2.13), without the hat sign for convenience, the stress components are obtained as

$$\begin{aligned}\sigma_{rr} = &-\left(\tfrac{2\mu}{\tilde{\lambda}+2\mu}\right)\tfrac{1}{r^2}\textstyle\int_a^r T(r,t)rdr - \tfrac{1}{8}\left(\tfrac{4\tilde{\lambda}+6\mu}{\tilde{\lambda}+2\mu}\right)r^2\omega^2 \\ &+\left(\tfrac{2\mu+2\tilde{\lambda}}{\tilde{\lambda}+2\mu}\right)c_1 - \left(\tfrac{2\mu}{\tilde{\lambda}+2\mu}\right)\tfrac{c_2}{r^2}\end{aligned} \tag{2.54}$$

$$\begin{aligned}\sigma_{\theta\theta} = &\left(\tfrac{2\mu}{\tilde{\lambda}+2\mu}\right)\left\{\tfrac{1}{r^2}\textstyle\int_a^r T(r,t)rdr - T\right\} \\ &-\left(\tfrac{4\tilde{\lambda}+2\mu}{\tilde{\lambda}+2\mu}\right)\tfrac{1}{8}r^2\omega^2 + \left(\tfrac{2\tilde{\lambda}+2\mu}{\tilde{\lambda}+2\mu}\right)c_1 + \left(\tfrac{2\mu}{\tilde{\lambda}+2\mu}\right)\tfrac{c_2}{r^2}\end{aligned} \tag{2.55}$$

The unknowns $c_1(t)$ and $c_2(t)$ may be determined by applying the mechanical boundary conditions.

2.4 Results and discussions

To investigate the accuracy of the presented formulations, an example is chosen from Ref. [4], where the coupled thermoelasticity of a disk is analyzed using the

finite element method. In this example, a stationary disk made of aluminum, with the Lamè constants $\lambda = 40.4$ GPa, $\mu = 27$ GPa and $\alpha = 23 \times 10^{-6}$ K^{-1}, $\rho = 2707$ kg/m^3, $\kappa = 204$ W/m·K and $c = 903$ J/kg·K is considered. The nondimensional inner and outer radii of the disk is given as $a = 1$ and $b = 2$, respectively. The inside boundary of the disk is assumed to be radially fixed, but exposed to a step function heat flux. The outside boundary is traction free with zero temperature change. The initial conditions for the displacement, velocity, temperature, and the rate of temperature are assumed to be zero.

In the case of zero angular velocity, assuming that $C = 0.02$ and $\hat{t}_0 = 0.64$, the time variation of the nondimensional temperature and radial displacement at mid-radius of the disk are plotted in Figs. 2.1. Good agreements are observed between the results of presented analytical method and those obtained using the Galerkin finite element method in Ref. [4].

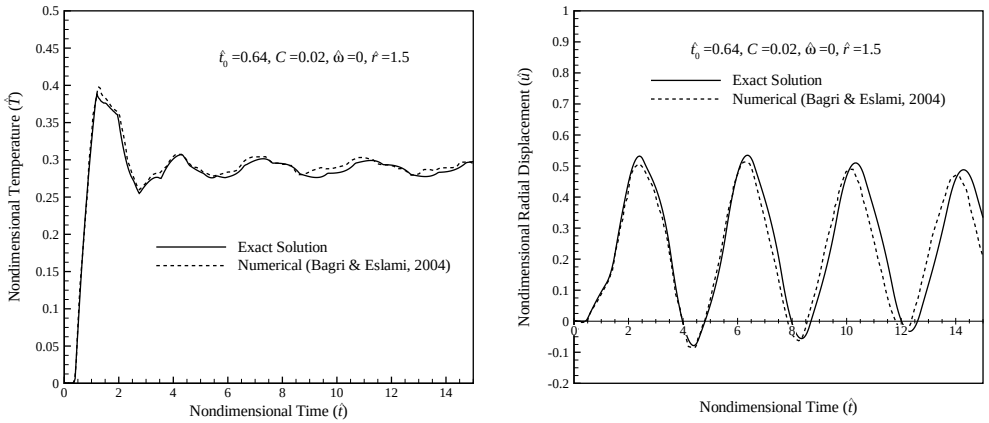

(a) temperature change (b) radial displacement

Fig. 2.1 Time history of the nondimensional temperature and displacement at mid-radius of the stationary disk.

Assuming that the disk is rotating with nondimensional angular velocity 0.01, the time histories of temperature and radial displacement at mid-radius of the disk for the different theories of thermoelasticity are shown in Fig. 2.2. Moreover, for these theories, the time histories of radial stress and tangential stress are plotted in Figs. 2.3 and 2.4, respectively. In this case, the reference temperature is considered to be 293 K.

As shown in Figs. 2.2-2.4, when thermal shock load is applied, the generalized

coupled theory based on LS model leads to larger maximum value of the curves for temperature, displacement and stresses compared to other theories.

The classical coupled theory and uncoupled theories of thermoelasticity predict an infinite propagation speed for the thermal disturbances. In other words, when $\hat{t}_0 = 0$ the hyperbolic heat conduction equation (2.11) reduces to a parabolic equation with infinite speed for thermal wave propagation. Moreover, this Fig. 2.2 shows that in the case of dynamic uncoupled solution, $C = 0$, the influence of temperature field on displacement filed is ignored and thus the radial displacement varies harmonically along the time with constant amplitudes. For coupled thermoelastic solutions, the displacement amplitudes are decreasing along the time axis. The reason is that for $C \neq 0$, damping term appears in the heat conduction equation and, therefore, the energy dissipation occurs in the system.

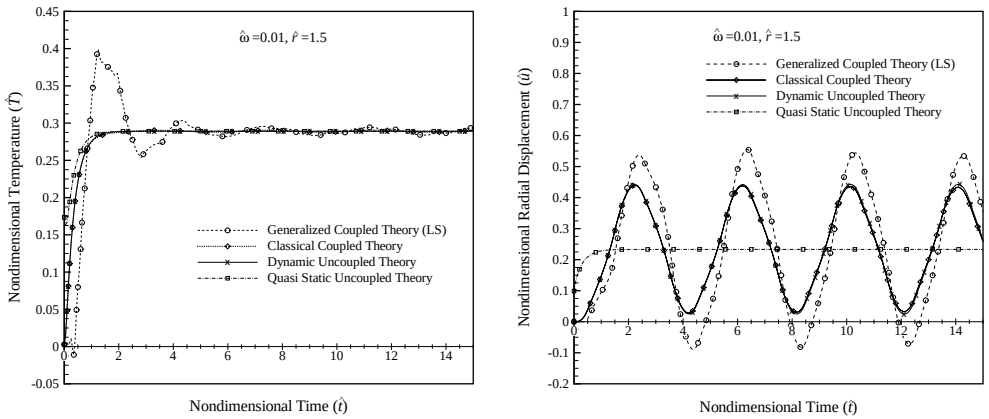

(a) temperature change (b) radial displacement

Fig. 2.2 Time history of the nondimensional temperature and displacement at mid-radius of the rotating disk for different theories of thermoelasticity.

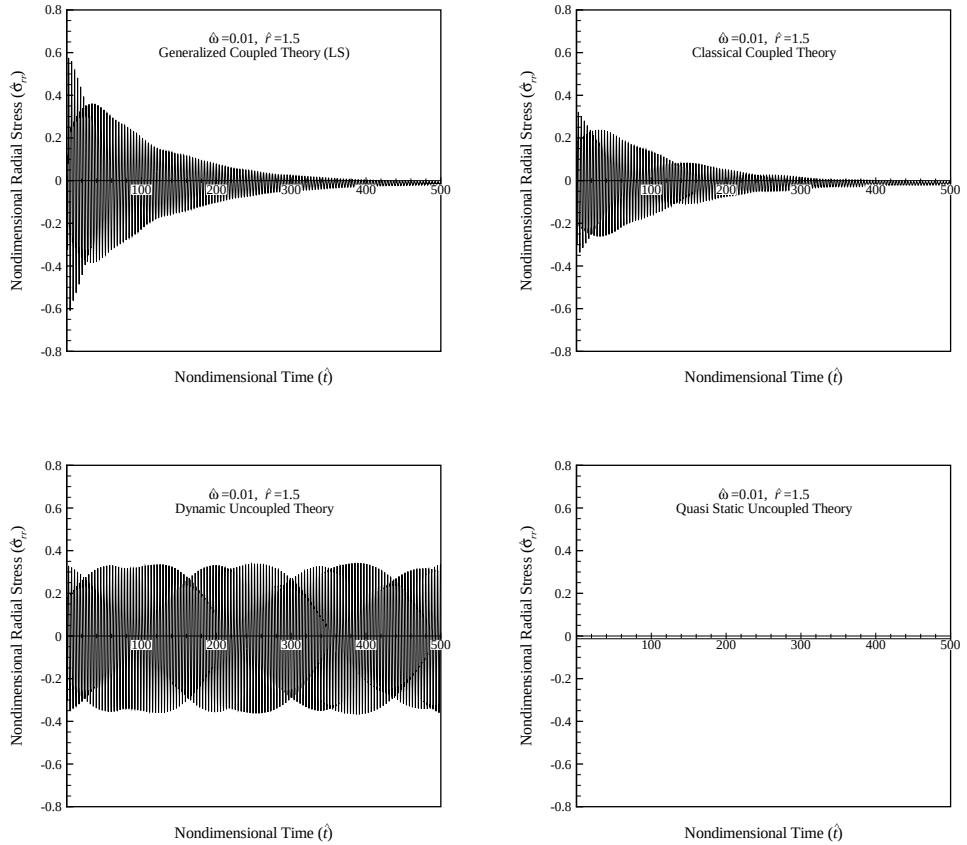

Fig. 2.3 Time history of the nondimensional radial stress at mid-radius of the rotating disk for different theories of thermoelasticity.

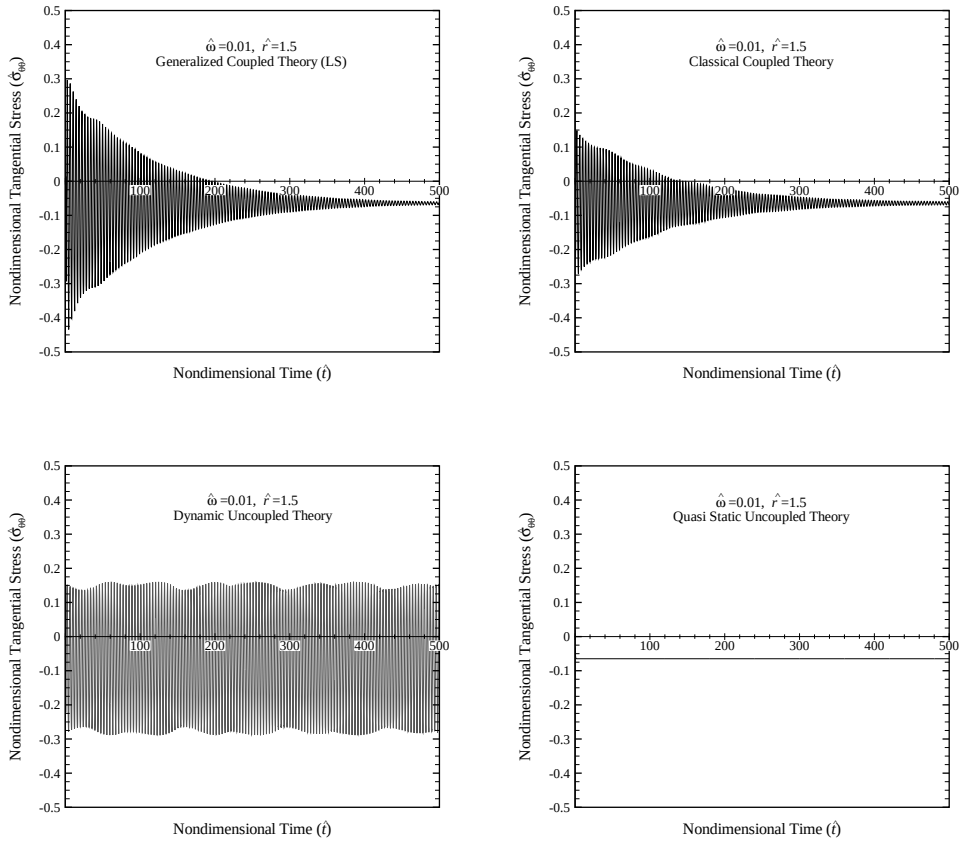

Fig. 2.4 Time history of the nondimensional tangential stress at mid-radius of the rotating disk for different theories of thermoelasticity.

The radial distribution of nondimensional temperature change, radial stress and circumferential stress for different theories of thermoelasticity at different values of the time are shown in Figs. 2.5, 2.6 and 2.7, respectively. In these figures, the temperature wave front is clearly observed from the figure related to generalized coupled solution. In this figure, times $\hat{t} = 0.25, 0.5$ and 0.75 show the temperature wave propagation, while times $\hat{t} = 1, 1.25$ indicate the wave reflection from the outer radius of the disk. However, the temperature gradient along the radius is smooth for the classical coupled and uncoupled theories of thermoelasticity due to the infinite speed of thermal wave disturbances in these theories. The elastic wave fronts are clearly seen from the figures related to coupled and dynamic uncoupled solutions, while the radial distribution of radial stress related to quasi static uncoupled solution is smooth at different values of the time.

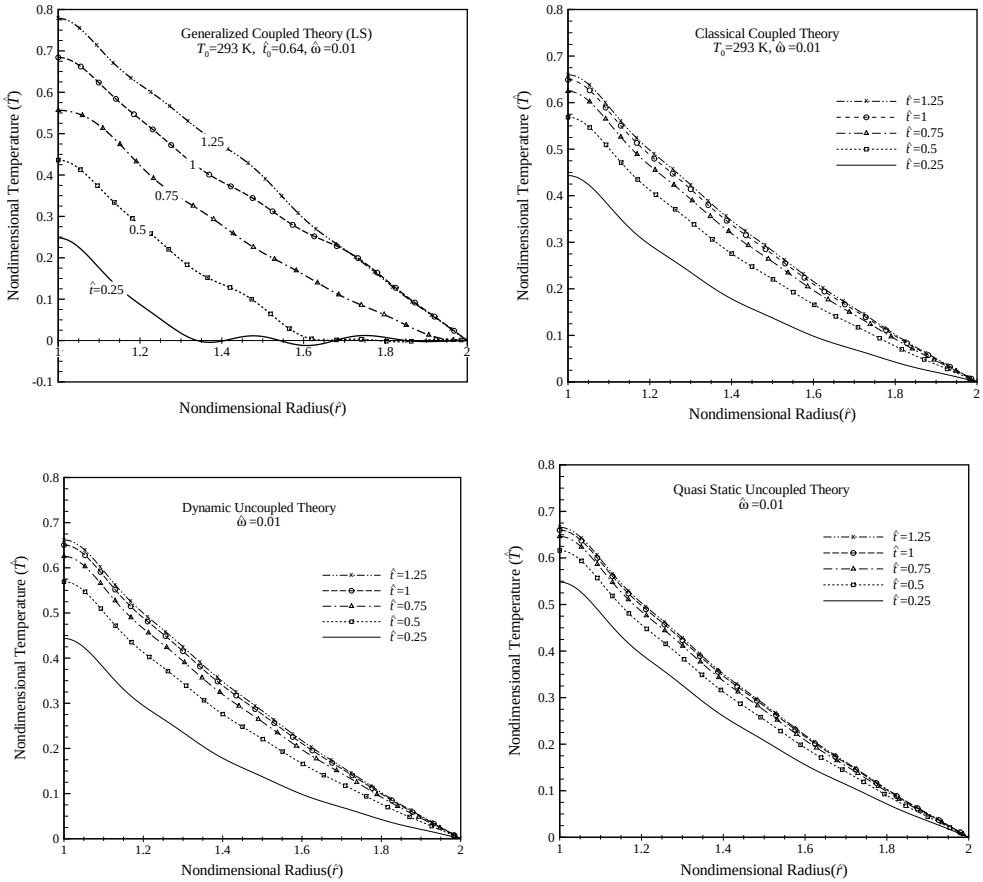

Fig. 2.5 Radial distribution of nondimensional temperature change for different theories of thermoelasticity.

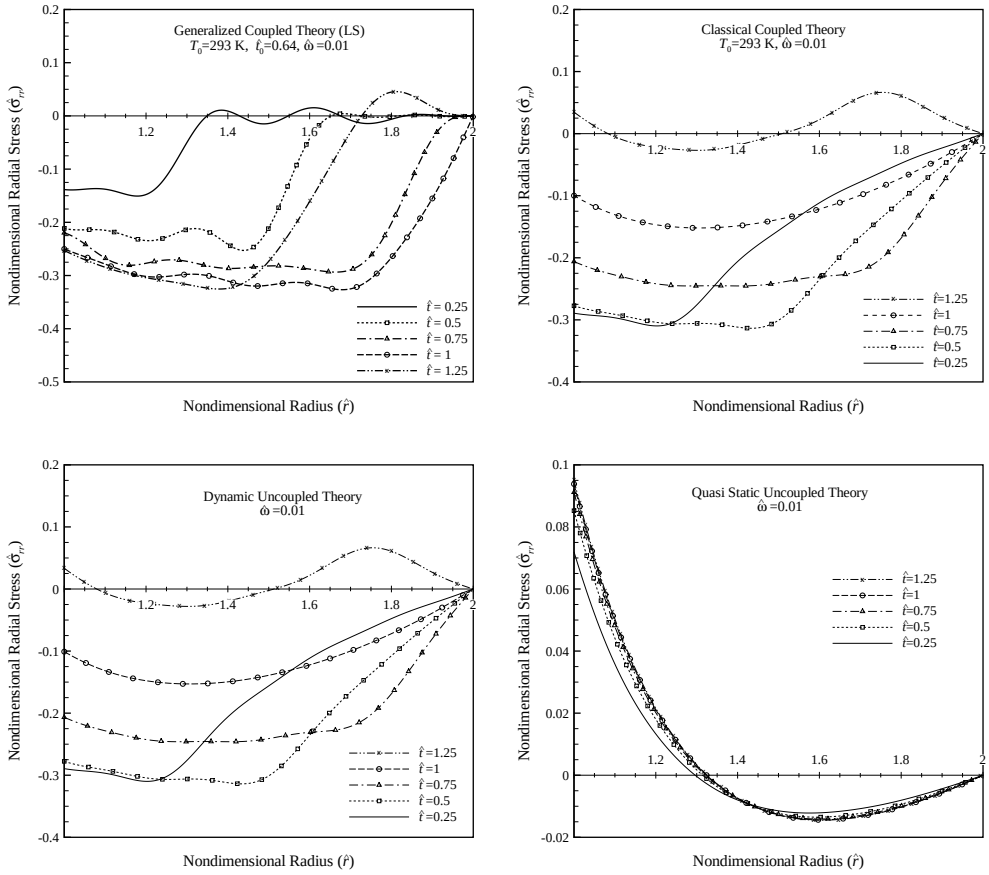

Fig. 2.6 Radial distribution of nondimensional radial stress for different theories of thermoelasticity.

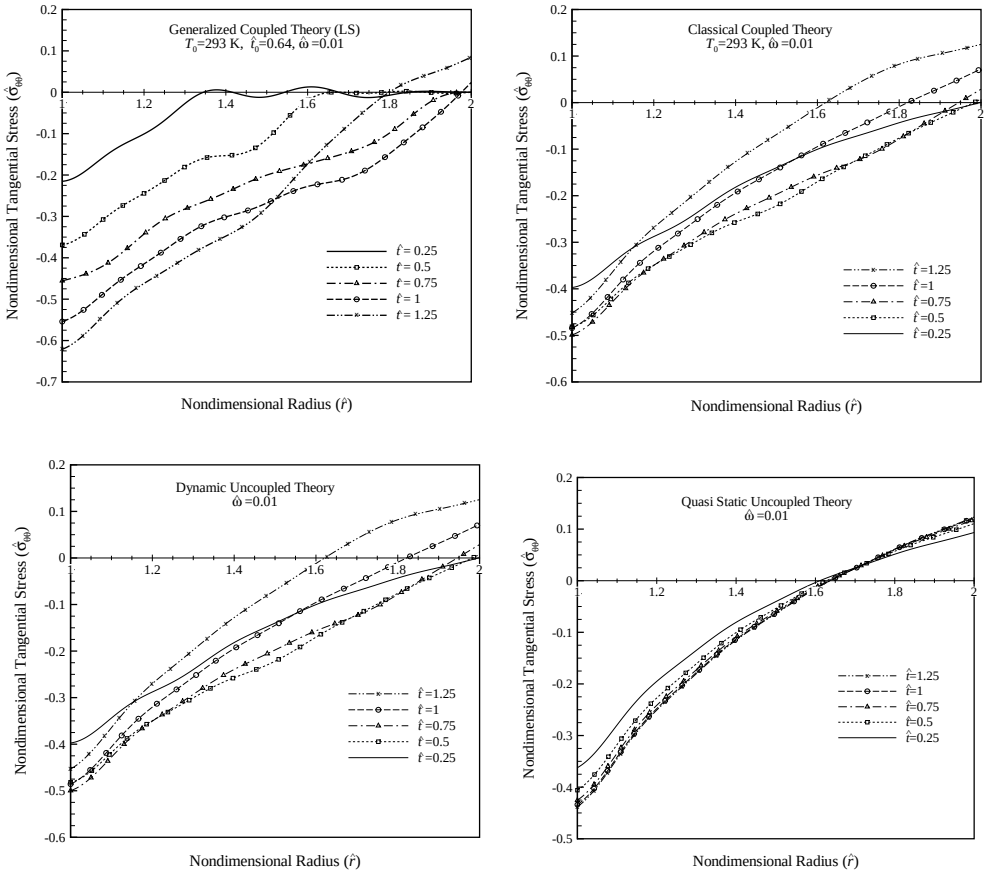

Fig. 2.7 Radial distribution of nondimensional circumferential stress for different theories of thermoelasticity.

The effects of coupling parameter (C) and relaxation time (t_0) on time histories of temperature and displacement at mid-radius of the rotating disk are illustrated in Figs. 2.8 and 2.9 for $\hat{\omega} = 0.01$.

Figure 2.8 shows temperature and radial displacement changes versus nondimensional time for values of $C = 0, 0.05, 0.1$ and 0.15. The case of $C = 0$ is related to the uncoupled solution. As shown in Fig. 2.8, when C takes a greater value, the maximum value of temperature reduce, while the amplitudes of oscillations of temperature increase. The reason is that with increasing damping parameter, the conversion between the mechanical and thermal energies increases. Moreover, in the case of uncoupled solution, $C = 0$, the influence of temperature field on displacement filed is ignored and thus the radial displacement varies harmonically along the time with constant amplitudes. For $C \neq 0$, the amplitudes are decreasing along the

time axis, and the damping is more noticeable for greater values of C. The reason is that for $C \neq 0$, damping term appears in the heat conduction equation and, therefore, the energy dissipation occurs in the system.

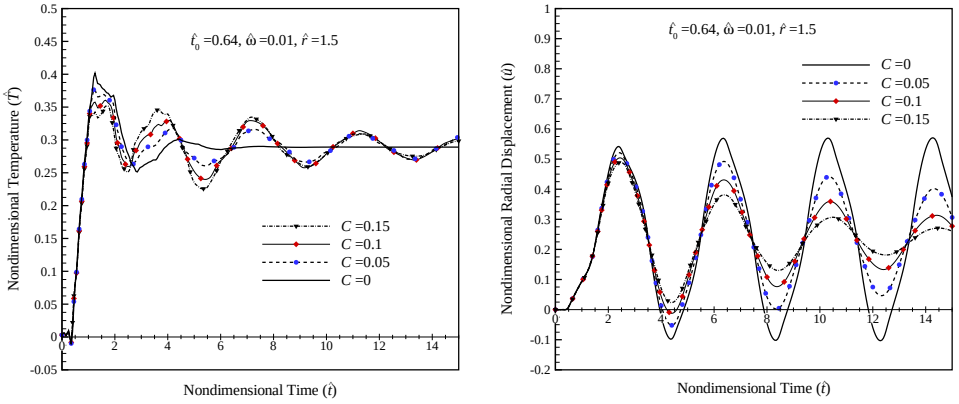

(a) temperature change (b) radial displacement

Fig. 2.8 Effect of coupling parameter on time history of the solutions at mid-radius of the rotating disk.

Figure 2.9 shows the time histories of temperature and radial displacement, for different values of relaxation time when the reference temperature is $T_0 = 293$ K. The nondimensional values of relaxation time associated with Lord-Shulman model are assumed to be 0.64 and 1.5625. The case of $\hat{t}_0 = 0$ is related to the classical theory of thermoelasticity that predicts an infinite propagation speed for the thermal disturbances. In other words, when $\hat{t}_0 = 0$ the hyperbolic heat conduction equation (2.11) reduces to a parabolic equation with infinite speed for thermal wave propagation. As shown in Fig. 2.9, with increasing relaxation time, the maximum value of the curves for temperature and displacement increase. However, since with the increase of relaxation time the propagation speed of thermal disturbances decreases, these maximum values occur at the later times.

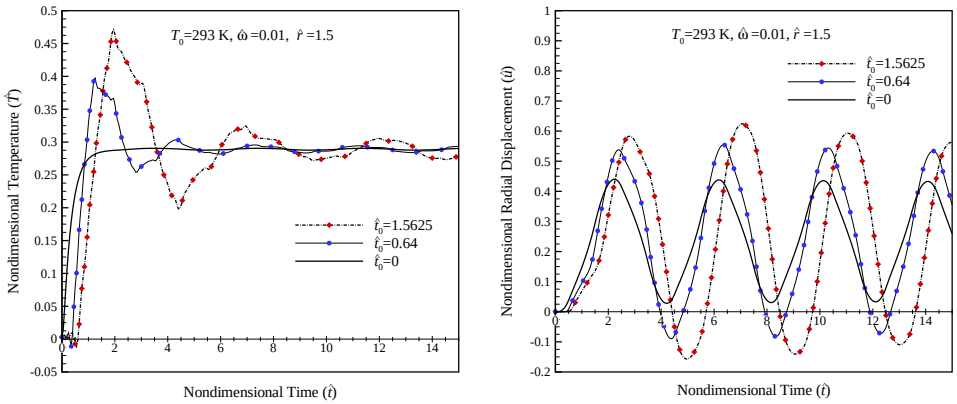

(a) temperature change (b) radial displacement

Fig. 2.9 Effect of relaxation time on time history of the solutions at mid-radius of the rotating disk.

2.5 Summary

In this chapter, thermoelasticity problems based on the classical and generalized coupled theories, and dynamic and quasi static uncoupled theories for a rotating disk are solved using a fully analytical procedure. Assuming that the disk is subjected to an arbitrary heat transfer and traction at its inner and outer radii, closed form formulations are presented for temperature and displacement fields. The procedure used in this work, is based on the finite Hankel transform. To validate the formulations, the results are compared with those obtained using the numerical method in the literature, which show good agreement. The radial distributions and time histories of temperature, displacement and stresses for the different theories of thermoelasticity in the disk are plotted and compared to each other.

Chapter 3

Stress analysis of disks using refined 1D FE models

Since providing an analytical solution for disk problems with more sophisticated geometries and boundary conditions is mathematically complex and may be impossible, the development of alternative numerical solution techniques seems essential. In the present chapter, a refined finite element method is employed for stress analysis of rotors and rotating disks with an arbitrary geometry.

3.1 FE methods refined through CUF

Despite significant advances in computing power, complex 3D FE models still impose large computational costs, especially during the iterative design stage. For this reason, reduced refined models may be used to obtain solutions with lower computational efforts. A general approach which can be employed to develop refined finite element models has been suggested in the book by Carrera *et al*. [15]. They introduced the Carrera Unified Formulations (CUF) in which the FE methods are formulated on the basis of a class of theories of structures. In fact, Carrera *et al*. [14] first developed a unified formulation for the 2D FE method (2D FE-CUF) to overcome the limitations of classical theories of plates and shells. A 1D FE method in framework of the CUF (1D FE-CUF) was later extended by Carrera *et al*. [17] based on the beam model to go beyond the classical beam theories. Indeed, the CUF has been able to enhance the capabilities of the 1D and 2D conventional finite

element methods, so that using these refined methods leads to 3D-like solutions but with lower computational costs. Furthermore, analysis of multi-field problems such as mechanical, thermal, electric and magnetic fields, as well as of layered structures is of other outstanding features of the CUF models.

3.2 Governing equations of rotating disks

Consider a variable thickness disk with an arbitrary profile, which is located in a reference stationary coordinate system (xyz) and it is rotating at a constant angular velocity ω about its axis. The disk is assumed to be at static equilibrium while it is subjected to body forces (1), surface forces (2), concentrated loads (3) and temperature gradients (4) as shown in Fig. 3.1.

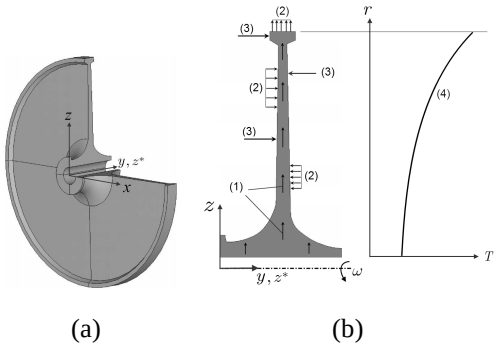

Fig. 3.1 A rotating disk with variable thickness subjected to mechanical and thermal loads (a) Structural coordinate systems, (b) A meridional section of the disk and loads.

The total potential energy, Π, that is the sum of the internal strain energy and the potential energy of the external forces, can be written as

$$\Pi = \frac{1}{2}\int_V \varepsilon^{\mathrm{e}\mathrm{T}}\sigma\, dV - \int_V \mathbf{u}^{\mathrm{T}}\mathbf{f}^{\mathrm{B}}\, dV - \int_S \mathbf{u}^{\mathrm{T}}\mathbf{f}^{\mathrm{S}}\, dS - \sum_k \mathbf{u}^{\mathrm{T}}\mathbf{f}^{\mathrm{C}_k} \tag{3.1}$$

where ε^{e} stands for the elastic strain vector, σ denotes the stress vector and $\mathrm{u} = \{u_x \quad u_y \quad u_z\}^{\mathrm{T}}$ is the displacement vector. Furthermore, $\mathbf{f}^{\mathrm{B}} = \{f_x^{\mathrm{B}} \quad f_y^{\mathrm{B}} \quad f_z^{\mathrm{B}}\}^{\mathrm{T}}$ is the vector of body forces per unit volume V, $\mathbf{f}^{\mathrm{S}}$ is the vector of surface forces per unit surface area S of the body, and $\mathbf{f}^{\mathrm{C}_k} = \{f_x^{\mathrm{C}_k} \quad f_y^{\mathrm{C}_k} \quad f_z^{\mathrm{C}_k}\}^{\mathrm{T}}$ is the vector of con-

centrated loads where k denotes the load application point. It is noted that the components of $\mathbf{f}^{\mathrm{B}}$ and $\mathbf{f}^{\mathrm{S}}$ may be a function of the coordinates x, y and z however the specific x, y and z coordinates of S are considered for $\mathbf{f}^{\mathrm{S}}$ [9].
The Hooke law for a linear thermoelastic material can be written as

$$\sigma = \mathbf{C}\varepsilon^{\mathrm{e}} \tag{3.2}$$

where $\mathbf{C}$ is the forth order tensor of elastic moduli. In the linear thermoelasticity, the elastic strain vector ε^{e} is equal to

$$\varepsilon^{\mathrm{e}} = \varepsilon - \varepsilon^{\mathrm{t}} \tag{3.3}$$

where ε denotes the total strain vector and ε^{t} is the strain vector due to the temperature change $\Delta T = T - T_0$, that is

$$\varepsilon^{\mathrm{t}} = \alpha(\Delta T) \tag{3.4}$$

where T_0 is the reference temperature. The steady-state temperature distribution T may be, in general, a function of all three space coordinates. α stands for the vector of linear thermal expansion coefficients. Moreover, the strain-displacement relations can be written as

$$\varepsilon = \mathbf{D}\mathbf{u} \tag{3.5}$$

where $\mathbf{D}$ is the matrix of linear differential operators.
Neglecting the time rate of elastic deformation, the body force per unit volume due to rotation can be obtained as

$$\mathbf{f}^{\mathrm{B}} = \rho\Omega^{\mathrm{T}}\Omega\mathbf{r} \tag{3.6}$$

where $\mathbf{r} = \{x_P \quad 0 \quad z_P\}^{\mathrm{T}}$ is the position vector of the material point with respect to the rotational axis, and ρ is the material density. The matrix Ω is

$$\Omega = \omega \begin{bmatrix} 0 & 0 & 1 \\ 0 & 0 & 0 \\ -1 & 0 & 0 \end{bmatrix} \tag{3.7}$$

Substituting Eqs. (3.2), (3.3) and (3.6) into Eq. (3.1), the total potential energy becomes

$$\begin{aligned}\Pi = &\frac{1}{2}\int_V [(\mathbf{u}^{\mathrm{T}}\mathbf{D}^{\mathrm{T}})\mathbf{C}(\mathbf{D}\mathbf{u})]\,dV - \int_V [(\mathbf{u}^{\mathrm{T}}\mathbf{D}^{\mathrm{T}})\mathbf{C}\alpha\Delta T)]\,dV \\ &+\frac{1}{2}\int_V (\Delta T\,\alpha^{\mathrm{T}}\mathbf{C}\alpha\Delta T)\,dV - \int_V \mathbf{u}^{\mathrm{T}}(\rho\Omega^2\mathbf{r})\,dV \\ &-\int_S \mathbf{u}^{\mathrm{T}}\mathbf{f}^{\mathrm{S}}\,dS - \sum_k \mathbf{u}^{\mathrm{T}}\mathbf{f}^{C_k}\end{aligned} \tag{3.8}$$

where $\Omega^2 = \Omega^{\mathrm{T}}\Omega$.

3.3 1D FE-CUF approach for variable thickness disks

A finite element formulation of Eq. (3.8) can be obtained using the 1D FE-CUF approach. To this end, the structure of Fig. 3.1 is assumed as a beam along its axis (y) so that each cross section of the beam (A) is defined in any orthogonal $x-z$ plane. The structure is discretized into a finite number of 1D beam elements in the y-direction, while the Lagrange-type expansions are employed to assume the model kinematics (see Fig. 3.2).

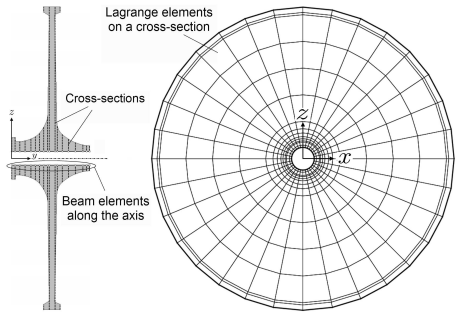

Fig. 3.2 A sample 1D FE model of a disk with arbitrary profile in the CUF framework.

Thus, the displacement field is characterized as

$$\mathbf{u}(x,y,z) = N_i(y)F_\tau(x,z)\mathbf{U}^{i\tau} \tag{3.9}$$

where $\mathrm{U}^{i\tau} = \{U_x^{i\tau} \quad U_y^{i\tau} \quad U_z^{i\tau}\}^{\mathrm{T}}$ is the nodal displacement vector, $N_i(y)$ are the shape functions, and F_τ are Lagrange polynomial expansions. In Eq. (3.9), τ ($\tau =$

$1,2,\ldots,\mathrm{M}$) and i ($i = 1,2,\ldots,\mathrm{N_{nodes}}$) indicate summation, according to the generalized Einstein's notation. Here, M and $\mathrm{N_{nodes}}$ are the number of terms of the expansion and the number of element nodes, respectively.

It is obvious that in the discretization process along the disk axis, the length of beam elements can be unequal. In other words, the cross sections need not be equidistant; in fact, it is advisable to select the sections closely together where there is sudden change in geometry, in loadings or in mechanical properties.

In this approach, three types of beam elements, two nodes (B2), three nodes (B3) and four nodes (B4), may be adopted to provide a linear, a quadratic and a cubic interpolation of the displacement variable along the longitudinal direction, respectively. For these elements, the distribution of the nodes in the natural coordinate system in which $-1 \leq \gamma \leq 1$ is shown in Fig. 3.3.

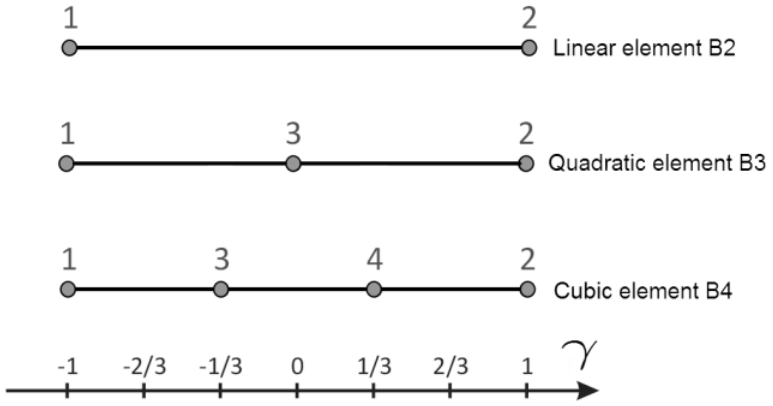

Fig. 3.3 Two-, three- and four- node beam elements in actual geometry.

Moreover, the shape functions of B2, B3 and B4 elements in the natural system, respectively, are express as follows

$$\begin{aligned} N_1(\gamma) &= \tfrac{1}{2}(1-\gamma) \\ N_2(\gamma) &= \tfrac{1}{2}(1+\gamma) \end{aligned} \tag{3.10}$$

$$\begin{aligned} N_1(\gamma) &= \tfrac{1}{2}\gamma(1-\gamma) \\ N_2(\gamma) &= (1+\gamma)(1-\gamma) \\ N_3(\gamma) &= \tfrac{1}{2}\gamma(1+\gamma) \end{aligned} \tag{3.11}$$

$$\begin{aligned} N_1(\gamma) &= -\tfrac{9}{16}(\gamma+\tfrac{1}{3})(\gamma-\tfrac{1}{3})(\gamma-1) \\ N_2(\gamma) &= \tfrac{27}{16}(\gamma+1)(\gamma-\tfrac{1}{3})(\gamma-1) \\ N_3(\gamma) &= -\tfrac{27}{16}(\gamma+1)(\gamma+\tfrac{1}{3})(\gamma-1) \\ N_4(\gamma) &= \tfrac{9}{16}(\gamma+1)(\gamma+\tfrac{1}{3})(\gamma-\tfrac{1}{3}) \end{aligned} \tag{3.12}$$

On the other hand, the cross sections can be discretized by using different types of Lagrange elements (LEs) such as linear three-point (denoted as L3), bilinear four-point (L4), quadratic nine-point (L9) and cubic sixteen-point (L16) elements (see Fig. 3.4).

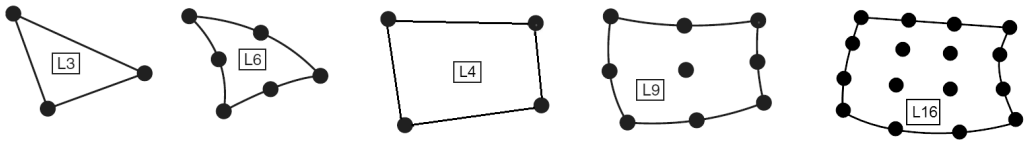

Fig. 3.4 Three-, six-, nine- and sixteen- node Lagrange elements (L3, L6, L9 and L16) in actual geometry.

Furthermore, a sample scheme of L9 element in the actual and the natural coordinate systems is shown in Fig. 3.5. In general, the coordinate transformation from an arbitrary cross section referred to (x,z) coordinates to the natural square (ξ,η) is trivial and more details can be found in Ref. [9].

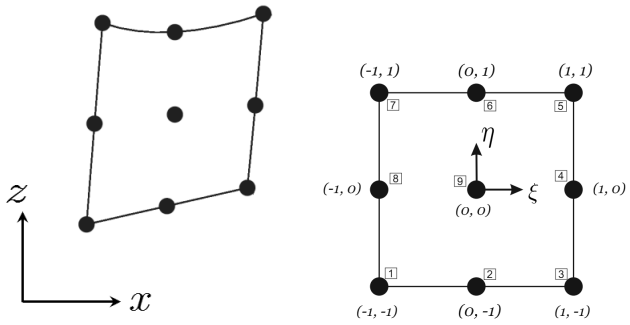

(a) (b)

Fig. 3.5 Sample scheme of L9 element in the actual (a) and the natural (b) coordinate systems.

Thus, the Lagrange polynomial expansions for L4 and L9 elements in the natural coordinate system (ξ,η) are expressed by the following relations [18]

$$\begin{gathered} F_\tau(\xi,\eta)=\frac{1}{4}(1+\xi\ \xi_\tau)(1+\eta\ \eta_\tau) \qquad \tau=1,2,3,4 \\ F_\tau(\xi,\eta)=\tfrac{1}{4}(\xi^2+\xi\ \xi_\tau)(\eta^2+\eta\ \eta_\tau) \qquad \tau=1,3,5,7 \\ F_\tau(\xi,\eta)=\tfrac{1}{2}\eta_\tau^2(\eta^2-\eta\ \eta_\tau)(1-\xi^2)+\tfrac{1}{2}\xi_\tau^2(\xi^2-\xi\ \xi_\tau)(1-\eta^2) \qquad \tau=2,4,6,8 \\ F_\tau(\xi,\eta)=(1-\xi^2)(1-\eta^2) \qquad \tau=9 \end{gathered} \tag{3.13}$$

here $-1\le\xi\le1$ and $-1\le\eta\le1$, whereas ξ_τ and η_τ are the natural coordinates of τ^{th} Lagrange point of the element. In addition, the polynomials related to L16 are give by [18]

$$F_{\tau_{JK}}(\xi,\eta)=L_J(\xi)L_K(\eta) \qquad J,K=1,2,3,4 \tag{3.14}$$

where

$$\begin{gathered} L_1(\xi)=\tfrac{1}{16}(\xi-1)(1-9\xi^2) \qquad L_2(\xi)=\tfrac{9}{16}(1-\xi^2)(1-3\xi) \\ L_3(\xi)=\tfrac{9}{16}(1-\xi^2)(1+3\xi) \qquad L_4(\xi)=\tfrac{1}{16}(1+\xi)(9\xi^2-1) \end{gathered} \tag{3.15}$$

For instance, the displacement components for a basic beam element B2 ($N_{nodes}=2$) and one L9 element ($M=9$) over the cross-section is

$$\begin{gathered} u_x=N_iF_\tau U_x^{i\tau}=N_1(F_1U_x^{11}+\cdots+F_9U_x^{19})+N_2(F_1U_x^{21}+\cdots+F_9U_x^{29}) \\ u_y=N_iF_\tau U_y^{i\tau}=N_1(F_1U_y^{11}+\cdots+F_9U_y^{19})+N_2(F_1U_y^{21}+\cdots+F_9U_y^{29}) \\ u_z=N_iF_\tau U_z^{i\tau}=N_1(F_1U_z^{11}+\cdots+F_9U_z^{19})+N_2(F_1U_z^{21}+\cdots+F_9U_z^{29}) \end{gathered} \tag{3.16}$$

3.4 Finite element equations in CUF form

Substituting the unified displacement field (Eq. (3.9)) into Eq. (3.8), the total potential energy becomes

$$\begin{aligned}\Pi = &\frac{1}{2}\int_V \mathbf{U}^{js\mathrm{T}}[(\mathbf{D}^{\mathrm{T}}N_jF_s)\mathbf{C}(\mathbf{D}N_iF_\tau)]\mathbf{U}^{i\tau}\,dV - \int_V [(\mathbf{D}^{\mathrm{T}}N_iF_\tau)\mathbf{C}\alpha\Delta T]\mathbf{U}^{i\tau}\,dV \\ &+\frac{1}{2}\int_V (\Delta T\,\alpha^{\mathrm{T}}\mathbf{C}\alpha\Delta T)\,dV - \int_V (N_iF_\tau\rho\Omega^2\mathbf{r})\mathbf{U}^{i\tau}\,dV \\ &-\int_S (N_iF_\tau\mathbf{f}^{\mathrm{S}})\mathbf{U}^{i\tau}\,dS - \sum_k (N_iF_\tau\mathbf{f}^{\mathrm{C}_k})\mathbf{U}^{i\tau}\end{aligned} \tag{3.17}$$

The principle of minimum potential energy requires

$$\frac{\partial\Pi}{\partial\mathrm{U}} = 0 \tag{3.18}$$

Thus, differentiation of Π with respect to the nodal displacements U yields the following equilibrium equations for a finite element

$$\begin{aligned}&\int_V [(\mathbf{D}^{\mathrm{T}}N_jF_s)\mathbf{C}(\mathbf{D}N_iF_\tau)]\mathbf{U}^{js}\,dV - \int_V [(\mathbf{D}^{\mathrm{T}}N_iF_\tau)\beta\Delta T]\,dV \\ &-\int_V (N_iF_\tau\rho\Omega^2\mathbf{r})\,dV - \int_S (N_iF_\tau\mathbf{f}^{\mathrm{S}})\,dS - \sum_k (N_iF_\tau\mathbf{f}^{\mathrm{C}_k}) = 0\end{aligned} \tag{3.19}$$

in which $\beta = \mathbf{C}\alpha$ stands for the vector of stress-temperature moduli. The equation (3.19) may be presented in matrix form as

$$\mathbf{K}^{ij\tau s}\mathbf{U}^{js} = \mathbf{F}^{i\tau} \tag{3.20}$$

where

$$\mathbf{F}^{i\tau} = \mathbf{F}_T^{i\tau} + \mathbf{F}_{\mathrm{B}}^{i\tau} + \mathbf{F}_{\mathrm{S}}^{i\tau} + \mathbf{F}_{\mathrm{C}}^{i\tau} \tag{3.21}$$

The $\mathrm{K}^{ij\tau s}$ matrix is the structural stiffness matrix. The superscripts s and j are similar to τ and i, respectively, and indicate summation based on Einstein's notation. $\mathbf{F}_T^{i\tau}$ is the thermal load vector, which represents artificial forces for modeling thermal expansion, $\mathbf{F}_{\mathrm{B}}^{i\tau}$ is the vector of the body force due to rotational speed, $\mathbf{F}_{\mathrm{S}}^{i\tau}$ is the force vector due to tractions applied on the surface area, and $\mathbf{F}_{\mathrm{C}}^{i\tau}$ is the force vector due to

concentrated external loads. The matrix and vectors are defined as

$$\begin{aligned}
\mathrm{K}^{ij\tau s} &= \int_V \left[(\mathbf{D}^{\mathrm{T}} N_j F_s)\mathbf{C}(\mathbf{D}N_i F_\tau)\right] dV \\
\mathbf{F}_T^{i\tau} &= \int_V \left[(\mathbf{D}^{\mathrm{T}} N_i F_\tau)\beta\Delta T\right] dV \\
\mathbf{F}_{\mathrm{B}}^{i\tau} &= \int_V \left(N_i F_\tau \rho\Omega^2 \mathbf{r}\right) dV \\
\mathbf{F}_{\mathrm{S}}^{i\tau} &= \int_S \left(N_i F_\tau \mathbf{f}^{\mathrm{S}}\right) dS \\
\mathbf{F}_{\mathrm{C}}^{i\tau} &= \sum_k (N_i F_\tau \mathbf{f}^{C_k})
\end{aligned} \tag{3.22}$$

Four superscripts τ, s, i and j are exploited to assemble the stiffness matrix and the load vectors. In fact, the CUF presents a condensed notation that leads to the so-called fundamental nucleus (FN) of all the FE matrix and vectors involved. Equations (3.19) or (3.20) can be used for a disk made of a heterogeneous anisotropic material that is subjected to arbitrary surface and concentrated forces, as well as an arbitrary steady-state temperature field.
According to 1D CUF theory (see Fig. 3.2), the components of strain, ε, stress, σ and thermal expansion coefficient, α, vectors may be grouped as it follows

$$\varepsilon_p = \{\varepsilon_{zz} \;\; \varepsilon_{xx} \;\; \varepsilon_{xz}\}^{\mathrm{T}} \qquad \varepsilon_n = \{\varepsilon_{yy} \;\; \varepsilon_{yz} \;\; \varepsilon_{xy}\}^{\mathrm{T}} \tag{3.23}$$

$$\sigma_p = \{\sigma_{zz} \;\; \sigma_{xx} \;\; \sigma_{xz}\}^{\mathrm{T}} \qquad \sigma_n = \{\sigma_{yy} \;\; \sigma_{yz} \;\; \sigma_{xy}\}^{\mathrm{T}} \tag{3.24}$$

$$\alpha_p = \{\alpha_{zz} \;\; \alpha_{xx} \;\; \alpha_{xz}\}^{\mathrm{T}} \qquad \alpha_n = \{\alpha_{yy} \;\; \alpha_{yz} \;\; \alpha_{xy}\}^{\mathrm{T}} \tag{3.25}$$

where the subscript p denotes the in-plane components over a cross section of the disk, while n indicates the normal components to the cross section. Therefore, strain-displacement relations (3.5) can be decomposed into the two following expressions

$$\begin{aligned}
\varepsilon_p &= \mathbf{D_p}\mathbf{u} \\
\varepsilon_n &= (\mathbf{D}_{ny} + \mathbf{D}_{np})\mathbf{u}
\end{aligned} \tag{3.26}$$

where the matrices $\mathbf{D}_p$, $\mathbf{D}_{np}$ and $\mathbf{D}_{ny}$ are the linear differential operators

$$\mathbf{D}_p = \begin{bmatrix} 0 & 0 & \partial/\partial z \\ \partial/\partial x & 0 & 0 \\ \partial/\partial z & 0 & \partial/\partial x \end{bmatrix}, \quad \mathbf{D}_{np} = \begin{bmatrix} 0 & 0 & 0 \\ 0 & \partial/\partial z & 0 \\ 0 & \partial/\partial x & 0 \end{bmatrix}$$
$$\mathbf{D}_{ny} = \begin{bmatrix} 0 & \partial/\partial y & 0 \\ 0 & 0 & \partial/\partial y \\ \partial/\partial y & 0 & 0 \end{bmatrix} \tag{3.27}$$

In a similar manner, the grouped stresses and stress-temperature moduli are obtained as

$$\begin{aligned} \boldsymbol{\sigma}_p &= \mathbf{C}_{pp}\boldsymbol{\varepsilon}_p + \mathbf{C}_{pn}\boldsymbol{\varepsilon}_n \\ \boldsymbol{\sigma}_n &= \mathbf{C}_{np}\boldsymbol{\varepsilon}_p + \mathbf{C}_{nn}\boldsymbol{\varepsilon}_n \end{aligned} \tag{3.28}$$

$$\begin{aligned} \boldsymbol{\beta}_p &= \mathbf{C}_{pp}\boldsymbol{\alpha}_p + \mathbf{C}_{pn}\boldsymbol{\alpha}_n \\ \boldsymbol{\beta}_n &= \mathbf{C}_{np}\boldsymbol{\alpha}_p + \mathbf{C}_{nn}\boldsymbol{\alpha}_n \end{aligned} \tag{3.29}$$

where $\mathbf{C}_{np} = \mathbf{C}_{pn}^{\mathrm{T}}$. In order to summarize, the expanded expressions for components of the matrix $\mathbf{C}$ for anisotropic materials are not given here, but they can be found in Refs. [61] and [56]. For isotropic materials, $\boldsymbol{\alpha}_p = \alpha\{1\ \ 1\ \ 0\}^{\mathrm{T}}$, $\boldsymbol{\alpha}_n = \alpha\{1\ \ 0\ \ 0\}^{\mathrm{T}}$ and $\mathbf{C}_{pp}$, $\mathbf{C}_{pn}$ and $\mathbf{C}_{nn}$ result in the following matrices

$$\mathbf{C}_{pp} = \begin{bmatrix} \lambda+2\mu & \lambda & 0 \\ \lambda & \lambda+2\mu & 0 \\ 0 & 0 & 0 \end{bmatrix}, \qquad \mathbf{C}_{pn} = \begin{bmatrix} \lambda & 0 & 0 \\ \lambda & 0 & 0 \\ 0 & \mu & 0 \end{bmatrix}$$
$$\tilde{\mathbf{C}}_{nn} = \begin{bmatrix} \lambda+2\mu & 0 & 0 \\ 0 & 0 & 0 \\ 0 & 0 & \mu \end{bmatrix} \tag{3.30}$$

in which λ and μ are Lame constants, and α is the thermal expansion coefficient of the material.

$$\lambda = \frac{\nu E}{(1+\nu)(1-2\nu)} \quad , \quad \mu = \frac{E}{2(1+\nu)}$$

For a general anisotropic material but homogeneous along the thickness, which means material properties may continuously vary along radius of the disk, the fun-

damental nuclei (3.22) can be written as

$$\begin{aligned}
\mathbf{K}^{ij\tau s} &= I_l^{ij} \lhd \mathrm{D}_{np}^{\mathrm{T}}(F_\tau \mathrm{I}) \left[\tilde{\mathrm{C}}_{np}\mathrm{D}_p(F_s\mathrm{I}) + \tilde{\mathrm{C}}_{nn}\mathrm{D}_{np}(F_s\mathrm{I})\right] + \\
&+ \mathrm{D}_p^{\mathrm{T}}(F_\tau \mathrm{I}) \left[\tilde{\mathrm{C}}_{pp}\mathrm{D}_p(F_s\mathrm{I}) + \tilde{\mathrm{C}}_{pn}\mathrm{D}_{np}(F_s\mathrm{I})\right] \rhd + \\
&+ I_l^{ij,y} \lhd \left[\mathrm{D}_{np}^{\mathrm{T}}(F_\tau \mathrm{I}) + \mathrm{D}_p^{\mathrm{T}}(F_\tau \mathrm{I})\tilde{\mathrm{C}}_{pn}\right] F_s \rhd + \\
&+ I_l^{i,yj}\mathrm{I}_{Ay}^{\mathrm{T}} \lhd F_\tau \left[\tilde{\mathrm{C}}_{np}\mathrm{D}_p(F_s\mathrm{I}) + \tilde{\mathrm{C}}_{nn}\mathrm{D}_{np}(F_s\mathrm{I})\right] \rhd + \\
&+ I_l^{i,yj,y}\mathrm{I}_{Ay}^{\mathrm{T}}\mathrm{I}_{Ay} \lhd F_\tau \tilde{\mathrm{C}}_{nn} F_s \rhd
\end{aligned}$$

$$\begin{aligned}
\mathbf{F}_T^{i\tau} &= I_l^i \lhd \Delta T \left[(\mathrm{D}_p^{\mathrm{T}} F_\tau)\boldsymbol{\beta}_p + (\mathrm{D}_{np}^{\mathrm{T}} F_\tau)\boldsymbol{\beta}_n\right] \rhd \\
&+ I_l^{i,y} \lhd \Delta T F_\tau \left[\mathbf{I}_{Ay}\boldsymbol{\beta}_n\right] \rhd
\end{aligned} \tag{3.31}$$

$$\mathbf{F}_{\mathrm{B}}^{i\tau} = I_l^i \lhd F_\tau \rho \mathrm{r} \rhd \Omega^2$$

$$\mathbf{F}_{\mathrm{S}}^{i\tau} = \int_S (N_i F_\tau \mathbf{f}^{\mathrm{S}})\, dS$$

$$\mathbf{F}_{\mathrm{C}}^{i\tau} = \sum_k (N_i F_\tau \mathbf{f}^{\mathrm{C}_k})$$

where

$$\mathrm{I}_{Ay} = \begin{bmatrix} 0 & 0 & 1 \\ 1 & 0 & 0 \\ 0 & 1 & 0 \end{bmatrix} \qquad \mathrm{I} = \begin{bmatrix} 1 & 0 & 0 \\ 0 & 1 & 0 \\ 0 & 0 & 1 \end{bmatrix} \tag{3.32}$$

$$\lhd \cdots \rhd = \int_A \cdots \, \mathrm{d}A \tag{3.33}$$

$$\begin{aligned}
&\{I_l^i, I_l^{ij}, I_l^{ij,y}, I_l^{i,yj}, I_l^{i,yj,y}\} = \\
&\int_l \{N_i, (N_i N_j), (N_i N_{j,y}), (N_{i,y} N_j), (N_{i,y} N_{j,y})\}\, \mathrm{d}y
\end{aligned} \tag{3.34}$$

In order to obtain the governing equations of thermoelasticity problem in rotating disks, Eq. (3.20) can be expanded with respect to the superscripts τ, s, i and j as

$$\mathrm{KU} = \mathrm{F} \tag{3.35}$$

where K and F are the total stiffness matrix and the vector of equivalent nodal forces, respectively. The nodal displacement vector U contains all the nodal degrees of freedom (DOFs) of the structural model, which can be calculated as

$$\mathrm{DOFs} = \sum_{i=1}^{\mathrm{N_{BN}}} (3 \times \mathrm{N}_{\mathrm{LN}}^i) \tag{3.36}$$

here N_{LN} is the total number of Lagrange nodal points on each cross section and N_{BN} stands for the total number of beam nodes along the longitudinal axis. More details about assembly technique of these matrix and vectors can be found in Ref. [16].

The governing equations of the structure (Eq. (3.35)) can be solved for the nodal displacement vector U in the Cartesian reference system by the standard numerical solvers. Stress and displacement fields for axisymmetric structures are typically presented in a cylindrical coordinate system. Hence, using transformation relations, the fields in the rectangular Cartesian system (xyz) can be transformed into the cylindrical coordinate system $(r\theta z^*)$ as it follows

$$\begin{aligned}
\mathbf{u} &= \{u_r \;\; u_\theta \;\; u_{z^*}\}^{\mathrm{T}} \\
\varepsilon &= \{\varepsilon_{rr} \;\; \varepsilon_{\theta\theta} \;\; \varepsilon_{z^*z^*} \;\; \varepsilon_{r\theta} \;\; \varepsilon_{\theta z^*} \;\; \varepsilon_{rz^*}\}^{\mathrm{T}} \\
\sigma &= \{\sigma_{rr} \;\; \sigma_{\theta\theta} \;\; \sigma_{z^*z^*} \;\; \sigma_{r\theta} \;\; \sigma_{\theta z^*} \;\; \sigma_{rz^*}\}^{\mathrm{T}}
\end{aligned} \tag{3.37}$$

As shown in Fig. 3.1, r, θ and z^* show the radial, circumferential and axial directions, respectively.

3.5 Numerical results

To investigate the validity of the formulations presented in the previous sections for stress analysis of rotors, several illustrative examples including rotating disks with constant and variable thickness; and a complex rotor are analyzed in this section.

3.5.1 Rotating disk with constant thickness

Consider a disk with constant thickness made of steel, with the Young's modulus $E = 210$ (GPa), Poisson's ratio $\nu = 0.3$ and density $\rho = 7800$ $(\mathrm{kg/m^3})$. The inner and outer radii; and the thickness of the disk are assumed as 0.1016 (m), 0.2032 (m) and 0.01 (m), respectively. The disk is rotating with angular velocity 2000 (rad/s). The inside boundary of the disk (hub) is assumed to be fully fixed (mounted on a rigid shaft), while the outside boundary is traction free.

To solve this problem by the presented 1D CUF model, geometry of the disk can be discretized into a number of B2 or B3 elements along its axis direction and used a number of L4, L9 or L16 approximations over the related cross-sections. For example, Fig. 3.6 shows discretization of the disk into a single 3-node beam element (1B3) along the axis, while 100 elements of L9 (5×20 L9) have been employed for approximation of deformations on its cross-section.

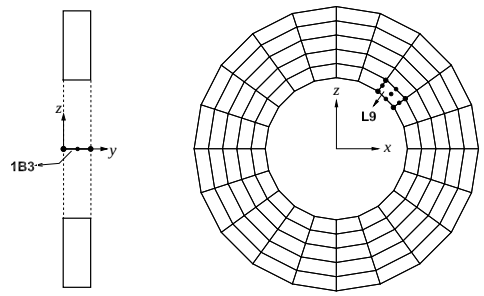

(a) 1B3 (b) 5×20 L9

Fig. 3.6 Discretizing a constant thickness disk into one B3 finite element along the axis with a distribution of L9 elements over the cross-section.

In this example, the effect of the various discretizations associated with the CUF approach on stress and displacement fields of the disk was investigated. Considering 1B3 along the axis, radial displacement (u_r), radial stress (σ_{rr}) and circumferential stress ($\sigma_{\theta\theta}$) for the point located at the mid-radius of the disk ($r = 0.1524$ (m)) for different distributions of LEs on the cross-section are presented and compared with analytical and converged 3D conventional finite element (FE) solutions in Table 3.1. The closed form formulation of the analytical solutions, which are reported in the second row of Tables 3.1 and 3.2, for annular disks with constant thickness can be found in Ref. [62]. The 3D conventional FE solution, in the last row of these tables, was performed by the ANSYS FE package. Several solid models with finer meshes especially at vicinity of the inner and outer radii of the disk were analyzed in order to check convergence of the ANSYS model. In the converged ANSYS model, the geometry of the disk has been meshed into 1920 SOLID185 (3D 8-node structural solid) elements as 24×40 elements on the cross-section (24 elements in radial direction and 40 element in circumferential direction) and 2 elements across the thickness of the disk, and in this case, the total number of DOFs is equal to 9000. In this dissertation, the computational costs of FE models are provided in terms of DOFs.

Table 3.1 Displacement and stresses at mid-radius of the rotating disk with constant thickness for different LEs on the cross-section.

Model		DOFs	u_r (μm)	σ_{rr} (MPa)	$\sigma_{\theta\theta}$ (MPa)
Analytical		1	85.93	276.70	201.42
1D CUF*	4×32 L4	1440	$81.56^{(5.07)}$	$265.45^{(4.06)}$	$186.07^{(7.62)}$
	4×40 L4	1800	$81.39^{(5.28)}$	$270.27^{(2.32)}$	$185.54^{(7.88)}$
	4×48 L4	2160	$81.50^{(5.15)}$	$270.70^{(2.16)}$	$185.73^{(7.79)}$
	5×32 L4	1728	$81.98^{(4.59)}$	$272.08^{(1.66)}$	$189.37^{(5.98)}$
	8×32 L4	2592	$83.53^{(2.79)}$	$273.72^{(1.07)}$	$194.00^{(3.67)}$
	4×20 L9	3240	$84.91^{(1.18)}$	$275.33^{(0.49)}$	$195.93^{(2.72)}$
	5×16 L9	3168	$85.19^{(0.86)}$	$276.45^{(0.08)}$	$198.05^{(1.67)}$
	5×20 L9	3960	$85.19^{(0.86)}$	$276.58^{(0.04)}$	$197.88^{(1.75)}$
	2×16 L16	3024	$85.23^{(0.82)}$	$275.88^{(0.29)}$	$199.01^{(1.19)}$
3D FE (ANSYS)		9000	$85.29^{(0.74)}$	$275.55^{(0.41)}$	$200.10^{(0.65)}$

*= With a single B3 element along the axis of the disk.

()= Absolute percentage difference with respect to the analytical solution.

In Table 3.1, it is observed that if L4 elements are employed, the maximum error for the solution of nodal displacement with respect to the analytical solution is about 5% that is related to models with 4 elements in the radial direction. An appropriate distribution of L4 elements may improve the accuracy of the solution. A significant improvement has been achieved by enriching the discretization along the radius. Indeed, the maximum error decreases below 2.8% with the distribution of 8×32 L4. Moreover, it can be found from the table that the effect of high-order elements, like L9, is significant on the accuracy. Considering the mesh 4×20 of L9 elements on the cross-section, for instance, the error is reduced to 1.18%. Refining the distribution of L9 elements through the radius, the difference of the CUF solution can be reduced to less than one percent. For example, using the mesh 5×16 L9, the maximum relative error is decreased to 0.86%, however, its DOFs is less than the distribution of 4×20. In addition, employing the 5×16 L9 model with almost one-third DOFs of the 3D FE model can lead to the solid-like accuracy.

As presented in Table 3.1, by using L16 elements, more accurate results are obtained even with less DOFs compare to those of L9 elements. For instance, using only 32 L16 elements with 3024 DOFs and distribution of 2×16, the solution of nodal displacement is obtained somewhat more accurate than 5×16 and 5×20 distributions of L9 with, respectively, 3160 and 3960 DOFs.

The comparisons in Table 3.1 reveal that by selecting proper distribution and type of LE on cross-section of the disk, the results of 1D CUF models have close agreement with the analytical reference solutions. Moreover, a local refinement of LE over cross-section makes 1D CUF models able to reduce computational costs compared to the 3D FE model. From Table 3.1, it is also found that the rate of convergence of L9 element is higher than L4. The reason is that L9 element uses quadratic polynomials as interpolation functions to approximate the displacement field, while polynomials related to L4 element are of a bilinear type, see Eqs (3.13) and (3.14). Therefore, increasing numbers of L4 elements on a cross section can be very effective. Furthermore, the results obtained for L4 and L9 elements show that a refinement of LEs distribution in the radial direction is more effective than one in the circumferential direction. In other words, increase of number of elements along the radial direction, compared to circumferential direction, is more effective in improving the accuracy of the solution. Since distribution refinements of LEs over a cross-section may cause computational costs to be increased, making use of a higher-order LE (L16 cubic element for example) can reduce DOFs, while preserving the accuracy.

Refinement of the discretization along the axis of the disk may also be investigated to improve the solution accuracy and to optimize computational costs. The effect of different beam elements along the axis on values of the displacement and the stresses at the mid-radius of the disk is represented in Table 3.2, with the assumption that the distribution of 5×20 L9 has been used on the cross-section. It is observed that using only a single B2 element in the CUF model of the disk detects the 3D-like result with very low computational costs (almost 3.4 times less DOFs). Also, it may be found from Table 3.2 that as the number of beam elements increases, the solution accuracy may not arise. In addition, since the disk is thin, the use of quadratic beam elements B3 across the thickness does not have significant effect on the accuracy of the results and only increases the DOFs.

Table 3.2 Displacement and stresses at mid-radius of the rotating disk with constant thickness for different LEs on the cross-section.

Model		DOFs	u_r (μm)	σ_{rr} (MPa)	$\sigma_{\theta\theta}$ (MPa)
Analytical		1	85.93	276.70	201.42
1D CUF*	1B2	2640	$85.26^{(0.77)}$	$275.60^{(0.40)}$	$197.62^{(1.88)}$
	2B2	3960	$85.23^{(0.81)}$	$276.45^{(0.09)}$	$197.89^{(1.75)}$
	3B2	5280	$85.23^{(0.81)}$	$276.45^{(0.09)}$	$197.89^{(1.75)}$
	1B3	3960	$85.18^{(0.86)}$	$276.58^{(0.04)}$	$197.88^{(1.75)}$
	2B3	6600	$85.18^{(0.87)}$	$276.63^{(0.02)}$	$198.01^{(1.69)}$
	3B3	9240	$85.18^{(0.87)}$	$276.64^{(0.02)}$	$198.05^{(1.67)}$
3D FE (ANSYS)		9000	$85.29^{(0.74)}$	$275.55^{(0.41)}$	$200.10^{(0.65)}$

*= With a distribution of 5×20 L9 over the cross-section.

()= Absolute percentage difference with respect to the analytical solution.

3.5.2 Rotating disk with variable thickness

To demonstrate the ability of the method to analyze rotating disks with arbitrary profile, an annular disk with hyperbolic profile may be considered. In this example, the disk profile is assumed to be symmetric with respect to the middle plane perpendicular to the axis. The inner and outer radii are $r_{in} = 0.05$ (m), $r_o = 0.2$ (m), while thickness of the disk from the value of $h_i = 0.06$ (m) in inner radius varies as $h(r) = Cr^a$ to the value of $h_o = 0.03$ (m) in outer radius, where $C = 0.0134$ and $a = -0.5$. The material of the disk is assumed to be steel with $E = 207$ (GPa), $\nu = 0.28$ and $\rho = 7860$ $(\mathrm{kg/m^3})$. Angular velocity and boundary conditions of the disk are identical to those of the previous example.

According to the approach presented in this chapter, the variable thickness disk can be considered as a beam with non-uniform cross-sections across its axis. A FE representation of the geometry may significantly differ from that of the real 3D disk. Hence, an appropriate FE modeling of the 3D structure is a critical and lengthy task which can also affect accuracy of the results and computational costs.

To find an acceptable model of the disk in the CUF framework, eight 1D FE models of the 3D geometry are considered, namely, models (1)-(8), as shown in Fig. 3.7.

Moreover, a detailed description of these models is presented in Table 3.3. The models (1)-(8) are obtained by dividing the disk across its thickness at the inner radius into 8, 10, 12, 14, 16, 18 or 22 discrete elements of type B2. The length and related cross-section of the beam elements in each model may be different from each other. Figure 3.7 clearly shows that due to symmetry of the disk profile with respect to the middle plane perpendicular to the axis, 3 to 8 types of cross-section with different radii are needed to generate the models (1) to (8). Furthermore, the models (2) and (3) as well as the models (7) and (8) are, however, geometrically identical but the number of beam elements used in the tow models is different each other, as shown in Fig. 3.7.

To describe the deformations over each cross-section of the models (1)-(8), a distribution of L4 elements is employed, as presented in Table 3.3. The distributions of L4 elements in the model (1) with three different cross-sections, for instance, may be indicated as $(2/6/8) \times 32$ which means the number of the elements in the circumferential direction of all cross-sections is 32, while the cross sections, from the smaller to the larger, are divided into 2, 6 and 8 elements, respectively, along the radial direction. In Fig. 3.8, the discretization and the 1D FE model (7) of the disk using 18 B2 across it axis and the distributions of L4 elements over the 8 different cross-sections are shown.

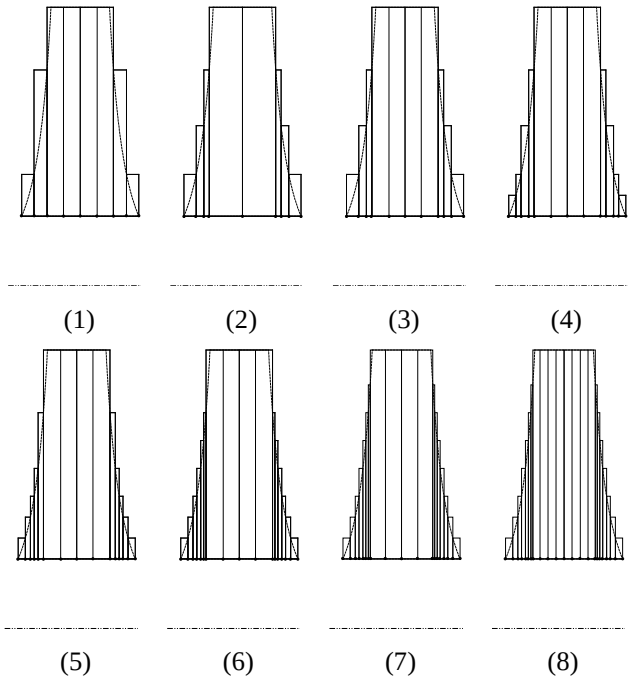

Fig. 3.7 Different 1D FE models of the variable thickness disk based on the CUF approach, discretizing along the disk axis into: (1) 8 B2 with 3 different cross-sections (Sec.), (2) 8 B2, 4 Sec., (3) 10 B2, 4 Sec., (4) 12 B2, 5 Sec., (5) 14 B2, 6 Sec., (6) 16 B2, 7 Sec., (7) 18 B2, 8 Sec., (8) 22 B2, 8 Sec.

Table 3.3 1D CUF FE models of the variable thickness disk

Model	Discretizing		DOFs
	along the axis	over the cross-sections	
(1)	8 B2, 3 Sec.*	$(2/6/8) \times 32$ L4	6240
(2)	8 B2, 4 Sec.	$(2/4/6/8) \times 32$ L4	5472
(3)	10 B2, 4 Sec.	$(2/4/6/8) \times 32$ L4	7200
(4)	12 B2, 5 Sec.	$(1/2/4/6/8) \times 32$ L4	7584
(5)	14 B2, 6 Sec.	$(1/2/3/4/6/8) \times 32$ L4	8352
(6)	16 B2, 7 Sec.	$(1/2/3/4/5/6/8) \times 32$ L4	9504
(7)	18 B2, 8 Sec.	$(1/2/3/4/5/6/7/8) \times 32$ L4	11040
(8)	22 B2, 8 Sec.	$(1/2/3/4/5/6/7/8) \times 32$ L4	14496

* = 3 types of cross-section with different radii

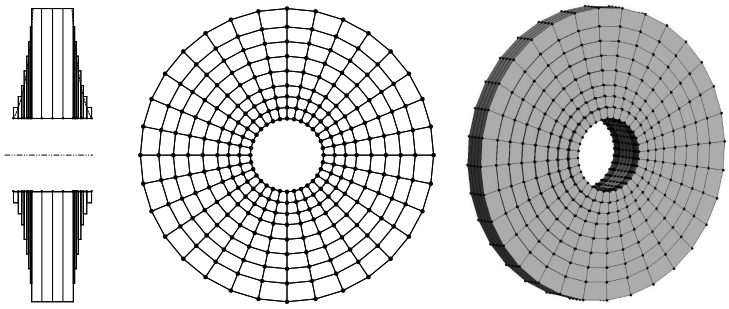

(a) (b) (c)

Fig. 3.8 A FE model of the variable thickness disk based on the 1D CUF approach, (a) 18 B2 elements along the axis, (b) distribution of L4 elements as 8×32 over cross-section with the outer radius, (c) the FE model (7) of the disk with total DOFs=11040.

In Fig. 3.9, distributions of the radial displacement along radius of the disk at the middle plane perpendicular to the axis obtained from the eight 1D CUF FE models are plotted and compared with analytical and converged 3D FE solutions. Moreover, values of the displacement at mid and outer radii of the disk (u_r at $r = 0.125, 0.2$ m) for the different models are reported and compared with the reference solutions in Table 3.4.

The analytical solution for this example may be obtained using relations presented in Ref. [62] for annular disks of hyperbolic thickness. The 3D FE analysis was also done by ANSYS using a converged model, as shown in Fig. 3.10, with 14400 total DOFs made of 3120 8-node solid elements with three DOFs per element node. To check convergence of the ANSYS model in relation to the total number of the elements in the solution domain, several models with finer meshes especially at vicinity of the inner and outer radii were investigated.

From the comparisons presented in Fig. 3.9 and Table 3.4, it may be found that 1D CUF FE models have an acceptable accuracy and very high rate of convergence in predicting the displacement field. Good overall agreements are observed between the results obtained by these models and the reference analytical solution. The maximum difference between the results of the CUF models and the reference analytical solution is less than 1.7 percent that is related to the models (7) and (8). Furthermore, the results given in Table 3.4 reveal that discretizing of the disk profile into an appropriate number of beam elements and cross-sections may lead to solid-like accuracy with much lower computational effort. For instance, the model (2) which is created by 8 B2 elements with distributions of $(2/4/6/8)\times32$ L4 over 4 different cross-sections provides an excellent accuracy (below 0.6% difference with respect

to the analytical solution for the nodal displacement) almost like the ANSYS result, but with about 2.6 times less DOFs of the 3D ANSYS model. On the other hand, a comparison between the results of the models (2) and (3) (or the models (7) and (8)) which are geometrically identical shows that the increasing beam elements may not result in more accurate solution and only leads to a model with larger DOFs.

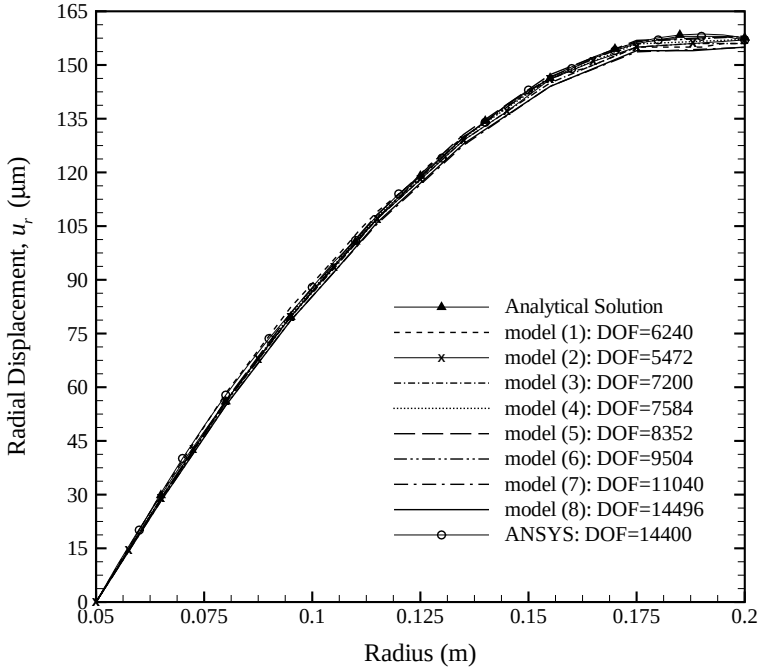

Fig. 3.9 Radial distributions of the radial displacement at the middle plane perpendicular to the axis of the variable thickness disk for the different FE models.

Table 3.4 Comparison of the radial displacements at mid and outer radii of the variable thickness disk for the different FE models.

Model		DOFs	radial displacment u_r (μm)	
			at mid-radius	at outer radius
Analytical		1	119.01	157.57
1D CUF FE	(1)	6240	$120.32^{(1.10)}$	$156.00^{(1.00)}$
	(2)	5472	$118.36^{(0.54)}$	$157.00^{(0.36)}$
	(3)	7200	$118.36^{(0.54)}$	$156.42^{(0.73)}$
	(4)	7584	$118.75^{(0.22)}$	$157.15^{(0.27)}$
	(5)	8352	$119.50^{(0.41)}$	$158.08^{(0.32)}$
	(6)	9504	$118.50^{(0.43)}$	$157.93^{(0.23)}$
	(7)	11040	$117.26^{(1.47)}$	$154.92^{(1.68)}$
	(8)	14496	$117.06^{(1.64)}$	$155.00^{(1.63)}$
3D FE (ANSYS)		14400	$119.00^{(0.01)}$	$157.10^{(0.30)}$

$()$ = absolute percentage difference with respect to the analytical solution.

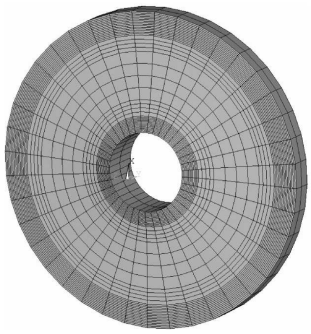

Fig. 3.10 ANSYS model with 3120 8-node elements (SOLID185), total DOFs 14400.

Figure 3.11 shows distributions of the averaged radial and circumferential stresses along the radius of the disk for the different models. As may be seen from the figure, the results of the presented models are in close agreement with the analytical and 3D FE solutions, especially, in zones far from the boundaries. There are, however, some deviations between the FE and analytical results at the boundaries of the disk,

where higher-order elements or mesh refinement over the cross-sections may be typical remedies.

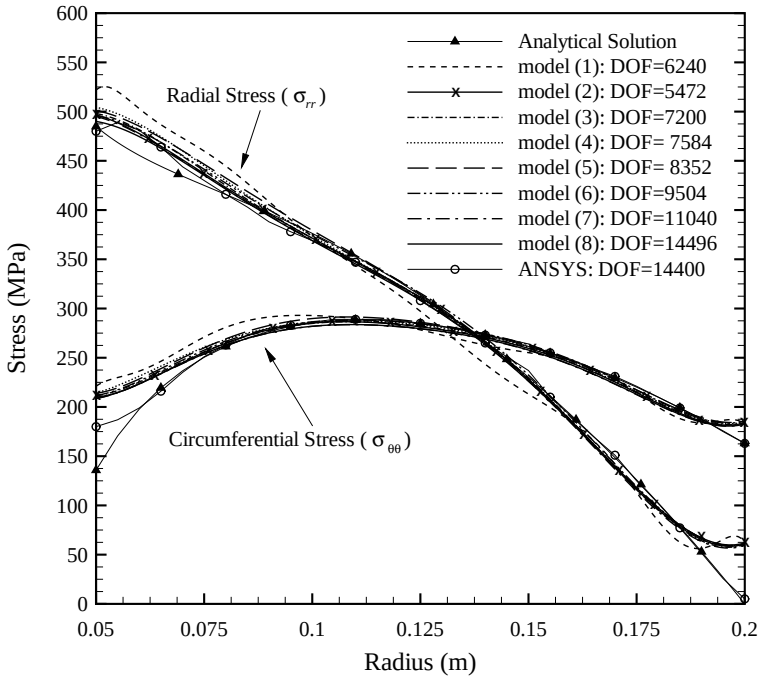

Fig. 3.11 Radial distributions of the stresses at the middle plane perpendicular to the axis of the variable thickness disk for the different FE models.

It should be noted that FE discretization along the axis of the disk is, by definition, a process that leads to a modified geometry of the structure. This means that all 1D FE models shown in Fig. 3.7 are not geometrically identical, and can not be compared with each other. On the other hand, the investigation of the models shows that since the disk has been assumed as a thick beam, increasing beam elements along its axis may not have significant effect on accuracy of the results and only leads to more DOFs. In fact, the purpose of the different discretizations presented in Fig. 3.7, as well as the investigations of the displacement and the stresses in Figs. 3.9 and 3.11 and Table 3.4, could be to find a proper 1D FE model of the disk for stress analysis with an acceptable initial accuracy and a reasonable number of DOFs compared to the 3D FEM.

Thus, in this numerical example, the model (2) may be adopted as a 1D FE model that satisfactorily balances accuracy and DOFs. Further improvement in the accuracy of the solution may be obtained by a discretization refinement over the cross-

sections. A convergence study on the solution can be performed to find an appropriate mesh of L4 elements over the cross-sections.
It has been already verified that in a disk problem, increasing number of discretized elements through the radial direction, compared to circumferential direction, is more effective in improving the accuracy of the solution. In this study, therefore, five types of mesh refined in the radial direction as $(1/2/3/4)\times 32$, $(2/4/6/8)\times 32$, $(5/7/9/14)\times 32$, $(4/8/12/16)\times 32$ and $(10/12/14/20)\times 32$ are considered over the four cross-sections of the model (2). These five meshes are showed in Fig. 3.12. The effect of the different discretizations on the displacement and the stresses of the model (2) is shown in Tables 3.5 and 3.6, as well as Figs. 3.13 and 3.14.

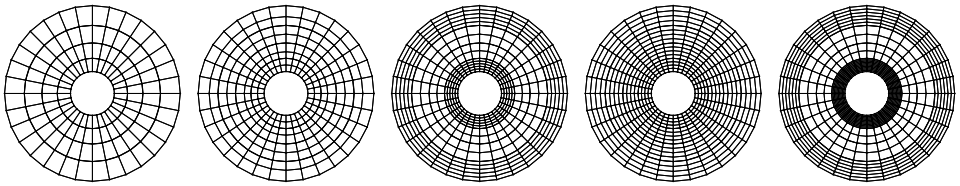

(a) (b) (c) (d) (e)

Fig. 3.12 Different discretizations over the cross-sections of the 1D CUF FE model (2): (a) $(1/2/3/4)\times 32$, (b) $(2/4/6/8)\times 32$, (c) $(5/7/9/14)\times 32$, (d) $(4/8/12/16)\times 32$ and (e) $(10/12/14/20)\times 32$.

Table 3.5 presents the convergence of the radial displacement values at mid and outer radii of the disk. Also, the distributions of the displacement are plotted along the radial direction for the different meshes in Fig. 3.13. It is seen that the results rapidly converge to the analytical solution by enriching the discretization along the radius. Using the mesh $(4/8/12/16)\times 32$ over the cross-sections, instead of $(1/2/3/4)\times 32$ or $(2/4/6/8)\times 32$, for instance, an excellent agreement and solid-like accuracy is observed between result of the CUF model and the analytical solution. It may be preferable to tune the refinement locally in order to optimize computational costs. For this purpose, the mesh $(5/7/9/14)\times 32$ which has finer discretization at the vicinity of the inner and outer radii can be sufficient for reaching the convergent solution with about 1.6 times less DOFs compared to the 3D FE analysis.

Table 3.5 Comparison of radial displacements at mid and outer radii of the variable thickness disk for the different meshes over the cross-sections.

Model	DOFs	radial displacment u_r (μm)	
		at mid-radius	at outer radius
Analytical	1	119.01	157.57
8 B2, $(1/2/3/4)\times 32$	3168	$114.50^{(3.79)}$	$154.00^{(2.27)}$
8 B2, $(2/4/6/8)\times 32$	5472	$118.00^{(0.85)}$	$157.00^{(0.36)}$
8 B2, $(5/7/9/14)\times 32$	8928	$119.00^{(0.01)}$	$157.00^{(0.36)}$
8 B2, $(4/8/12/16)\times 32$	10080	$119.00^{(0.01)}$	$158.00^{(0.27)}$
8 B2, $(10/12/14/20)\times 32$	13536	$119.00^{(0.01)}$	$157.00^{(0.36)}$
3D FE (ANSYS)	14400	$119.00^{(0.01)}$	$157.10^{(0.30)}$

$^{()}$ = absolute percentage difference with respect to the analytical solution.

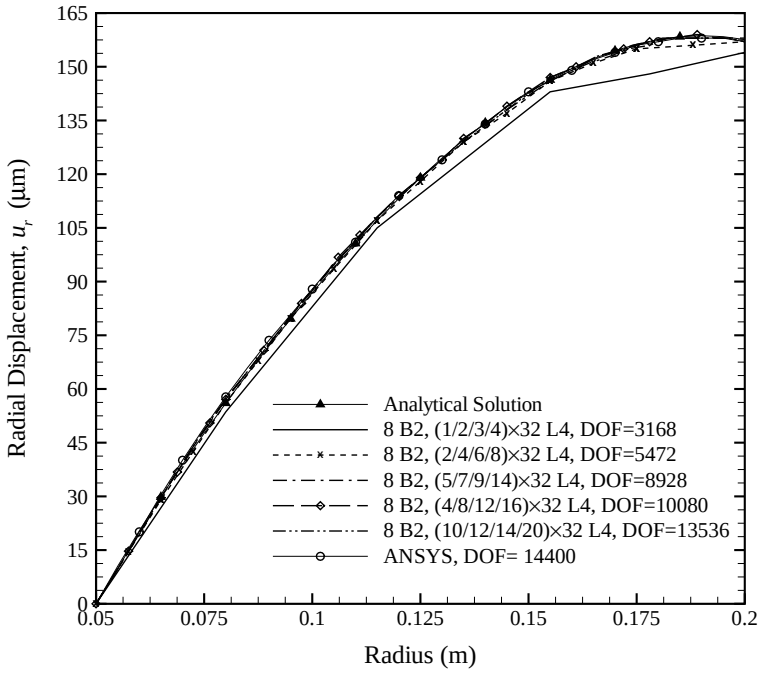

Fig. 3.13 Radial distribution of radial displacement at the middle plane perpendicular to the axis of the variable thickness disk for the different meshes over the cross-sections.

In Table 3.6, values of the stresses, σ_{rr} and $\sigma_{\theta\theta}$, at mid-radius ($r = 0.125$ (m)) of the model for the different meshes are given and compared with the reference solutions. The table shows that with the increase of the number of discretized elements through the radius, the convergence of the stresses can be achieved. Furthermore, the results presented in the table may emphasize that a proper mesh of the elements over the cross-sections of the model can be effective in detecting the solid-like solution.

Table 3.6 Comparison of stresses at mid-radius of the variable thickness disk for the different meshes over the cross-sections.

Model	DOFs	σ_{rr} (MPa)	$\sigma_{\theta\theta}$ (MPa)
Analytical	1	313.19	284.78
8 B2, $(1/2/3/4)\times 32$	3168	$303.37^{(3.14)}$	$275.75^{(3.17)}$
8 B2, $(2/4/6/8)\times 32$	5472	$311.25^{(0.62)}$	$281.25^{(1.24)}$
8 B2, $(5/7/9/14)\times 32$	8928	$308.37^{(1.54)}$	$282.87^{(0.67)}$
8 B2, $(4/8/12/16)\times 32$	10080	$311.00^{(0.7)}$	$285.50^{(0.25)}$
8 B2, $(10/12/14/20)\times 32$	13536	$307.50^{(1.82)}$	$282.50^{(0.8)}$
3D FE (ANSYS)	14400	$308.00^{(1.66)}$	$285.00^{(0.08)}$

$^{()}$ = absolute percentage difference with respect to the analytical solution.

Moreover, radial distributions of the stresses are plotted in Fig. 3.14 for the different meshes over cross-sections of the model (2). Remarkable improvements in the stress distributions, especially at vicinity of the boundaries, are observed by refining the meshes.

It should be noted that the stresses are obtained from the computed nodal displacements and, therefore, may be considered as derivative quantities in FEM. In other words, once the FE matrix equations are solved for displacement field at the nodes, in postprocessing these derivative quantities are calculated and graphically displayed. The calculated stresses at the mutual nodal point between adjacent elements over the cross-section are not generally identical. This causes jumps in the stresses at the boundary between any two adjacent elements. Many techniques have been proposed in literatures to overcome these discontinuities and improve accu-

racy of the stress distributions such as averaged simple nodal evaluation, averaged extrapolation using a reduced polynomial, and continuous and discrete smoothing methods on elements. Depending on numerical technique used to calculate the stresses, the accuracy of the derivative quantities is generally lower than that of the displacements, especially, at boundaries of the disk. In the present study, the averaged extrapolation technique using a reduced polynomial is employed to recover the stresses and to smooth out the jumps in curves of the stress distributions, as shown in Figs. 3.11 and 3.14.

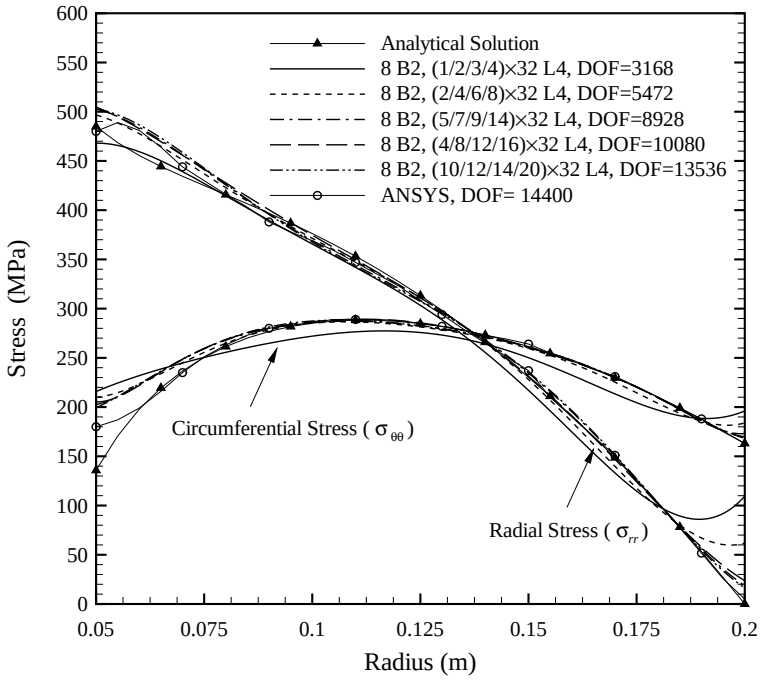

Fig. 3.14 Radial distribution of radial stress at the middle plane perpendicular to the axis of the variable thickness disk for the different L4 distributions.

It can also be observed from Figs. 3.11 and 3.14 that there are some minor differences between the analytical and the converged FE solutions for stresses at the inner radius of the disk. The reason may be due to the different definitions of the clamped boundary conditions in the analytical and the FE models. The closed form solutions related to the analytical method for the stresses are obtained under axisymmetric plane stress assumptions. It should be mentioned that in axisymmetric problems all quantities are independent of the circumferential variable θ, as well as the circumferential displacement, u_θ, is assumed to be zero. Thus, the components

of radial and circumferential stresses (σ_{rr} and $\sigma_{\theta\theta}$) are the only non-zero stresses. In addition, in the analytical model the clamped conditions at the inner radius of the disk is defined as $u_r = 0$. In the FE models, however, all components of displacement and stress fields in any direction are involved in the solution and the clamped constraints are simulated by using zero displacement field ($u_r = u_\theta = u_{z^*} = 0$) in all nodes located on the inside surface of the disk.

3.5.3 Rotating disk with variable thickness subjected steady-State temperature gradient

An annular disk with variable thickness subjected to centrifugal and thermal loads is analyzed to validate the formulation presented in the previous section. The inner and outer radii of the disk, whose thickness varies according to the hyperbolic function $h(r) = 0.013r^{-0.5}$, are assumed to be $r_{\text{in}} = 0.05\,\text{m}$ and $r_{\text{out}} = 0.2\,\text{m}$. This disk, made of a nickel based alloy (λ=100.38 GPa, μ=66.92 GPa, $\alpha = 16.3 \times 10^{-6}\,1/^{\circ}\text{C}$), is rotating at $\omega = 1497.5\,\text{rad/s}$. The inner radius may be considered fully fixed (the zero displacements) or deformable on the *xz* plane ($u_y = 0$), while other boundaries are free of surface tractions and concentrated loads. The temperature at the inner and outer radii is supposed to be $T_{\text{in}} = 537$ and $T_{\text{out}} = 614^{\circ}\text{C}$, while the reference temperature is $T_0 = 20^{\circ}\text{C}$. The variation of temperature is assumed to occur in the radial direction only, such that the radial steady-state temperature distribution in the disk can be considered as uniform, linear, parabolic and exponential (Eq. 3.38)

$$\begin{aligned} T(r) &= T_{\text{out}} \\ T(r) &= T_{\text{in}} + (T_{\text{out}} - T_{\text{in}})(r - r_{\text{in}})/(r_{\text{out}} - r_{\text{in}}) \\ T(r) &= T_{\text{in}} + (T_{\text{out}} - T_{\text{in}})(r - r_{\text{in}})^2/(r_{\text{out}} - r_{\text{in}})^2 \\ T(r) &= T_{\text{in}} + (T_{\text{out}} - T_{\text{in}})\ln(r/r_{\text{in}})/\ln(r_{\text{out}}/r_{\text{in}}) \end{aligned} \tag{3.38}$$

The different temperature distributions along the radial direction are plotted in Fig. 3.15.

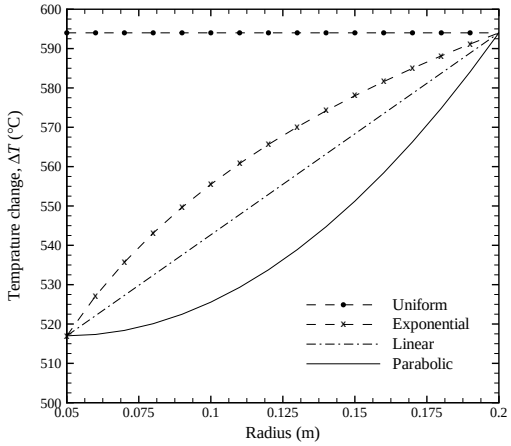

Fig. 3.15 Different distributions of temperature change along radius of the disk.

To solve this problem, the geometry of the disk is discretized into 10 B2 elements along its axis. As shown in Fig. 3.16, the length of these elements are unequal, and the cross sections are selected closely together where there is sudden change in geometry of the disk.

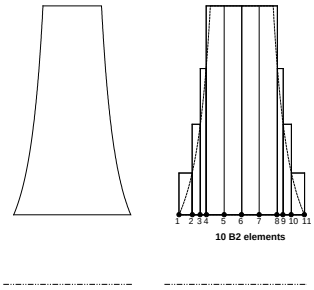

(a) (b)

Fig. 3.16 Discretization of variable thickness disk along the axis based on 1D CUF (a) disk profile, (b) discretization into 10 B2 with four different cross sections.

A number of L4, L9 and L16 elements can be used to describe the deformations over the cross sections. Figure 3.16 clearly shows that, due to symmetry of the disk profile with respect to the middle plane perpendicular to the axis, four different types of cross section are needed to generate the FE model. Three types of meshes, which are indicated as $(1/2/3/4) \times 32$, $(2/4/6/8) \times 32$ and $(4/8/12/16) \times 32$, are considered over the four cross sections in this example. For instance, in the case of $(4/8/12/16) \times 32$, the number of Lagrange elements in the circumferential direc-

tion of the four cross sections is 32, while these cross sections, from the smaller to the larger, are divided into 4, 8, 12 and 16 elements, respectively, along the radial direction. Figure 3.17 shows the different types of meshes used for the Lagrange elements over the four cross sections.

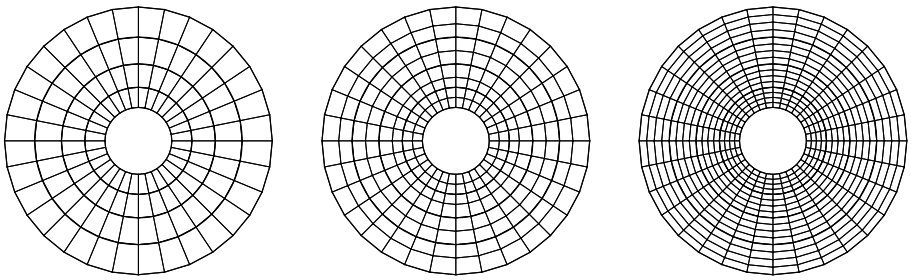

(a) $(1/2/3/4)\times 32$ (b) $(2/4/6/8)\times 32$ (c) $(4/8/12/16)\times 32$

Fig. 3.17 Three different types of meshes used for the Lagrange elements over the cross sections.

Assuming that the disk is subjected to the parabolic distribution of temperature and its inner radius is fully fixed, non-dimensional radial displacement ($\hat{u}_r$) for the point located at the mid-radius of the disk (r = 0.125 (m)) in the cross section related to the beam node 6 (see Fig. 3.16-(b)) for the three different meshes and types of elements are presented and compared with an exact solution in Table 3.7. The non-dimensional radial displacement is defined as $\hat{u}_r = u_r/u_0$ where $u_0 = r_{\text{out}}\alpha\Delta T_{\text{out}} + (\rho\omega^2 r_{\text{out}}^3)/E$. In this table, the computational costs of each model are provided in terms of DOFs which is determined by Eq. (4.39). The exact solution can be obtained using relations given in Ref. [63] for hyperbolic disks subjected thermal loads.

Table 3.7 Non-dimensional displacement at mid-radius of the disk for the different LEs and meshes on the four cross section.

Mesh	Element	DOFs	$\hat{u}_r$	Diff.* (%)
$(1/2/3/4)\times 32$	L4	4128	0.3497	2.91
	L9	14400	0.3486	2.59
	L16	30816	0.3487	2.62
$(2/4/6/8)\times 32$	L4	7200	0.3487	2.62
	L9	26688	0.3487	2.62
	L16	58464	0.3489	2.67
$(4/8/12/16)\times 32$	L4	13344	0.3486	2.59
	L9	51264	0.3487	2.62
	L16	93760	0.3488	2.64

*Absolute percentage difference with respect to the exact solution.

The comparisons show that the difference between the solutions obtained with the different CUF models and the reference exact solution is less than 3 percent. The maximum error for the nodal displacement is 2.91% that is related to the mesh $(1/2/3/4)\times 32$ with L4 elements. Using the same discretization, if L9 elements are used, the error is reduced to 2.59% while the number of DOFs increases from 4128 to 14400. It means that using $(1/2/3/4)\times 32$ L9 over the cross sections with almost 3.5 times more DOFs, accuracy of the solution is increased about 11%. Furthermore, the use of L16 elements, compared to L4, in the $(1/2/3/4)\times$ 32 mesh leads to increase of about 10% in the accuracy and 7.5 times more DOFs.

For the L4 elements, it is observed that improvements in the solution accuracy can be achieved by enriching the discretization along the radius. Indeed, for the $(2/4/6/8)\times 32$ distribution, the error with respect to the exact solution becomes 2.62% that is about 10% lower than the difference obtained with the $(1/2/3/4)\times 32$ mesh. A further improvement has been achieved by using the $(4/8/12/16)\times 32$. From the computational point of view, the numbers of DOFs with respect to the coarsest L4 mesh are increased of 1.7 and 3.2 times, respectively.

In addition, it can be observed from Table 3.7 that the rate of convergence of L9 model is higher than L4. The reason is that L9 element uses quadratic polynomials as interpolation functions to approximate the displacement field, while polynomials related to L4 element are of a bilinear type, see Eqs. (3.13) and (3.14). Therefore,

increasing numbers of L4 elements on a cross section in the radial direction can be very effective. On the other hand, the use of higher-order LEs (for example the L16 cubic element) may lead to a negative effect on accuracy of the solution, although the computational cost increases.

Consequently, the comparisons in Table 3.7 reveal that an appropriate distribution of the Lagrange elements and type of element used over the cross sections can lead to a reduction in computational costs and the convergence of results. Therefore, for this example, the $(2/4/6/8) \times 32$ mesh with L4 elements over the cross sections may be sufficient to obtain a converged result.

In Figs. 3.18 and 3.19, distributions of radial displacement (u_r), radial stress (σ_{rr}) and circumferential stress ($\sigma_{\theta\theta}$) related to the sixth beam node, are plotted and compared with the results obtained by analytical and FD methods (given in Refs. [63] and [51], respectively). The constraint on the displacement field at the inner radius is such that the displacements in *x* and *z* directions are allowed, while the displacement in *y* direction is prevented. The disk is still subjected to the parabolic temperature gradient along its radius. Moreover, in Figs. 3.18 and 3.19, the CUF curves are related to the model with $(2/4/3/4) \times 32$ L4 elements. Figure 3.18 shows distribution of the radial displacement along the radius of the disk. Excellent agreement is observed between the results of the presented model and those obtained using the analytical and FD solutions.

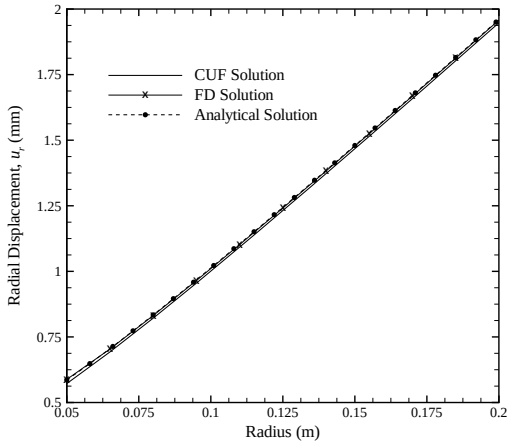

Fig. 3.18 Distribution of radial displacement along the radius at the middle plane perpendicular to the axis of the disk.

The distributions of averaged radial and circumferential stresses along the radius of the disk are plotted in Fig. 3.19. It is seen that the presented results are in close agreement with the references solutions.
It should be mentioned that in a displacement-based FE model, stresses are considered as derivative quantities which are directly derived from the nodal displacements through postprocessing methodologies. Depending on the numerical technique used to calculate stresses, the accuracy of the derivative quantities is generally lower than that of the displacements, especially, at the structure boundaries. Furthermore, the calculated stresses at the mutual nodal point between adjacent elements over the cross section are not generally identical. This nodal discrepancy determines jumps in the stress distributions at the boundary between any two adjacent elements. Therefore, techniques of stress averaging may be employed to improve the stress accuracy and to smooth out these jumps in curves of stress distributions.

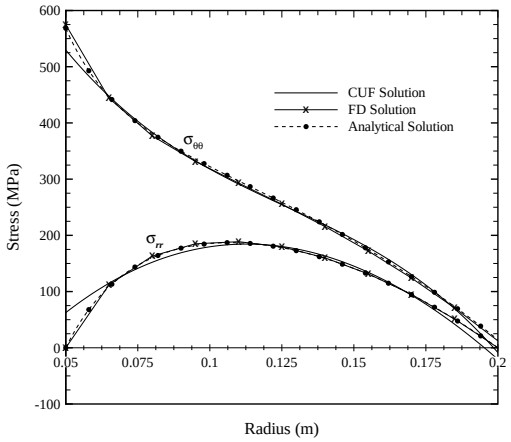

Fig. 3.19 Distribution of radial and circumferential stresses along the radius at the middle plane perpendicular to the axis of the disk.

Contour plots of the field variables can be preferred to show variations of a field along the model or mesh. Recalling capability of the presented 1D CUF approach to provide 3D-like solutions, the obtained results can be displayed as 2D or 3D contour plots (see Fig. 3.20-(a) for instance) by a proper postprocessing.
In Figs. 3.20-3.22, the contour plots related to the radial displacement, radial stress, and circumferential stress are shown on an axisymmetric plane, for two different boundary conditions. In particular, Fig. 3.20 shows the radial thermoelastic displacements u_r for the fully fixed disk at inner radius as well as the axial constrained

disk at inner radius. As expected, the maximum deformation of the fully fixed disk is higher than that one of the axially constrained disk.

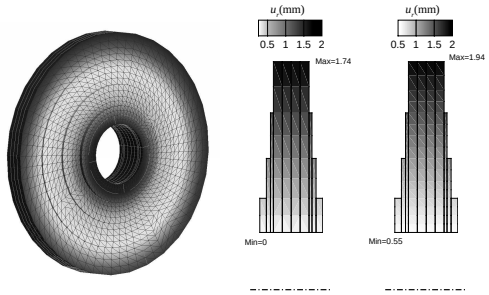

(a) (b) (c)

Fig. 3.20 Distribution of radial displacement on CUF model of the disk (a) fully fixed at inner radius, (b) axial constrained at inner radius.

Figure 3.21 represents the contour plots for the radial stress in the disk under the two different boundary conditions. As shown in this figure, the maximum value of radial stress for the fixed condition occurs at inner surface of the disk and it is significantly higher than the maximum value predicted for the disk with a radial deformable inner surface. The maximum radial thermoelastic stress for a disk, which is only constrained in the axial direction, occurs roughly at the mid-radius.

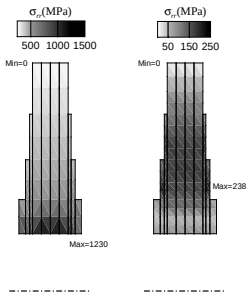

(a) (b)

Fig. 3.21 Distribution of radial stress on CUF model of the disk (a) fully fixed at inner radius, (b) axial constrained at inner radius.

The contour plots related to circumferential stress in the disk are shown in Fig. 3.22. If the inner surface of the disk is fully fixed, the values of circumferential stress is very high compared to the axial constrained disk.

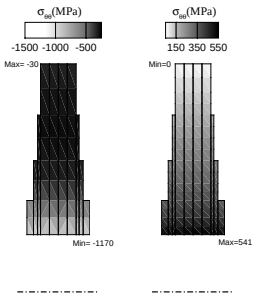

(a) (b)

Fig. 3.22 Distribution of circumferential stress on CUF model of the disk (a) fully fixed at inner radius, (b) axial constrained at inner radius.

In the case of a non-rotating disk (zero angular velocity) that is fully fixed at its inner radius, assuming thermal loading only, the non-dimensional thermal displacement and stresses distributions are presented in Figs. 3.23 and 3.24 for different temperature profiles. These distributions are related to the cross section in the beam node 6 which is shown in Fig. 3.16-(b). The non-dimensional thermal displacement and stresses are defined as

$$\hat{u}_r^{\mathrm{t}} = \frac{u_r}{u_0^{\mathrm{t}}} \quad , \quad \hat{\sigma}_{rr}^{\mathrm{t}} = \frac{\sigma_{rr}}{\sigma_0^{\mathrm{t}}} \quad , \quad \hat{\sigma}_{\theta\theta}^{\mathrm{t}} = \frac{\sigma_{\theta\theta}}{\sigma_0^{\mathrm{t}}}$$

where $\sigma_0^{\mathrm{t}} = E\,\alpha\Delta T_{\mathrm{out}}$ and $u_0^{\mathrm{t}} = r_{\mathrm{out}}\alpha\Delta T_{\mathrm{out}}$. It can be seen from Fig. 3.23 that, when the fixed disk is exposed to a uniform temperature, the radial deformation due to the thermal expansion is higher than that produced by a temperature gradient along the radius. A similar description may be presented for the radial and circumferential stresses in Fig. 3.24.

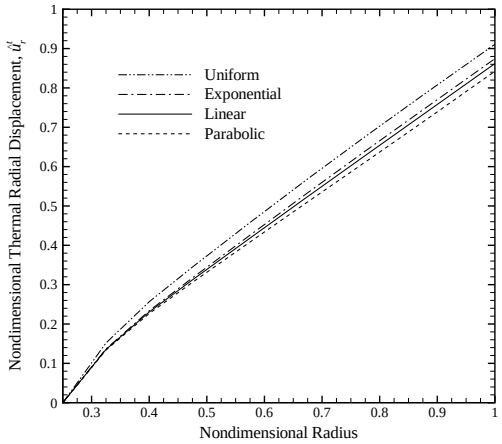

Fig. 3.23 Non-dimensional thermal displacement distributions along the radius on node 6 for Fixed BC.

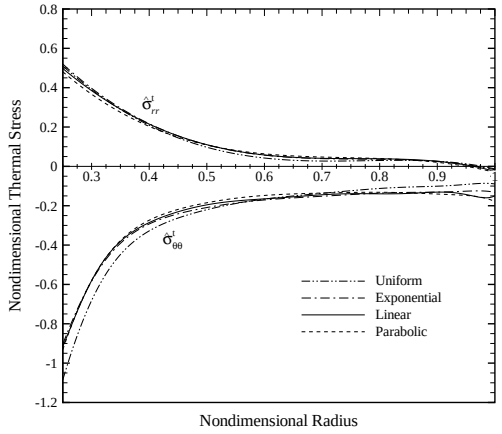

Fig. 3.24 Non-dimensional thermal stress distributions along the radius on node 6 Fixed BC.

3.5.4 Complex rotor

It should be recalled that rotors used in practical problems such as aircraft and industrial turbine engines have various configurations and are geometrically complex where the loading and boundary conditions are complicated. Some of these configurations can include; a disk-type rotor in which several disks, spacers and air seals with a shaft are clamped by tie bolts; a forged integrated drum-type rotor with rings to carry the blades that is bolted to adjacent disks on the forward and aft flanges,

a welded-type rotor in which a special welding method is used to attach disks and spacers to each other. Moreover, there are various disk models such as ring, web and hyperbolic models which are used in the rotors.
In order to perform a detailed analysis, find a 3D state of stress and assess allowed stresses in the parts of theses complex rotors with various materials and with various loading conditions, and also to investigate interactions between adjacent parts on each other, the FEM are often preferred. Due to the iterative nature of design of such structures, the refined FEM in the 1D CUF framework can be effectively used to obtain the results that are only provided by 3D FE analysis, but with much lower computational costs as verified in the previous illustrative examples.
As the final example of this chapter, to show the performance of the presented 1D CUF approach for the analysis of complex rotors, consider a rotor that is composed of one turbine disk and two compressor disks. These disks are mounted on an elastic hollow shaft, as shown in Fig. 3.25. The profile of the turbine disk has been assumed to be hyperbolic, however, two compressor disks have a web-type profile and are smaller in radius compared to the turbine disk. In this example, the profile of the turbine disk, the angular velocity of the rotor and the mechanical properties of the rotor material are identical to those of the previous example. Both ends of the shaft of this rotor are assumed to be fully fixed.

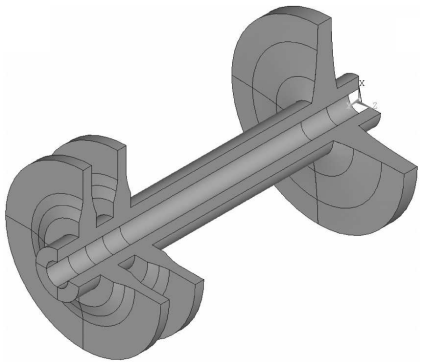

Fig. 3.25 3D model of a complex rotor.

Using a similar procedure to the previous example, the finite element model of the problem can be obtained by discretizing the rotor into some discrete beam elements through its axis. In this example as illustrated in Fig. 3.26, the geometry of the rotor is divided into 32 B2 elements along the axis, so that 8 B2 of these elements are employed for discretizing the disks and the shaft through the axis in the hub

zone. A distribution of the four-point Lagrange (L4) elements is considered over the cross-sections of the 1D FE model. Proper meshes of L4 elements over the cross-sections can be choose through a convergence analysis. Thus, the model with the mesh 1×32 over the shaft cross-section, as well as the meshes $(4/6/8/16)\times32$ and $(4/5/6/12)\times32$, respectively, over the cross-sections of turbine and compressor disks may be sufficient for reaching a convergent solution. In this case, the number of total DOFs of the model is equal to 27072.

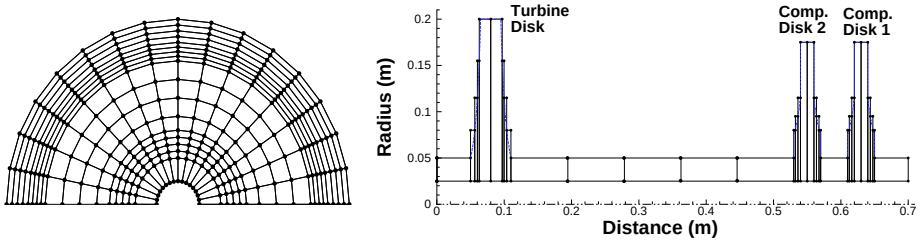

(a) (b)

Fig. 3.26 A 1D CUF FE model of the complex rotor, with DOFs= 27072 (a) The mesh of L4 elements over the cross-section with the largest radius, (b) The mesh of B2 elements in the axial direction.

Using the CUF approach, 3D distributions of all of the three components of displacement and the six components of stress and strain can be obtained. Since radial displacement (u_r), radial stress (σ_{rr}) and circumferential stress ($\sigma_{\theta\theta}$) are often more important in structural analysis and design of such structures, therefore, in this example only distributions of these components are represented in Figs. 3.27-3.30.
In order to verify the accuracy of the 1D CUF model, the present solution is compared with the result of a 3D stress analysis obtained by ANSYS in Figs. 3.27 and 3.28 as well. The converged solid model in the ANSYS solution with 44280 total DOFs has been generated by 10160 8-node solid elements.
Figures 3.27 and 3.29 show the contour plots as two-dimensionally in an axisymmetric plane for the displacement and the stresses on the CUF model of the rotor. These contour plots may be preferred to display variations of the field variables along the model or the mesh.
Furthermore, Fig. 3.28 shows the variation of radial displacement through the radial direction at the middle plane perpendicular to the axis of the rotor disks which are mounted on the elastic shaft. In this figure, as well as the converged displacement distribution for the single disk presented in the previous example with rigid hub (Fig. 3.7) is plotted. It is seen from Fig. 3.28 that the solution of the present model for

the turbine disk has excellent agreement with the solution of ANSYS. Also, Figs. 3.27 and 3.28 reveal that the proposed 1D model is able to detect the solid solution perfectly, with a significant reduction in the computational costs.

Also, the distribution of the stresses for the turbine disk mounted on the elastic shaft and the single disk with rigid hub are presented in Fig 3.30. The interactions between the shaft and the disks and the effect of mechanical boundary conditions in the hub on the deformation and stresses distributions in the turbine disk can be clearly observed from Figs. 3.28 and 3.30. As expected, it may be seen in Fig. 3.28 that with the decrease of rigidity in the inner radius of a rotating disk, the radial deformation of the disk is increased. For example in this figure, the total radial deformation of the turbine disk mounted on the elastic shaft is about 20% larger than that of the disk with rigid hub. On the other hand, as seen in Fig. 3.30, the maximum radial stress for the rigid hub conditions occurs at the inner surface and it is greater than its corresponding value for the disk with elastic hub conditions. Furthermore, if effect of the elastic shaft is taken into account, the maximum circumferential stress occurs at the inner surface of the disk, while for the disk with rigid hub this value is close to mid-radius of the disk.

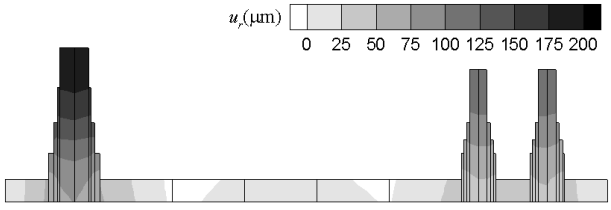

(a)

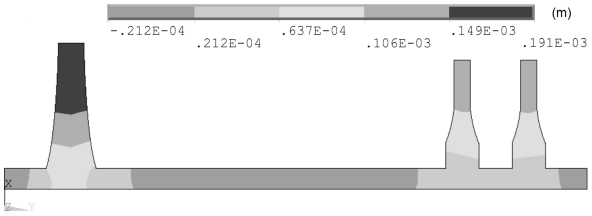

(b)

Fig. 3.27 Distribution of the radial displacement on the complex rotor (a) 1D CUF solution with 27072 DOFs, (b) 3D ANSYS solution with 44280 DOFs .

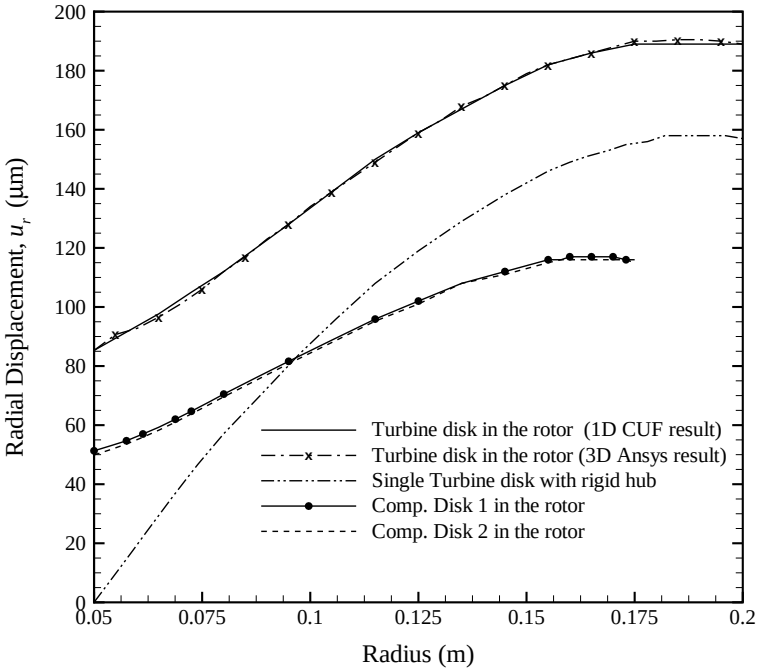

Fig. 3.28 Radial distribution of radial displacement.

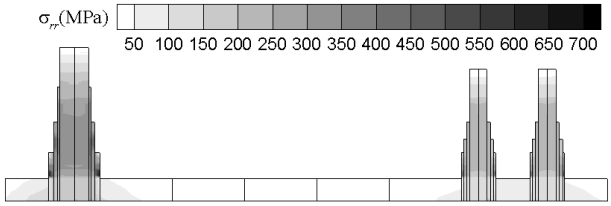

(a) Radial stress

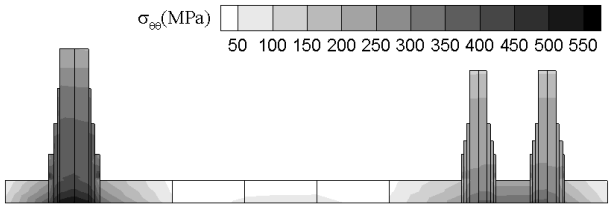

(b) Circumferential stress

Fig. 3.29 Distribution of the radial and circumferential stresses on the CUF model of the complex rotor.

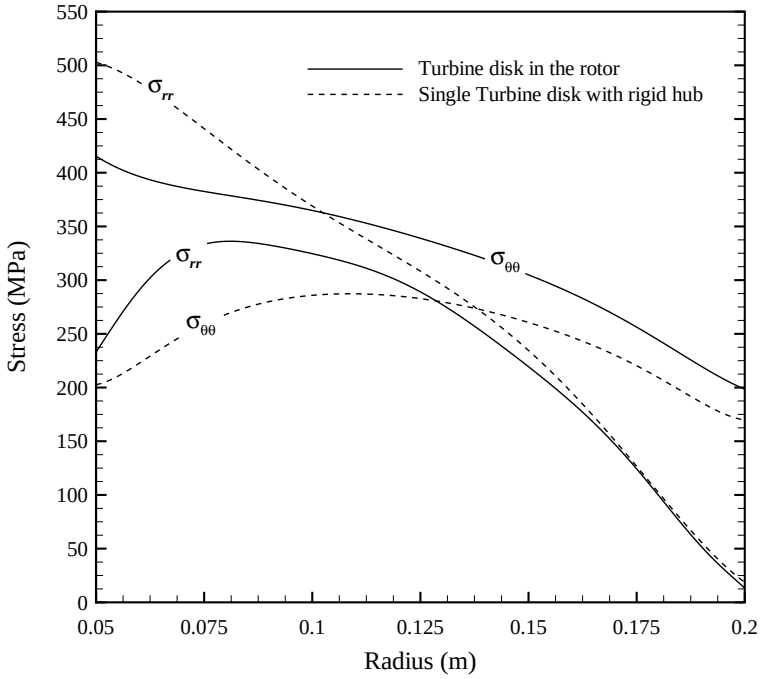

Fig. 3.30 Radial distribution of the stresses in turbine disk.

3.6 Summary

In this chapter, the 1D refined FE method based on the CUF was extended for steady-state thermoelastic analysis of rotating disks with an arbitrary geometry. The governing FE formulation was developed for the disks made of heterogeneous anisotropic materials that are subjected to arbitrary thermal, surface, and concentrated loads. To validate the proposed formulation, the results obtained for different numerical examples were compared with those obtained using analytical, 1D finite difference and 3D FE solutions, which showed good agreement.

Chapter 4

Development of 1D FE-CUF approach for dynamic coupled thermoelasticity

Since the time history analysis of the dynamic thermoelastic problems is very time consuming, the reduced FE models have been recommended to obtain the solutions with lower computational effort. Thus, in this chapter, a novel FE approach refined through the CUF is developed for the dynamic generalized coupled thermoelastic analysis of 3D beam-type structures.

4.1 Governing equations of coupled thermoelasticity

The equation of motion for a 3D elastic body in the physical coordinate system (x,y,z) is stated as follows [41, 49]

$$\sigma_{ij,j} + X_i = \rho \ddot{u}_i + \zeta \dot{u}_i \tag{4.1}$$

where σ_{ij} and u_i are stress and displacement components, respectively. X_i denotes body forces per unit volume, ρ is mass density, and ζ stands for the damping coefficient of the material. Likewise, the superscript dot $(\cdot)$ and the subscript comma $(,)$ indicate the derivatives with respect to the time (t) and the space variables (x,y,z), respectively.

In addition, the strain-displacement relations within the linear context of small deformation theory are expressed as [41]

$$\varepsilon_{ij} = \frac{1}{2}(u_{i,j} + u_{j,i}) \tag{4.2}$$

and according to GL generalized theory, Hooke's law for a nonhomogeneous anisotropic thermoelastic material can be written as [41]

$$\sigma_{ij} = C_{ijpq}\varepsilon_{pq} - \beta_{ij}(T + t_1\dot{T}) \tag{4.3}$$

where C_{ijpq} is a fourth-order tensor containing all the elastic coefficients of a general nonhomogeneous anisotropic material. $\beta_{ij} = C_{ijpq}\alpha_{pq}$ is the second order tensor of thermoelastic moduli where in α_{ij} is the coefficient of thermal expansion tensor. In Eq. (4.3), T denotes the temperature change relative to the reference temperature T_0, so that this temperature difference creates thermal strain. Also, t_1 is one of the two relaxation times defined by Green and Lindsay.
On the other hand, the energy balance equation can be expressed as [41]

$$q_{i,i} = R - T_0\dot{\mathrm{S}} \tag{4.4}$$

where q_i is heat flux vector and R stands for internal heat source per unit volume per unit time. S denotes entropy per unit volume and is given by the following relationship [41]

$$\mathrm{S} = \frac{\rho c}{T_0}(T + t_2\dot{T}) + \beta_{ij}\varepsilon_{ij} - \frac{1}{T_0}\tilde{c}_i T_{,i} \tag{4.5}$$

Here, c is specific heat, while t_2 and $\tilde{c}_i$ are another relaxation time and a vector of material new constants, respectively, proposed by Green and Lindsay. Moreover, based on LS and GL theories of thermoelasticity the heat conduction equation for an anisotropic material can be stated as [41]

$$q_i + t_0\dot{q}_j = -\kappa_{ij}T_{,j} - \tilde{c}_i\dot{T} \tag{4.6}$$

where κ_{ij} is the thermal conductivity tensor and t_0 is relaxation time associated with LS theory.
Equations (4.1) to (4.3) may be combined to give the equation of motion in term of

the displacement components as

$$(C_{ijkl}u_{k,l})_{,j} - (\beta_{ij}T)_{,j} - (t_1\beta_{ij}\dot{T})_{,j} + X_i = \rho\ddot{u}_i + \zeta\dot{u}_i \tag{4.7}$$

Likewise, by using Eqs. (4.4)-(4.6) and Eq. (4.2), the energy equation can be expressed in terms of the temperature and displacement fields as

$$\begin{aligned} &\rho c(t_0+t_2)\ddot{T} + \rho c\dot{T} - 2\tilde{c}_i\dot{T}_{,i} - (\kappa_{ij}T_{,j})_{,i} \\ &+t_0T_0\beta_{ij}\ddot{u}_{i,j} + T_0\beta_{ij}\dot{u}_{i,j} = R + t_0\dot{R} \end{aligned} \tag{4.8}$$

Equations (4.7) and (4.8) constitute the governing system of equations for the generalized coupled thermoelasticity problems based on the LS (for $t_1 = t_2 = \tilde{c}_i = 0$) and GL (for $t_0 = 0$) theories in an anisotropic and nonhomogeneous medium. In these equations, the derivatives of the relaxation times and $\tilde{c}_i$ with respect to position variables are ignored. Thus, the four coupled equations, including three equations of motion and one heat conduction equation, under specified initial and boundary conditions must be simultaneously solved for the three unknown displacement components (u_i) and the one unknown temperature change (T).

4.2 FE formulation through Galerkin technique

To obtain a FE formulation of the governing equations (4.7) and (4.8), Galerkin technique may be utilized. In implementation of the conventional FE method, the 3D domain with the volume V can be discretized into a finite number of regular 3D solid elements. Thus, the components of displacement and temperature change in each base element can be approximated by identical shape functions as follows

$$\begin{aligned} u_i^{(e)}(x,y,z,t) &= \phi_m(x,y,z)U_i^m(t) \\ T^{(e)}(x,y,z,t) &= \phi_m(x,y,z)\Theta^m(t) \end{aligned} \tag{4.9}$$

where $U_i^m(t)$ and $\Theta^m(t)$ are the displacement vector and the temperature change at each nodal point of the element. $\phi_m(x,y,z)$ denotes shape functions in the base element. It is noted that in these approximations, time and space variables are separated into distinct functions. Furthermore, the repeated subscript $m\,(m = 1,\cdots,r)$ is a dummy index and indicates summation while r stands for the number of nodal points in the element [30, 41].

According to Galerkin method, multiplying both sides of Eq. (4.1) by the shape functions ϕ_m and then integrating over volume of the element, yields

$$\int_{V^{(e)}} \left(\sigma_{ij,j} + X_i - \rho\ddot{u}_i - \zeta\dot{u}_i\right)\phi_m dV = 0 \tag{4.10}$$

On the first term of Eq. (4.10) the divergence theorem can be applied as

$$\int_{V^{(e)}} \left(\sigma_{ij,j}\right)\phi_m dV = \int_{S^{(e)}} \sigma_{ij}n_j\phi_m dS - \int_{V^{(e)}} \phi_{m,j}\sigma_{ij}dV \tag{4.11}$$

where n_j is the unit vector normal to the boundary surface of the element $S^{(e)}$. Substituting relation (4.11) into Eq. (4.10) gives

$$\begin{aligned}&\int_{S^{(e)}} \sigma_{ij}n_j\phi_m dS - \int_{V^{(e)}} \phi_{m,j}\sigma_{ij}dV + \int_{V^{(e)}} \left(X_i\phi_m\right)dV \\ &- \int_{V^{(e)}} \left(\rho\ddot{u}_i\phi_m\right)dV - \int_{V^{(e)}} \left(\zeta\dot{u}_i\phi_m\right)dV = 0\end{aligned} \tag{4.12}$$

Furthermore, by using the relationship between the traction vector (t_i^n) acting on an arbitrary surface and the stress tensor, the first integral in Eq. (4.12) may be expressed as

$$\int_{S^{(e)}} \sigma_{ij}n_j\phi_m dS = \int_{S^{(e)}} \mathrm{t}_i^n\phi_m dS \tag{4.13}$$

Therefore, Eq. (4.12) can be rewritten as follows

$$\begin{aligned}&\int_{V^{(e)}} \left(\rho\ddot{u}_i\phi_m\right)dV + \int_{V^{(e)}} \left(\zeta\dot{u}_i\phi_m\right)dV + \int_{V^{(e)}} \left(\phi_{m,j}\sigma_{ij}\right)dV \\ &= \int_{V^{(e)}} X_i\phi_m dV + \int_{S^{(e)}} \mathrm{t}_i^n\phi_m dS\end{aligned} \tag{4.14}$$

Similarly, applying Galerkin method to the energy equation (4.8) gives

$$\begin{aligned}&\int_{V^{(e)}} \Big(\rho c(t_0+t_2)\ddot{T} + \rho c\dot{T} - 2\tilde{c}_i\dot{T}_{,i} - \left(\kappa_{ij}T_{,j}\right)_{,i} \\ &+t_0T_0\beta_{ij}\ddot{u}_{i,j} + T_0\beta_{ij}\dot{u}_{i,j} - R - t_0\dot{R}\Big)\phi_m dV = 0\end{aligned} \tag{4.15}$$

where the weak form of the term $(\kappa_{ij}T_{,j})_{,i}$ can be written according to the divergence theorem as

$$\int_{V^{(e)}} \left(\kappa_{ij}T_{,j}\right)_{,i}\phi_m dV = \int_{S^{(e)}} \left(\kappa_{ij}T_{,j}n_i\phi_m\right) dS - \int_{V^{(e)}} \left(\kappa_{ij}T_{,j}\phi_{m,i}\right) dV \tag{4.16}$$

and likewise substituting this form into Eq. (4.15) and rearranging the terms result in the following

$$\begin{aligned}
&\int_{V^{(e)}} (t_0 T_0 \beta_{ij}\ddot{u}_{i,j}\phi_m)dV + \int_{V^{(e)}} (t_0\rho c\ddot{T}\phi_m)dV + \int_{V^{(e)}} (t_2\rho c\ddot{T}\phi_m)dV \\
&+ \int_{V^{(e)}} (T_0\beta_{ij}\dot{u}_{i,j}\phi_m)dV + \int_{V^{(e)}} (\rho c\dot{T}\phi_m)dV - \int_{V^{(e)}} (2\tilde{c}_i\dot{T}_{,i}\phi_m)dV \\
&+ \int_{V^{(e)}} (\kappa_{ij}T_{,j}\phi_{m,i})dV = \int_{S^{(e)}} (q_i n_i\phi_m)dS + \int_{V^{(e)}} (R\phi_m)dV + \int_{V^{(e)}} (t_0\dot{R}\phi_m)dV
\end{aligned} \tag{4.17}$$

The system of equations (4.17) and (4.14) as well as the stress-strain relations (4.3) may be expressed in vector form as

$$\begin{aligned}
&\int_{V^{(e)}} (\rho\ddot{\mathbf{u}}\phi_m)dV + \int_{V^{(e)}} (\zeta\dot{\mathbf{u}}\phi_m)dV + \int_{V^{(e)}} (\mathbf{D}^{\mathrm{T}}\phi_m\sigma)dV \\
&= \int_{V^{(e)}} (\mathbf{X}\phi_m)dV + \int_{S^{(e)}} (\mathbf{t}\phi_m)dS
\end{aligned} \tag{4.18}$$

$$\begin{aligned}
&\int_{V^{(e)}} (t_0 T_0 \beta^{\mathrm{T}}\mathbf{D}\ddot{\mathbf{u}}\phi_m)dV + \int_{V^{(e)}} (t_0\rho c\ddot{T}\phi_m)dV + \int_{V^{(e)}} (t_2\rho c\ddot{T}\phi_m)dV \\
&+ \int_{V^{(e)}} (T_0\beta^{\mathrm{T}}\mathbf{D}\dot{\mathbf{u}}\phi_m)dV + \int_{V^{(e)}} (\rho c\dot{T}\phi_m)dV - \int_{V^{(e)}} (2\tilde{\mathbf{c}}^{\mathrm{T}}\nabla\dot{T}\phi_m)dV \\
&+ \int_{V^{(e)}} (\nabla^{\mathrm{T}}T\kappa\nabla\phi_m)dV = \int_{S^{(e)}} (\mathbf{q}^{\mathrm{T}}\mathbf{n}\phi_m)dS + \int_{V^{(e)}} (R\phi_m)dV + \int_{V^{(e)}} (t_0\dot{R}\phi_m)dV
\end{aligned} \tag{4.19}$$

$$\sigma = \mathbf{C}\varepsilon - \beta(T + t_1\dot{T}) \tag{4.20}$$

Equations (4.14) and (4.17), or (4.18) and (4.19), represent the general weak formulation containing all possible boundary conditions for the generalized coupled thermoelasticity problems.

4.3 1D FE-CUF approach for dynamic coupled thermoelastic problems

The 3D FE model presented in the previous Section, however, leads to more accurate results than the traditional 1D or 2D models, but the main drawback of this method is the significant increase of degrees of freedom (DOF) and, consequently, computational efforts. The computational competence is definitely reduced in a 3D model with enormous DOF especially in an iterative solution scheme of the dynamic coupled thermoelasticity problems. To lower the computational costs of such problems without loss of accuracy, refined 1D FE models in the framework of the CUF with 3D capabilities can be developed.

Consider an arbitrary structure subjected to thermo-mechanical shock loads which is located in the rectangular Cartesian coordinate system (x,y,z). As shown in Fig. 4.1, if the structure can be assumed as a beam along the *y*-direction, each cross section, whose centroid G, of the beam is defined in the *xz*-plane and perpendicular to the *y*-axis.

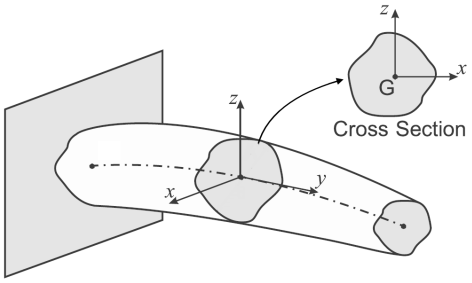

Fig. 4.1 A beam structure with an arbitrary cross section

According to the traditional 1D FE procedure, the structure can be discretized into a finite number of 1D beam elements along the *y*-axis. In this case, as illustrated in Fig. 4.2-a, the approximate displacement and temperature fields in each element can be obtained by the beam shape functions $N_m(y)$ as

$$\begin{aligned} \mathbf{u} &= N_m \mathbf{u}^m \\ T &= N_m T^m \end{aligned} \tag{4.21}$$

in which $\mathbf{u}^m$ and T^m are the nodal displacement vector and temperature change, respectively. In addition, the dummy index $m\,(m = 1, \cdots, M)$ denotes the summation and M is the number of nodes in the beam element.

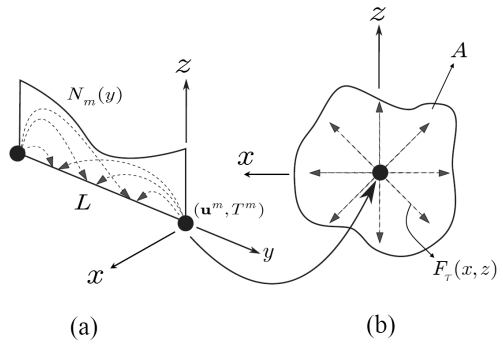

Fig. 4.2 A beam base element

On the other hand, based on the unified formulation for beams presented by Crarrea [17], to overcome the limitations of the classical beam theories such as the Euler-Bernoulli and the Timoshenko models, the distributions of displacements and the temperature over the cross section related to each node of the beam element can be described by an expansion of generic functions F_τ as

$$\begin{aligned} \mathbf{u}^m &= F_\tau \mathbf{U}^{m\tau} \\ T^m &= F_\tau \Theta^{m\tau} \end{aligned} \tag{4.22}$$

where F_τ are the functions of the cross section coordinates x and z (see Fig 4.2-b), $\mathbf{U}^{m\tau}(t) = \{U_x^{m\tau} \quad U_y^{m\tau} \quad U_z^{m\tau}\}^{\mathrm{T}}$ is the generalized displacement vector, and $\Theta^{m\tau}(t)$ denotes the generalized temperature change. Here, $\tau\,(\tau = 1, 2, \cdots, N_{\mathrm{CUF}})$ indicates summation, as well, while N_{CUF} is the number of terms of the expansion.
The hierarchical capabilities of the presented unified formulation (4.22) play a essential role in dealing with variable kinematic models in a compact unified manner. The order of the model is taken into account as a free parameter of the analysis (i.e., as input) in this formulation. In other words, the refined models can be obtained with no need for ad hoc formulations. In Fig. 4.3, a 3D 8-nodes element is schematically compared with a 1D 2-nodes element refined by the CUF.

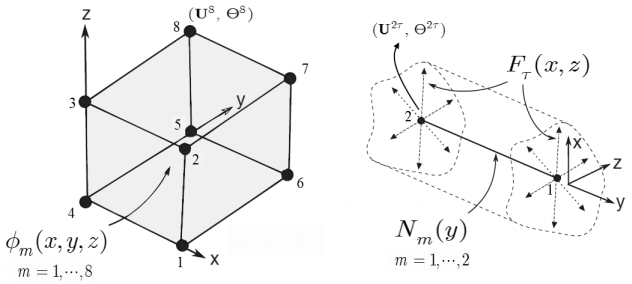

(a) (b)

Fig. 4.3 A schematic comparison between a 3D element and a refined 1D element, (a) a 3D 8-nodes element, (b) a refined 1D 2-nodes element.

Thus, comparing the relations (4.21) and (4.22) with Eq. (4.9) results in the following relationship

$$\phi_m(x,y,z) = N_m(y)F_\tau(x,z) \tag{4.23}$$

In this approach, three types of the beam element, two-, three- and four-nodes, may be used to give a linear, a quadratic and a cubic interpolation function of the displacement and temperature fields along the y-axis, respectively. Likewise, the selection of $F_\tau(x,z)$ and N_{CUF} is arbitrary. That is, various kinds of basic functions including polynomials, harmonics and exponentials of any-order can be assumed to predict the displacement components and temperature change on the beam cross section. For instance, different classes of polynomials such as Taylor, Legendre and Lagrange polynomials are extensively employed as approximation functions in the numerical modeling of structures. More details about the variable kinematic models and the interpolating functions can be found in [17].

4.4 FE equations of coupled thermoelasticity in CUF form

The relations (4.9) and (4.23) can be substituted into Eqs. (4.18) and (4.19) to give

$$\begin{aligned}
&\int_{V^{(e)}} (\rho N_l F_s N_m F_\tau)\ddot{\mathbf{U}}^{ls} dV + \int_{V^{(e)}} (\zeta N_l F_s N_m F_\tau)\dot{\mathbf{U}}^{ls} dV \\
&- \int_{V^{(e)}} (t_1 \mathbf{D}^{\mathrm{T}} N_m F_\tau \beta N_l F_s)\dot{\Theta}^{ls} dV + \int_{V^{(e)}} (\mathbf{D}^{\mathrm{T}} N_m F_\tau \mathbf{C}\mathbf{D} N_l F_s)\mathbf{U}^{ls} dV \\
&- \int_{V^{(e)}} (\mathbf{D}^{\mathrm{T}} N_m F_\tau \beta N_l F_s)\Theta^{ls} dV = \int_{V^{(e)}} (\mathbf{X} N_m F_\tau) dV + \int_{S^{(e)}} (\mathbf{t}^n N_m F_\tau) dS
\end{aligned} \tag{4.24}$$

$$\begin{aligned}
&\int_{V^{(e)}} (t_0 T_0 \beta^{\mathrm{T}} \mathbf{D} N_l F_s N_m F_\tau)\ddot{\mathbf{U}}^{ls} dV \\
&+ \int_{V^{(e)}} (t_0 \rho c N_l F_s N_m F_\tau + t_2 \rho c N_l F_s N_m F_\tau)\ddot{\Theta}^{ls} dV \\
&+ \int_{V^{(e)}} (T_0 \beta^{\mathrm{T}} \mathbf{D} N_l F_s N_m F_\tau)\dot{\mathbf{U}}^{ls} dV \\
&+ \int_{V^{(e)}} (\rho c N_l F_s N_m F_\tau - 2\mathbf{c}^{\mathrm{T}} \nabla N_l F_s N_m F_\tau)\dot{\Theta}^{ls} dV \\
&+ \int_{V^{(e)}} (\nabla^{\mathrm{T}} N_l F_s \kappa \nabla N_m F_\tau)\Theta^{ls} dV \\
&= \int_{S^{(e)}} (\mathbf{q}\mathbf{n} N_m F_\tau) dS + \int_{V^{(e)}} (R N_m F_\tau) dV + \int_{V^{(e)}} (t_0 \dot{R} N_m F_\tau) dV
\end{aligned} \tag{4.25}$$

here, the indexes s and l are similar to τ and m, respectively, and indicate summation based on Einstein's notation. Equations (4.24) and (4.25) render the 1D unified finite element formulation which can be employed to 3D analysis of the generalized coupled thermoelastic problems.

The presented approach enables all the FE matrix and vectors to derived as a condensed notation which is named the so-called *fundamental nucleus* (FN). Indeed, theses fundamental nuclei do not depend on either the order of the expansion or the base functions used. Accordingly, the Eqs. (4.24) and (4.25) can be rewritten in

matrix form as

$$\mathbf{M}^{lm\tau s}\ddot{\delta}^{m\tau} + \mathbf{G}^{lm\tau s}\dot{\delta}^{m\tau} + \mathbf{K}^{lm\tau s}\delta^{m\tau} = \mathrm{p}^{ls} \tag{4.26}$$

here, $\mathbf{M}^{lm\tau s}$, $\mathbf{G}^{lm\tau s}$ and $\mathbf{K}^{lm\tau s}$ which are 4×4 matrices, represent the *fundamental nucleus* (FN) of the total mass, damping, and stiffness matrices, respectively. Likewise, $\delta^{m\tau} = \{\mathbf{U}^{ls} \quad \Theta^{ls}\}^{\mathrm{T}}$ and $\mathrm{p}^{ls} = \{\mathbf{F}^{ls} \quad \hat{Q}^{ls}\}^{\mathrm{T}}$ indicate the nuclei of the unknowns and load vectors, respectively. Equation (4.26) may also be expressed as

$$\begin{bmatrix} \mathbf{M}_{UU}^{lm\tau s} & 0 \\ \mathbf{M}_{\Theta U}^{lm\tau s} & \mathbf{M}_{\Theta\Theta}^{lm\tau s} \end{bmatrix} \begin{Bmatrix} \ddot{\mathbf{U}}^{ls} \\ \ddot{\Theta}^{ls} \end{Bmatrix} + \begin{bmatrix} \mathbf{G}_{UU}^{lm\tau s} & \mathbf{G}_{U\Theta}^{lm\tau s} \\ \mathbf{G}_{\Theta U}^{lm\tau s} & \mathbf{G}_{\Theta\Theta}^{lm\tau s} \end{bmatrix} \begin{Bmatrix} \dot{\mathbf{U}}^{ls} \\ \dot{\Theta}^{ls} \end{Bmatrix} + \begin{bmatrix} \mathbf{K}_{UU}^{lm\tau s} & \mathbf{K}_{U\Theta}^{lm\tau s} \\ 0 & \mathbf{K}_{\Theta\Theta}^{lm\tau s} \end{bmatrix} \begin{Bmatrix} \mathbf{U}^{ls} \\ \Theta^{ls} \end{Bmatrix} = \begin{Bmatrix} \mathbf{F}^{ls} \\ Q^{ls} \end{Bmatrix} \tag{4.27}$$

where

$$\begin{aligned}
[\mathbf{M}_{UU}^{lm\tau s}]_{3\times3} &= \int_{L^{(e)}}\int_{A^{(e)}} (\rho N_m N_l \,\mathbf{I} F_\tau F_s)\, dA dL \\
[\mathbf{M}_{\Theta U}^{lm\tau s}]_{1\times3} &= \int_{L^{(e)}}\int_{A^{(e)}} (t_0 T_0 N_m N_l [\beta_p^{\mathrm{T}}(\mathbf{D}_p F_s) + \beta_n^{\mathrm{T}}(\mathbf{D}_{np} F_s)] F_\tau)\, dA dL \\
&\quad + \int_{L^{(e)}}\int_{A^{(e)}} (t_0 T_0 [\beta_n^{\mathrm{T}} N_m (\mathbf{D}_{ny} N_l) F_s F_\tau])\, dA dL \\
[\mathbf{M}_{\Theta\Theta}^{lm\tau s}]_{1\times1} &= \int_{L^{(e)}}\int_{A^{(e)}} (\rho c t_0 N_m N_l F_\tau F_s)\, dA dL \\
&\quad + \int_{L^{(e)}}\int_{A^{(e)}} (\rho c t_2 N_m N_l F_\tau F_s)\, dA dL
\end{aligned} \tag{4.28}$$

$$\begin{aligned}
[\mathbf{G}_{UU}^{lm\tau s}]_{3\times3} &= \int_{L^{(e)}}\int_{A^{(e)}} (\zeta N_m N_l \,\mathbf{I} F_\tau F_s)\, dA dL \\
[\mathbf{G}_{U\Theta}^{lm\tau s}]_{3\times3} &= -\int_{L^{(e)}}\int_{A^{(e)}} (t_1 N_m N_l [(\mathbf{D}_p^{\mathrm{T}} F_\tau \mathbf{I})\beta_p + (\mathbf{D}_{np}^{\mathrm{T}} F_\tau \mathbf{I})\beta_n] F_s)\, dA dL \\
&\quad - \int_{L^{(e)}}\int_{A^{(e)}} (t_1 (\mathbf{D}_{ny}^{\mathrm{T}} N_m) N_l [F_\tau \beta_n F_s])\, dA dL \\
[\mathbf{G}_{\Theta U}^{lm\tau s}]_{1\times3} &= \int_{L^{(e)}}\int_{A^{(e)}} (T_0 N_m N_l [\beta_p^{\mathrm{T}}(\mathbf{D}_p F_s) + \beta_n^{\mathrm{T}}(\mathbf{D}_{np} F_s)] F_\tau)\, dA dL \\
&\quad + \int_{L^{(e)}}\int_{A^{(e)}} (T_0 [\beta_n^{\mathrm{T}} N_m (\mathbf{D}_{ny} N_l) F_s F_\tau)\, dA dL \\
[\mathbf{G}_{\Theta\Theta}^{lm\tau s}]_{1\times1} &= \int_{L^{(e)}}\int_{A^{(e)}} (\rho c N_m N_l F_\tau F_s)\, dA dL \\
&\quad - \int_{L^{(e)}}\int_{A^{(e)}} (2\tilde{\mathbf{c}}^{\mathrm{T}} N_m [\nabla_n N_l] F_\tau F_s)\, dA dL \\
&\quad - \int_{L^{(e)}}\int_{A^{(e)}} (2\tilde{\mathbf{c}}^{\mathrm{T}} N_m N_l F_\tau [\nabla_p F_s])\, dA dL
\end{aligned} \tag{4.29}$$

$$
\begin{aligned}
[\mathbf{K}_{UU}^{lm\tau s}]_{3\times3} &= \int_{L^{(e)}}\int_{A^{(e)}} \Big(N_m N_l \left[(\mathbf{D}_{np}^{\mathrm{T}} F_\tau \mathbf{I})[\mathbf{C}_{nn}(\mathbf{D}_{np} F_s \mathbf{I}) + \mathbf{C}_{np}(\mathbf{D}_p F_s \mathbf{I})]\right. \\
&\qquad \left. + \ (\mathbf{D}_p^{\mathrm{T}} F_\tau \mathbf{I})[\mathbf{C}_{pp}(\mathbf{D}_p F_s \mathbf{I}) + \mathbf{C}_{pn}(\mathbf{D}_{np} F_s \mathbf{I})]\right]\Big)\, dA dL \\
&+ \int_{L^{(e)}}\int_{A^{(e)}} \left(N_m(\mathbf{D}_{ny} N_l)[(\mathbf{D}_{np}^{\mathrm{T}} F_\tau \mathbf{I})\mathbf{C}_{nn} + (\mathbf{D}_p^{\mathrm{T}} F_\tau \mathbf{I})\mathbf{C}_{pn}]F_s\right)\, dA dL \\
&+ \int_{L^{(e)}}\int_{A^{(e)}} \left((\mathbf{D}_{ny}^{\mathrm{T}} N_m) N_l F_\tau [\mathbf{C}_{np}(\mathbf{D}_p F_s \mathbf{I}) + \mathbf{C}_{nn}(\mathbf{D}_{np} F_s \mathbf{I})]\right)\, dA dL \\
&+ \int_{L^{(e)}}\int_{A^{(e)}} \left((\mathbf{D}_{ny}^{\mathrm{T}} N_m)(\mathbf{D}_{ny} N_l) F_\tau \mathbf{C}_{nn} F_s\right)\, dA dL \\
[\mathbf{K}_{U\Theta}^{lm\tau s}]_{3\times1} &= -\int_{L^{(e)}}\int_{A^{(e)}} \left(N_m N_l[(\mathbf{D}_p^{\mathrm{T}} F_\tau)\beta_p + (\mathbf{D}_{np}^{\mathrm{T}} F_\tau)\beta_n]F_s\right)\, dA dL \\
&- \int_{L^{(e)}}\int_{A^{(e)}} \left((\mathbf{D}_{ny}^{\mathrm{T}} N_m) N_l F_\tau \beta_n F_s\right)\, dA dL \\
[\mathbf{K}_{\Theta\Theta}^{lm\tau s}]_{1\times1} &= \int_{L^{(e)}}\int_{A^{(e)}} \left(N_m N_l (\nabla_p^{\mathrm{T}} F_s)\kappa(\nabla_p F_\tau)\right)\, dA dL \\
&+ \int_{L^{(e)}}\int_{A^{(e)}} \left((\nabla_n^{\mathrm{T}} N_l)(N_m)\kappa(\nabla_p F_\tau)F_s\right)\, dA dL \\
&+ \int_{L^{(e)}}\int_{A^{(e)}} \left(N_l(\nabla_n N_m)\kappa(\nabla_p^{\mathrm{T}} F_s)F_\tau\right)\, dA dL \\
&+ \int_{L^{(e)}}\int_{A^{(e)}} \left((\nabla_n^{\mathrm{T}} N_l)(\nabla_n N_m) F_\tau \kappa F_s\right)\, dA dL
\end{aligned}
\tag{4.30}
$$

$$
\begin{aligned}
\{\mathbf{F}^{m\tau}\}_{3\times1} &= \int_{L^{(e)}}\int_{A^{(e)}} (\mathbf{X} N_m F_\tau)\, dA dL + \int_{S^{(e)}} (\mathbf{t} N_m F_\tau) dS \\
\{Q^{m\tau}\}_{1\times1} &= \int_{S^{(e)}} (\mathbf{q}^{\mathrm{T}} \mathbf{n} N_m F_\tau) dS + \int_{L^{(e)}}\int_{A^{(e)}} (R N_m F_\tau)\, dA dL \\
&\quad + \int_{L^{(e)}}\int_{A^{(e)}} (t_0 \dot{R} N_m F_\tau)\, dA dL
\end{aligned}
\tag{4.31}
$$

In the expressions (4.28)-(4.31), $\mathbf{I}$ represents the identity matrix. The subscript p denotes the in-plane components over a cross section of the structure, while n indicates the normal components to the cross section. Accordingly, the matrices $\mathbf{D}_p$, $\mathbf{D}_{np}$ and $\mathbf{D}_{ny}$ and the vectors ∇_p and ∇_n can be defined as

$$
\mathbf{D}_p = \begin{bmatrix} 0 & 0 & \partial_z \\ \partial_x & 0 & 0 \\ \partial_z & 0 & \partial_x \end{bmatrix}, \quad \mathbf{D}_{np} = \begin{bmatrix} 0 & 0 & 0 \\ 0 & \partial_z & 0 \\ 0 & \partial_x & 0 \end{bmatrix}, \quad \mathbf{D}_{ny} = \begin{bmatrix} 0 & \partial_y & 0 \\ 0 & 0 & \partial_y \\ \partial_y & 0 & 0 \end{bmatrix} \tag{4.32}
$$

and

$$
\nabla_p = \{\ \partial_x \quad 0 \quad \partial_z\ \}^{\mathrm{T}}\ ,\ \nabla_n = \{\ 0 \quad \partial_y \quad 0\ \}^{\mathrm{T}} \tag{4.33}
$$

Similarly, the grouped elastic coefficients matrix and stress-temperature moduli vector are given as

$$\mathbf{C}_{pp} = \begin{bmatrix} C_{11} & C_{12} & C_{14} \\ C_{21} & C_{22} & C_{24} \\ C_{41} & C_{42} & C_{44} \end{bmatrix} \quad , \quad \mathbf{C}_{nn} = \begin{bmatrix} C_{33} & C_{35} & C_{36} \\ C_{53} & C_{55} & C_{56} \\ C_{63} & C_{65} & C_{66} \end{bmatrix} \quad , \quad \mathbf{C}_{pn} = \begin{bmatrix} C_{13} & C_{15} & C_{16} \\ C_{23} & C_{25} & C_{26} \\ C_{43} & C_{45} & C_{46} \end{bmatrix} \tag{4.34}$$

$$\beta_p = \{\beta_{zz} \;\; \beta_{xx} \;\; \beta_{xz}\}^{\mathrm{T}} \qquad \beta_n = \{\beta_{yy} \;\; \beta_{yz} \;\; \beta_{xy}\}^{\mathrm{T}} \tag{4.35}$$

where $\mathbf{C}_{np} = \mathbf{C}_{pn}^{\mathrm{T}}$. In order to summarize, the expanded expressions for components of the matrix $\mathbf{C}$ for anisotropic materials are not given here, but they can be found in Ref. [56].

Furthermore, in most practical engineering problems, the structural damping matrix $\mathbf{G}_{UU}^{lm\tau s}$ may be computed by the Rayleigh damping model as [24]

$$\mathbf{G}_{UU}^{lm\tau s} = \zeta_1 \mathbf{M}_{UU}^{lm\tau s} + \zeta_2 \mathbf{K}_{UU}^{lm\tau s} \tag{4.36}$$

in which $\zeta_1 \mathbf{M}_{UU}$ and $\zeta_2 \mathbf{K}_{UU}$ are the structural mass and stiffness proportional damping terms, respectively, and the parameters ζ_1 and ζ_2 are typically obtained by experiments for materials.

Therefore the FNs (4.28)-(4.31) must be expanded with respect to the superscripts m, l, τ and s in order to obtain the FE matrices and vectors of the whole structure. In fact, indexes m and l are exploited to assemble the matrices in the FE procedure while τ and s are used to provide the order of the model. The assembly procedure of the FNs are concerned in the companion paper (Part 2). Thus, the matrix form of the governing equation for the whole structure can be expressed as

$$\mathbf{M}\ddot{\Delta} + \mathbf{G}\dot{\Delta} + \mathbf{K}\Delta = \mathbf{P} \tag{4.37}$$

where $\mathbf{M}$, $\mathbf{G}$ and $\mathbf{K}$ are the global mass, damping and stiffness matrices. Likewise, $\mathbf{P}$ is the global vector of the applied mechanical and thermal loads and Δ stands for the global vector of unknowns. Equation (4.37) of the whole structure can be solved for the nodal displacements and temperature change in the time domain by the standard numerical techniques used to such problems in the literature.

It is noted that in the presented formulation, the thermal and mechanical boundary conditions as well as the body forces and the heat sources are considered as the most general forms. The mechanical boundary conditions may be applied through specified traction vectors or displacements on the boundaries. likewise, the differ-

ent types of thermal boundary conditions including a known temperature change on a part of the boundary surface, a known heat flux on the boundary and the convection and radiation conditions may be assumed in problems. It is further obvious that the concentrated thermal and mechanical loads can be taken into account as the particular cases of the surface loads. Moreover, the initial thermal and mechanical conditions may be assumed in general form as arbitrary known functions of the space coordinates.

In the unified FE formulation (4.27), indeed, addition to taking into account the mechanical damping effect by the matrix $\mathbf{G}_{UU}^{lm\tau s}$, six theories of GL, LS, classical, dynamic uncoupled, quasi-static uncoupled and static uncoupled thermoelasticity are included. Accordingly, the generalized theory of thermoelasticity based on the Green-Lindsay and Lord-Shulman can be involved for $t_0 = 0$ and $t_1 = t_2 = \tilde{\mathbf{c}} = 0$, respectively. The four other theories can be provided as particular cases as represented in Table 4.1. Equation (4.27) can be simplified to the formulation of the classical coupled thermoelasticity problems by taking $t_1 = t_2 = \tilde{\mathbf{c}} = 0$ and $t_0 = 0$. The classical coupled theory reduces to the *dynamic uncoupled thermaoelasticity* by eliminating the coupling matrix ($\mathbf{G}_{\Theta U}^{lm\tau s}$) from the formulation. The dynamic uncoupled formulation can be employed for the problems in which the rate of imposed thermo-mechanical loads is not rapid enough to generate thermal stress waves. If the inertia forces can be further neglected as $\mathbf{M}_{UU}^{lm\tau s} = 0$, the governing formulation for the *quasi-static uncoupled thermaoelasticity* problems is obtained. Moreover, in a steady-state condition ($\mathbf{G}_{\Theta\Theta}^{lm\tau s} = 0$), the formulation can be more simplified to *static uncoupled thermoelasticity* where thermal stresses are imposed by the deformations due to the steady-state temperature field.

Table 4.1 Different theories of thermoelasticity through the 1D FE-CUF

	Conditions		Theory
Dynamic Coupled	$t_0 = 0$		Generalized, GL
	$t_1 = t_2 = \tilde{\mathbf{c}} = 0$		Generalized, LS
	$t_0 = 0$ $t_1 = t_2 = \tilde{\mathbf{c}} = 0$		Classical
Uncoupled	$t_0 = 0$ $t_1 = t_2 = \tilde{\mathbf{c}} = 0$	$\mathbf{G}_{\Theta U}^{lm\tau s} = 0$	dynamic
		$\mathbf{M}_{UU}^{lm\tau s} = 0$ $\mathbf{G}_{\Theta U}^{lm\tau s} = 0$	quasi-static
		$\mathbf{M}_{UU}^{lm\tau s} = 0$ $\mathbf{G}_{\Theta U}^{lm\tau s} = 0$ $\mathbf{G}_{\Theta\Theta}^{lm\tau s} = 0$	static

4.5 Component-wise approach for the coupled thermoelastic problems

In this dissertation, the approximating expansions have been obtained using bi-dimensional Lagrange functions. The Lagrange-based elements enable the physical surfaces to be modeled adopting arbitrary kinematics. This inherent capability makes it possible to create component-wise (CW) mathematical models, which can accurately describe the geometry of the real structure. Within the CW context, cross sections can be discretized by using different types of Lagrange elements (LEs) such as linear three-point (denoted as L3), bi-linear 4-point (L4), bi-quadratic 9-point (L9), and bi-cubic 16-point (L16) elements (see Fig. 3.4).
As far as the longitudinal discretization is concerned, beam elements with 2, 3 or 4 nodes can be chosen (Fig. 3.3). Figure 4.4 shows a possible mathematical model used to discretize a simple 3D geometry.

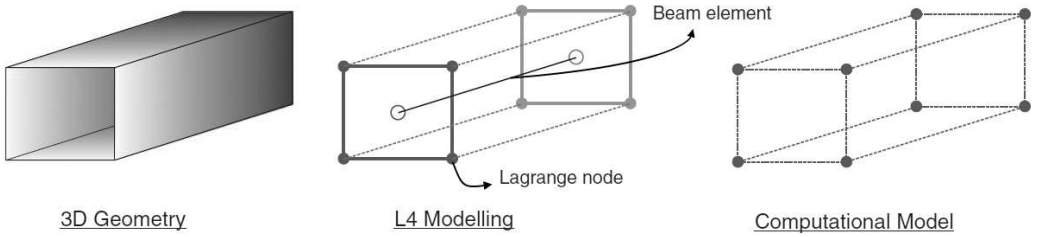

Fig. 4.4 32 DOF total, 16 DOF per beam node, 4 DOF per Lagrange node.

The model shown in Fig. 4.4 consists of 8 Lagrange points (4 per each beam node), and 32 degrees of freedom (DOF) (4 DOF per each Lagrangian point). Thus, the corresponding displacement field and the temperature change are

$$\begin{aligned}
u_x &= N_m F_\tau U_x^{m\tau} = N_1(F_1 U_x^{11} + \cdots + F_4 U_x^{14}) + N_2(F_1 U_x^{21} + \cdots + F_4 U_x^{24}) \\
u_y &= N_m F_\tau U_y^{m\tau} = N_1(F_1 U_y^{11} + \cdots + F_9 U_y^{14}) + N_2(F_1 U_y^{21} + \cdots + F_4 U_y^{24}) \\
u_z &= N_m F_\tau U_z^{m\tau} = N_1(F_1 U_z^{11} + \cdots + F_9 U_z^{14}) + N_2(F_1 U_z^{21} + \cdots + F_4 U_z^{24}) \\
T &= N_m F_\tau \Theta^{m\tau} = N_1(F_1 \Theta^{11} + \cdots + F_9 \Theta^{14}) + N_2(F_1 \Theta^{21} + \cdots + F_4 \Theta^{24})
\end{aligned} \tag{4.38}$$

For the assembly procedure, Fig. 4.5 graphically shows the methodology followed to build the CUF matrices. It should be observed that, in this example, the structure has been modeled using two L4 elements above the cross-section, and three 4-node beam elements along the longitudinal axis.
The total number of DOF of the computational model can be easily computed as

$$\text{DOF} = \sum_{i=1}^{N_{SN}} (4 \times N_{LN}^i) \tag{4.39}$$

where LN^i and SN represent the number of Lagrangian points of the i-th beam node and the total number of structural nodes, respectively. According to the example of Fig. 4.5, Eq. 4.39 reduces to

$$\text{DOF} = \sum_{i=1}^{10} (4 \times 6) = 240 \tag{4.40}$$

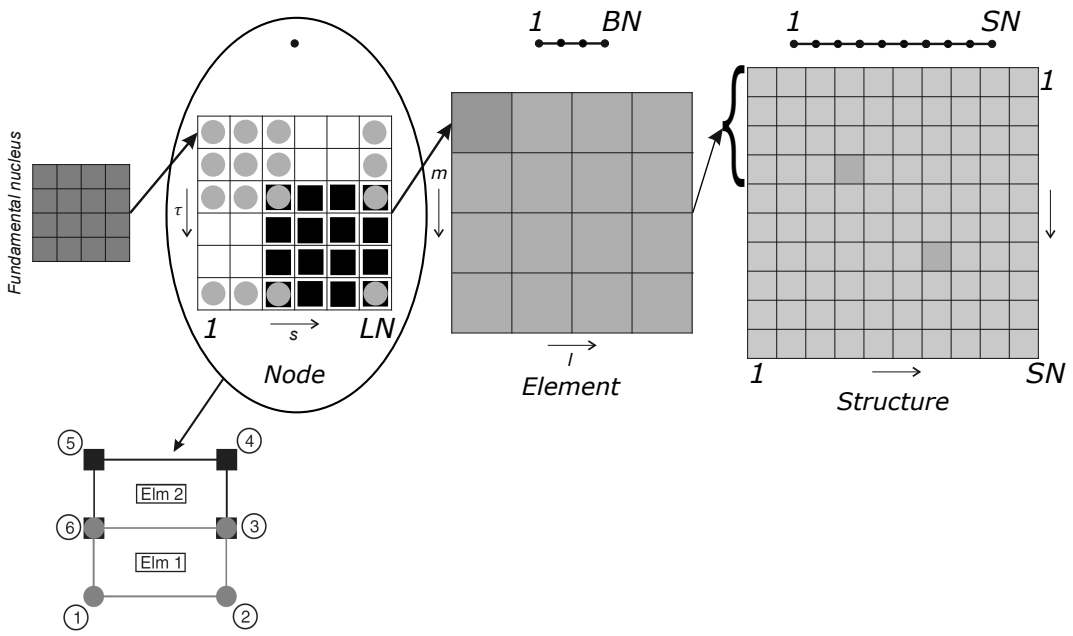

Fig. 4.5 Graphical representation of the assembly procedure.

4.6 Time history analysis

The transfinite element technique through the Laplace transform can be effectively used to find the time history responses of the dynamic coupled thermoelasticity equations in very short time intervals. In this method, the problems are solved in the Laplace transform domain by the FE method and then the transformed solutions are numerically inverted to obtain the physical responses in the time domain. Thus, taking Laplace transform of Eq. (4.26) results in

$$\mathbf{K}_{eq}{}^{lm\tau s}(\tilde{s})\delta^{m\tau^*} = \mathrm{p}^{ls^*}(\tilde{s}) \tag{4.41}$$

where $\mathrm{K}_{eq}^{lm\tau s}$ is the FN of the equivalent stiffness matrix that includes inertial, stiffness and damping contributions and is obtained as

$$\mathbf{K}_{eq}{}^{lm\tau s}(\tilde{s}) = \mathbf{M}^{lm\tau s}\tilde{s}^2 + \mathbf{G}^{lm\tau s}\tilde{s} + \mathbf{K}^{lm\tau s} \tag{4.42}$$

Here, $\tilde{s}$ stands for the Laplace variable and the superscript asterisk denotes Laplace transform of the terms.

The linear system of Eq. (4.41) is solved for different values of $\tilde{s}$, and then the

solutions are obtained in the time domain using the numerical inversion of Laplace transforms proposed by [28].

4.7 Non-dimensional FNs

It is expedient to express the governing equations in a nondimensional form. To this end, the following parameters are introduced

$$\begin{aligned}
&\hat{x}_i = x_i/l \ ; \ \ \hat{t} = V_e t/l \ \ ; \\
&\hat{T} = T/T_d \ ; \ \ \hat{u}_i = (\lambda+2\mu)u_i/(l\beta T_d) \ ; \ \hat{t}_0 = V_e t_0/l \\
&\hat{q}_i = q_i/(cT_d\rho V_e) \ \ ; \ \ \hat{\sigma}_{ij} = \sigma_{ij}/(\beta T_d) \ ; \\
&\hat{X}_i = X_i/(T_d\beta) \ \ ; \ \ \hat{R} = DR/(cT_d(\lambda+2\mu))
\end{aligned} \tag{4.43}$$

where the hat values indicate nondimensional parameters. T_d is a characteristic temperature. Moreover $V_e = \sqrt{(\lambda+2\mu)/\rho}$, $l = \kappa/V_e c\rho$ and $D = \kappa/c\rho$ are, respectively, the velocity of elastic longitudinal wave propagation, the dimensionless unit length and the thermal diffusivity of material.
Using the nondimensional parameters and considering the Lord-Shulman generalized theory of coupled thermoelasticity, the explicit nondimensional expressions of the equivalent fundamental nucleus components ($\hat{\mathrm{K}}_{eq}^{lm\tau s}$) in Eq. (4.41) for homogeneous isotropic materials are written as it follows

$$\begin{aligned}
K_{11}^{\tau slm} &= \tilde{s}^2 \lhd F_\tau F_s \rhd I_L^{ml} + \lhd F_{\tau,x} F_{s,x} \rhd I_L^{ml} + \\
&\quad + \hat{C}_{66} \lhd F_\tau F_s \rhd I_L^{m,yl,y} + \hat{C}_{44} \lhd F_{\tau,z} F_{s,z} \rhd I_L^{ml} \\
K_{12}^{\tau slm} &= \hat{C}_{66} \lhd F_\tau F_{s,x} \rhd I_L^{m,yl} + \lhd F_{\tau,x} F_s \rhd I_L^{ml,y} \\
K_{13}^{\tau slm} &= \hat{C}_{44} \lhd F_{\tau,z} F_{s,x} \rhd I_L^{ml} + \hat{C}_{21} \lhd F_{\tau,x} F_{s,z} \rhd I_L^{ml} \\
K_{14}^{\tau slm} &= - \lhd F_{\tau,x} F_s \rhd I_L^{ml}
\end{aligned} \tag{4.44}$$

$$\begin{aligned}
K_{21}^{\tau slm} &= \hat{C}_{66} \lhd F_{\tau,x} F_s \rhd I_L^{ml,y} + \hat{C}_{32} \lhd F_\tau F_{s,x} \rhd I_L^{m,yl} \\
K_{22}^{\tau slm} &= \tilde{s}^2 \lhd F_\tau F_s \rhd I_L^{ml} + \hat{C}_{66} \lhd F_{\tau,x} F_{s,x} \rhd I_L^{ml} + \\
&\quad + \lhd F_\tau F_s \rhd I_L^{m,yl,y} + \hat{C}_{55} \lhd F_{\tau,z} F_{s,z} \rhd I_L^{ml} \\
K_{23}^{\tau slm} &= \hat{C}_{55} \lhd F_{\tau,z} F_s \rhd I_L^{ml,y} + \hat{C}_{31} \lhd F_\tau F_{s,z} \rhd I_L^{m,yl} \\
K_{24}^{\tau slm} &= - \lhd F_\tau F_s \rhd I_L^{m,yl}
\end{aligned} \tag{4.45}$$

$$
\begin{aligned}
K_{31}^{\tau slm} &= \hat{C}_{44} \lhd F_{\tau,x} F_{s,z} \rhd I_L^{ml} + \hat{C}_{12} \lhd F_{\tau,z} F_{s,x} \rhd I_L^{ml} \\
K_{32}^{\tau slm} &= \hat{C}_{55} \lhd F_{\tau} F_{s,z} \rhd I_L^{m,yl} + \hat{C}_{13} \lhd F_{\tau,z} F_{s} \rhd I_L^{ml,y} \\
K_{33}^{\tau slm} &= \tilde{s}^2 \lhd F_{\tau} F_{s} \rhd I_L^{ml} + \hat{C}_{44} \lhd F_{\tau,x} F_{s,x} \rhd I_L^{ml} + \\
&\quad + \hat{C}_{55} \lhd F_{\tau} F_{s} \rhd I_L^{m,yl,y} + \lhd F_{\tau,z} F_{s,z} \rhd I_L^{ml} \\
K_{34}^{\tau slm} &= - \lhd F_{\tau,z} F_{s} \rhd I_L^{ml}
\end{aligned}
\tag{4.46}
$$

$$
\begin{aligned}
K_{41}^{\tau slm} &= C(\tilde{s}^2 \hat{t}_0 + \tilde{s}) \lhd F_{\tau} F_{s,x} \rhd I_L^{ml} \\
K_{42}^{\tau slm} &= C(\tilde{s}^2 \hat{t}_0 + \tilde{s}) \lhd F_{\tau} F_{s} \rhd I_L^{ml,y} \\
K_{43}^{\tau slm} &= C(\tilde{s}^2 \hat{t}_0 + \tilde{s}) \lhd F_{\tau} F_{s,z} \rhd I_L^{ml} \\
K_{44}^{\tau slm} &= (\tilde{s}^2 \hat{t}_0 + \tilde{s}) \lhd F_{\tau} F_{s} \rhd I_L^{ml} + \\
&\quad + \lhd F_{\tau,x} F_{s,x} \rhd I_L^{ml} + \lhd F_{\tau} F_{s} \rhd I_L^{m,yl,y} + \lhd F_{\tau,z} F_{s,z} \rhd I_L^{ml}
\end{aligned}
\tag{4.47}
$$

where

$$
I_L^{ml} \,|\, I_L^{m,yl} \,|\, I_L^{ml,y} \,|\, I_L^{m,yl,y} = \int_{L^{(e)}} \left(N_m N_l \,|\, N_{m,y} N_l \,|\, N_m N_{l,y} \,|\, N_{m,y} N_{l,y} \right) dy
$$

$$
\lhd \cdots \rhd = \int_{A^{(e)}} (\cdots) dA
$$

Furthermore, $C = T_0 \beta^2 / [c\rho(\lambda + 2\mu)]$ is the thermoelastic coupling (or damping) parameter. The dimensionless elastic coefficients $\hat{C}_{ij}$ are

$$
\begin{aligned}
\hat{C}_{44} = \hat{C}_{55} = \hat{C}_{66} &= \frac{\mu}{(\lambda + 2\mu)} \\
\hat{C}_{12} = \hat{C}_{13} = \hat{C}_{23} &= \frac{\lambda}{(\lambda + 2\mu)}
\end{aligned}
$$

Likewise, by considering surface and volume forces, the general nondimensional expression of the loading vector in the Laplace domain becomes

$$
\begin{aligned}
p_1^{m\tau^*} &= \int\limits_{S^{(e)}} \hat{t}_x^{n^*} F_{\tau} N_m dS + \int\limits_{V^{(e)}} \hat{X}_x^* F_{\tau} N_m dV \\
p_2^{m\tau^*} &= \int\limits_{S^{(e)}} \hat{t}_y^{n^*} F_{\tau} N_m dS + \int\limits_{V^{(e)}} \hat{X}_y^* F_{\tau} N_m dV \\
p_3^{m\tau^*} &= \int\limits_{S^{(e)}} \hat{t}_z^{n^*} F_{\tau} N_m dS + \int\limits_{V^{(e)}} \hat{X}_z^* F_{\tau} N_m dV \\
p_4^{m\tau^*} &= \int\limits_{V^{(e)}} [(\hat{t}_0 \tilde{s} + 1) \hat{R}^*] F_{\tau} N_m dV + \int\limits_{S^{(e)}} (\hat{q}_i^* n_i) F_{\tau} N_m dS
\end{aligned}
\tag{4.48}
$$

Here, the superscript asterisk denotes Laplace transform of the terms. $\hat{t}_i^n$ and $\hat{q}_i$ are the dimensionless traction and heat flux vectors, respectively. n_i is the unit vector normal to the boundary surface of the element $S^{(e)}$.

4.8 Summary

In the framework of the the Carrera unified formulation, the 1D FE procedure is developed to the 3D solution of the static, transient, and dynamic problems in the coupled and uncoupled thermoelasticity for the nonhomogeneous anisotropic materials. As particular cases, the generalized theories based on the Lord-Shulman and the Green-Lindsay models, as well as the classical coupled, dynamic uncoupled, quasi-static uncoupled and steady-state uncoupled theories of thermoelasticity can be extracted from the presented formulation. The mechanical damping effect can be further taken into account in the problems. In addition, the thermal and mechanical boundary conditions, the body force and the heat source are considered in the most general forms where no limiting assumption is applied. This generality allows to analyze varieties of more practical thermoelastic problems. Since this approach reduces the 3D problems to the 1D models with 3D-like accuracies and very low computational costs, it may seem to be a competent tool in an iterative solution process of the dynamic coupled thermoelasticity problems.

Chapter 5

Coupled thermoelastic analysis: Numerical evaluations and results

This chapter aims to evaluate the high-fidelity 1D FE-CUF approach proposed in the chapter 4. To this end, first, the approach is evaluated for a simple metallic beam problem and then is employed for the coupled thermoelastic analysis of disks. Static, quasi-static, and dynamic analyses of the coupled and uncoupled thermoelasticity have been performed in this chapter.

5.1 Thermoelastic analysis of a beam

Firstly, a static coupled thermoelastic analysis is performed on a simple metallic cantilever beam. The related results, which have obtained with different mathematical models, have been compared with a solution computed with a simple one-dimensional analytical formula. Secondly, the same configuration has been considered for a transient quasi-static analysis.

5.1.1 Static uncoupled thermoelastic analysis of a beam

The structure is a cantilever square beam, which has been subjected to a heat flux (q=100 W) at the clamped edge. The free tip has been considered at ambient temperature (T_0=20^o C). The cross-section area and the beam length were A = 20 cm^2,

and L = 50 cm, respectively. The material is aluminum with the Young's modulus E=73.1 GPa, the Poisson's ratio ν= 0.33, the thermal conductivity κ = 237 W·(m·K)$^{-1}$ and the coefficient of thermal expansion α=23.1$\times$10^{-6} K^{-1}. The analyses have been performed using several mathematical models. In particular, Table 5.1 lists the temperature changes and the longitudinal displacements along the beam axis using the 2-node finite elements. Further mesh studies have been performed considering the 4-node beam elements and different kinematic theories obtained with the L4, L9 and L16 Lagrange elements. The results are reported in Tables. 5.2, 5.3 and 5.4, respectively.

Table 5.1 Displacement and temperature change vs. number of B2 elements, 1L4.

		Location along the y-axis in mm (y_i)					
Nr. elements		0.0	0.1	0.2	0.3	0.4	0.5
5-B2	u_y	0.0	0.319	0.473	0.597	0.670	0.696
	T	105.5	84.38	63.28	42.19	21.09	0.0
10-B2	u_y	0.0	0.263	0.435	0.556	0.629	0.654
	T	105.5	84.38	63.28	42.19	21.09	0.0
20-B2	u_y	0.0	0.245	0.416	0.537	0.611	0.635
	T	105.5	84.38	63.28	42.19	21.09	0.0
30-B2	u_y	0.0	0.240	0.410	0.532	0.605	0.630
	T	105.5	84.38	63.28	42.19	21.09	0.0
50-B2	u_y	0.0	0.236	0.407	0.529	0.602	0.626
	T	105.5	84.38	63.28	42.19	21.09	0.0
100-B2	u_y	0.0	0.235	0.406	0.527	0.601	0.625
	T	105.5	84.38	63.28	42.19	21.09	0.0

Table 5.2 Displacement and temperature change vs. number of B4 elements, 1L4.

		Location along the y-axis in mm (y_i)					
Nr. elements		0.0	0.1	0.2	0.3	0.4	0.5
5-B4	u_y	0.0	0.242	0.412	0.534	0.607	0.631
	T	105.5	84.38	63.28	42.19	21.09	0.0
10-B4	u_y	0.0	0.236	0.406	0.528	0.601	0.625
	T	105.5	84.38	63.28	42.19	21.09	0.0
20-B4	u_y	0.0	0.234	0.405	0.527	0.600	0.624
	T	105.5	84.38	63.28	42.19	21.09	0.0
30-B4	u_y	0.0	0.234	0.405	0.527	0.600	0.624
	T	105.5	84.38	63.28	42.19	21.09	0.0
50-B4	u_y	0.0	0.234	0.405	0.527	0.600	0.624
	T	105.5	84.38	63.28	42.19	21.09	0.0
100-B4	u_y	0.0	0.234	0.405	0.527	0.600	0.624
	T	105.5	84.38	63.28	42.19	21.09	0.0

Table 5.3 Displacement and temperature change vs. number of B4 elements, 1L9.

		Location along the y-axis in mm (y_i)					
Nr. elements		0.0	0.1	0.2	0.3	0.4	0.5
5-B4	u_y	0.0	0.242	0.409	0.531	0.604	0.629
	T	105.5	84.38	63.28	42.19	21.09	0.0
10-B4	u_y	0.0	0.233	0.404	0.526	0.601	0.623
	T	105.5	84.38	63.28	42.19	21.09	0.0
20-B4	u_y	0.0	0.232	0.403	0.525	0.599	0.622
	T	105.5	84.38	63.28	42.19	21.09	0.0
30-B4	u_y	0.0	0.232	0.403	0.525	0.598	0.622
	T	105.5	84.38	63.28	42.19	21.09	0.0
50-B4	u_y	0.0	0.232	0.403	0.525	0.598	0.622
	T	105.5	84.38	63.28	42.19	21.09	0.0
100-B4	u_y	0.0	0.232	0.403	0.525	0.598	0.622
	T	105.5	84.38	63.28	42.19	21.09	0.0

Table 5.4 Displacement and temperature change vs. number of B4 elements, 1L16.

		Location along the y-axis in mm (y_i)					
Nr. elements		0.0	0.1	0.2	0.3	0.4	0.5
5-B4	u_y	0.0	0.242	0.409	0.531	0.604	0.629
	T	105.5	84.38	63.28	42.19	21.09	0.0
10-B4	u_y	0.0	0.233	0.404	0.526	0.598	0.623
	T	105.5	84.38	63.28	42.19	21.09	0.0
20-B4	u_y	0.0	0.231	0.402	0.524	0.597	0.621
	T	105.5	84.38	63.28	42.19	21.09	0.0
100-B4	u_y	0.0	0.231	0.402	0.524	0.597	0.621
	T	105.5	84.38	63.28	42.19	21.09	0.0

It is observed that the predicted temperature changes (T= 105.5 ^{o}C) satisfies the conduction equation

$$q = \kappa A \frac{T}{L} = 100 \text{ W} \tag{5.1}$$

For the axial elongations, the CUF results can be compared with a simple one-dimensional relation

$$u_y(y_i) = y_i \, \alpha \, \frac{(T_{y_i} + T_{y_i=0})}{2} \tag{5.2}$$

where y_i is the axial location. The results revealed that the proposed beam elements ensure a significant rate of convergence. In fact, only 5 elements are enough to predict the correct values of temperature changes, while models with 10 elements provide converged solutions also for the displacements, regardless of which Lagrange elements are used.

5.1.2 Quasi-static uncoupled thermoelastic analysis

The quasi-static response of the previous structure has been analysed. The governing equations have been modified such that the inertial terms, as well as the time variations of strains into the energy equation, are disregarded. The mathematical model used to perform the transient analysis consisted of 10 B4 finite elements along the beam axis and 1 L4 element above the cross-section. The time history of the temperature changes and the longitudinal displacements at different locations along the beam axis are shown in Figs. 5.1.

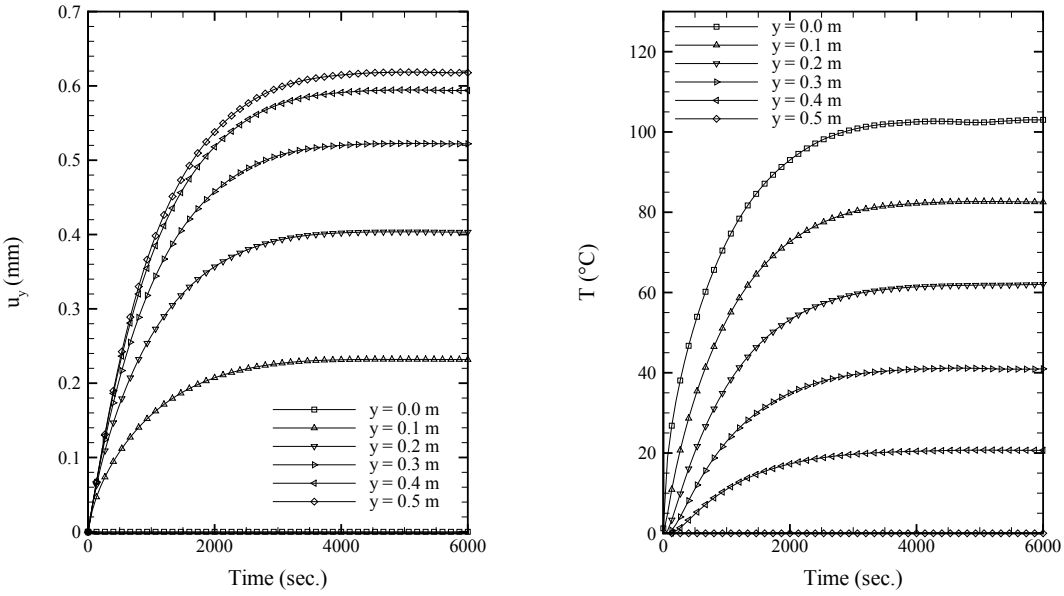

Fig. 5.1 Time histories of axial displacements and temperature changes as functions of the location. 10B4/1L4 model.

The figures show that, as the time passes (time $\rightarrow \infty$), the steady state values of the temperature changes and the axial displacements are reached (see Table 5.2). In the case in point, the steady-state solutions are obtained after about 2000 seconds. Figures 5.2 and 5.3 show the axial displacements and the temperature fields at different times.

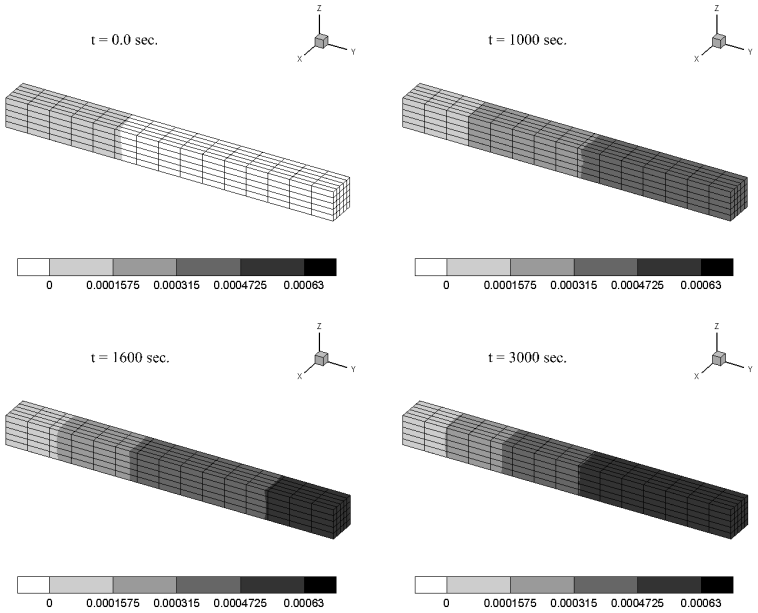

Fig. 5.2 Axial displacements (in meters) at different times. 10B4/1L4 model.

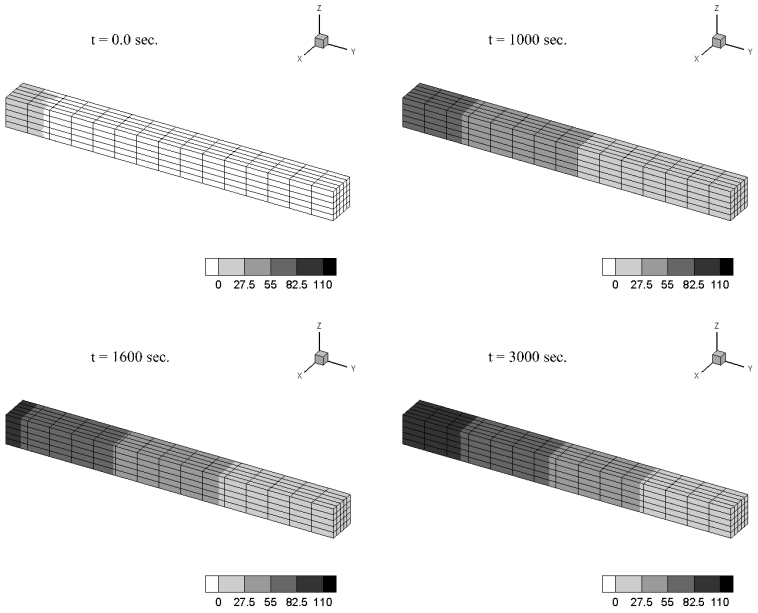

Fig. 5.3 Temperature changes (^{o}C) at different times. 10B4/1L4 model.

5.2 Dynamic coupled thermoelastic analysis of a disk

Based on the LS theory of thermoelasticity, the non-dimensional finite element equations are solved and evaluated for an axisymmetric and asymmetric disk made of homogeneous isotropic materials.

5.2.1 Axisymmetric disk

To evaluate and validate the present method, a numerical example is selected from reference [4] in which a 1D FE method has been used to solve the coupled thermoelasticity problem in a disk. Furthermore, this example has been analytically solved in the chapter 2. It is noted that the solution in both references obtained under axisymmetric and plane stress assumptions. Therefore, to unify the nondimensional parameters and compare the obtained results with the reference solutions, λ and β in the relations (4.43) must be respectively replaced by $k\lambda$ and $k\beta$ where $k = 2\mu/(\lambda + 2\mu)$.
Thus, an annular disk with constant thickness made of aluminum with $\lambda = 40.4$ GPa, $\mu = 27$ GPa, ρ=2707 kg/m^3, α=23×10^{-6} K^{-1}, κ=204 W/m$\cdot$K, c=903 J/kg$\cdot$K is considered. The dimensionless inner and outer radii of the disk are equal to $a = 1$ and $b = 2$, respectively, while the the dimensionless value 0.1 is considered to be the thickness of the disk. As the mechanical boundary conditions, the surface at inner radius is rigidly fixed while the other surfaces are assumed to be stress free. The temperature change on the outer surface is equal to zero, while the surface at inner radius is suddenly exposed to a heat flux as the Heaviside unit step function. Two side surfaces of the disk are assumed to be thermally insulated as well.
In the 1D FE-CUF approach, the disk can be assumed as a beam along its axis so that each cross section of the beam is defined in any plane perpendicular to the axis. Accordingly, to study the convergence of the results and the effect of discretization quality and type of the elements on the accuracy of the method, 6 models of 1D FE-CUF are considered in accordance with Table 5.5. Also, Figs. 5.4 and 5.5 show the types of discretizations considered along the axis and over the cross section of the disk.

Table 5.5 Different 1D FE-CUF models for the constant thickness disk

Model	Discretizing		DOF*
	along axis	over cross section	
(1)	1 B2		1680
(2)	1 B3	(6×30) L4	2520
(3)	1 B4		3360
(4)	1 B2	(3×15) L9	1680
(5)		(2×10) L16	
(6)		(6×18) L9	3744

*DOF: total degrees of freedom

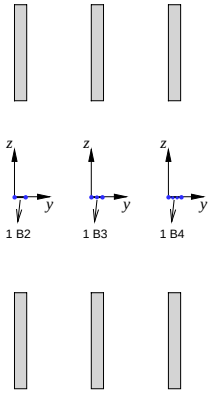

(a) (b) (c)

Fig. 5.4 Discretizing along the axis of the disk.

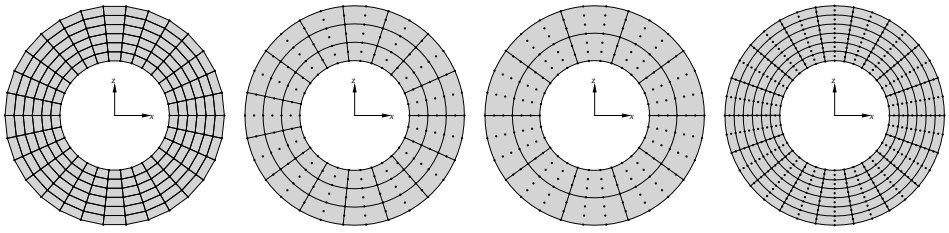

(6×30) L4 (3×15) L9 (2×10) L16 (6×18) L9

Fig. 5.5 Discretizing and distribution of Lagrange elements over the cross section of the disk.

Based on the classical theory of thermoelasticity and assuming the numerical value of the coupling parameter to be 0.02, the time history of the radial displacement and the temperature change in the mid-radius of the disk are shown in Figs. 5.6-5.8 and compared with the analytical solutions reported in the chapter 2.
Considering the distribution of (6×30) L4 on the cross-section of the disk, Fig. 5.6 shows these time history for the different types of beam elements along the axis. It is observed that since the disk is thin, the use of higher order elements B3 and B4 in comparison with the linear element B2 not only does not affect the accuracy of the results, but also significantly increases the degrees of freedom (DOF) and consequently the computational costs. Therefore, one B2 element along the axial direction can be enough to obtain converge solution with this model. Further improvement in the accuracy of the solution may be achieved by a refinement of the discretization over the cross sections.

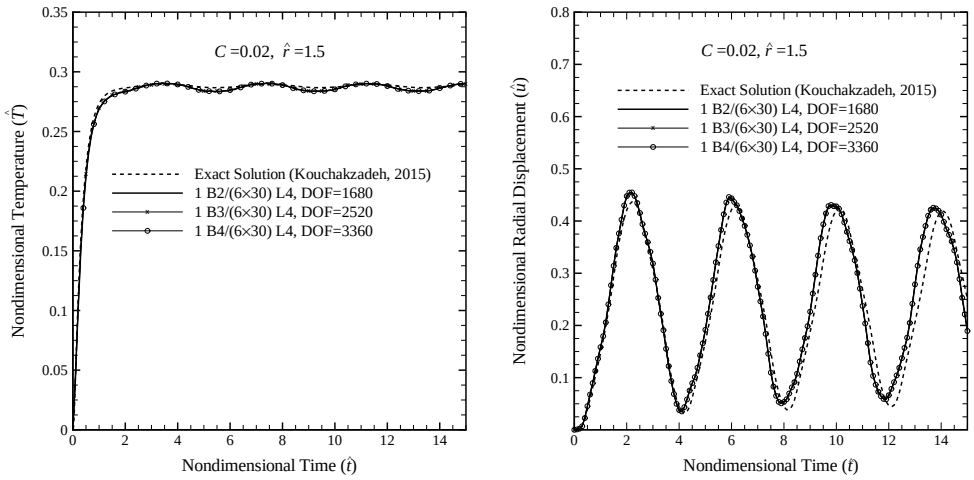

Fig. 5.6 Time histories of the nondimensional temperature change (a), and radial displacement (b) at mid-radius of the disk.

Thus, considering 1 B2 element along the axis, the effects of the Lagrangian element type on the accuracy of the time histories obtained at the mid-radius of the models with same DOF are shown in Fig. 5.7. As observed, using L9 and L16 elements, instead of L4, the accuracy of the solution arises. The reason is that the L9 and L16 elements respectively use fourth- and ninth-order polynomials as interpolation functions, while L4 is a bilinear element with second-order polynomials.

In this case, increasing the number of L4 elements over cross sections may increase the accuracy. Also, it is seen from Fig. 5.7 that, for the models with the same DOF, the use of L9 and L16 elements over cross sections of the model gives approximately the same results. In addition, although there is still little difference between the obtained solution and the reference result, the effect of the higher-order elements on the accuracy of the displacement field is more obvious than the temperature field.

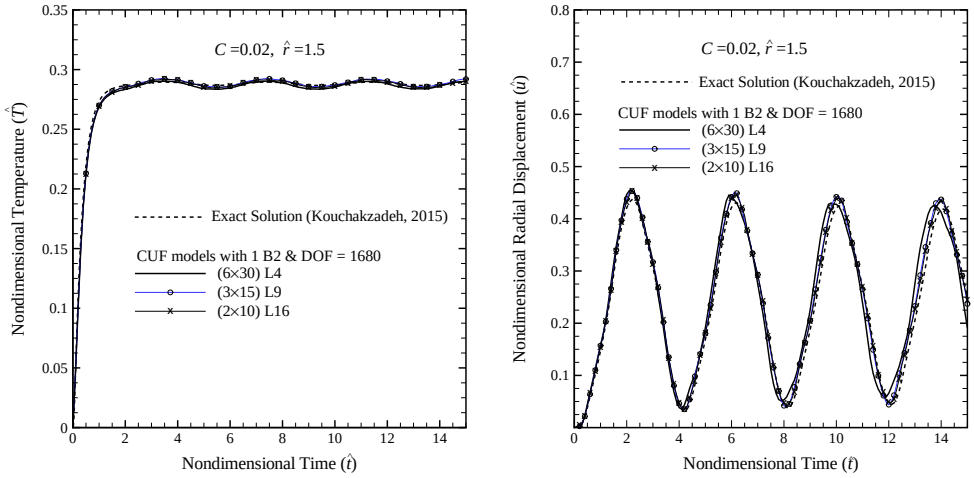

(a) (b)

Fig. 5.7 Time history of the nondimensional temperature change (a) and radial displacement (b) at mid-radius of the disk.

Moreover, refining the distribution of L9 elements over the cross section of the disk with 1 B2 along its axis, may improve the accuracy of the solution. In Fig. 5.8, the results obtained by two different distributions of L9 elements are compared with the reference solution. As seen from this figure, there are some minor differences, at the peaks of oscillations, between the result obtained by the distribution (3×15) L9 and the analytical solution for the radial displacement. By utilizing an improved distribution such as the (6×18) L9, the difference is largely eliminated, and an excellent match appears between the obtained result and the reference solution.

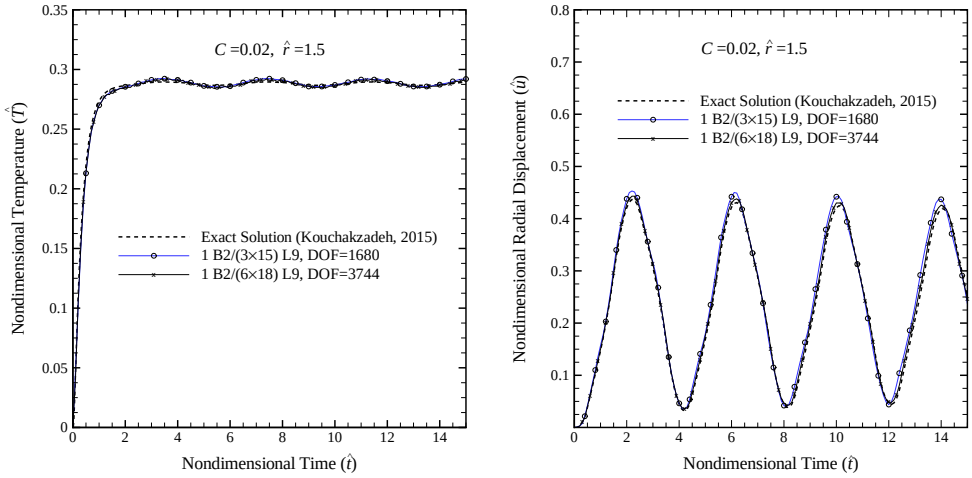

(a) (b)

Fig. 5.8 Time history of the nondimensional temperature change (a) and radial displacement (b) at mid-radius of the disk.

Likewise, the accuracy of the model 1 B2/(6×18) L9 of the disk can be evaluated for solving the generalized coupled thermoelasticity problem based on Lord-Shulman (LS) theory. In this case, the values of the coupling parameter and the relaxation time are assumed to be 0.02 and 0.64, respectively. In Fig. 5.9, the time histories of temperature and radial displacement at mid-radius of the disk for this model are shown and compared with the reference solutions. Moreover, the time histories of radial stress and tangential stress are plotted in Fig. 5.10. These figures reveal that the 1D FE-CUF model is able to provide the reference analytical solutions. However, slight differences between the axisymmetric FE solution proposed by [4] and the other results are observed in Fig. 5.9.

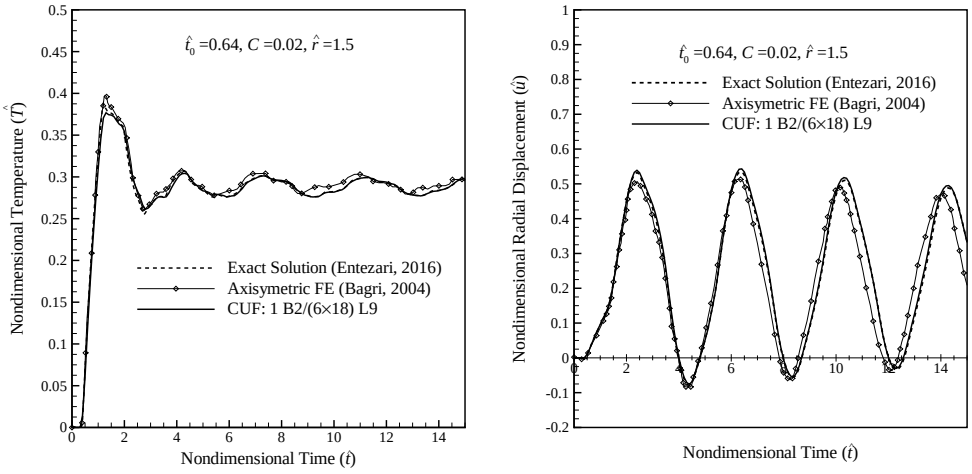

(a) (b)

Fig. 5.9 Time history of the nondimensional temperature change (a) and radial displacement (b) at mid-radius of the disk.

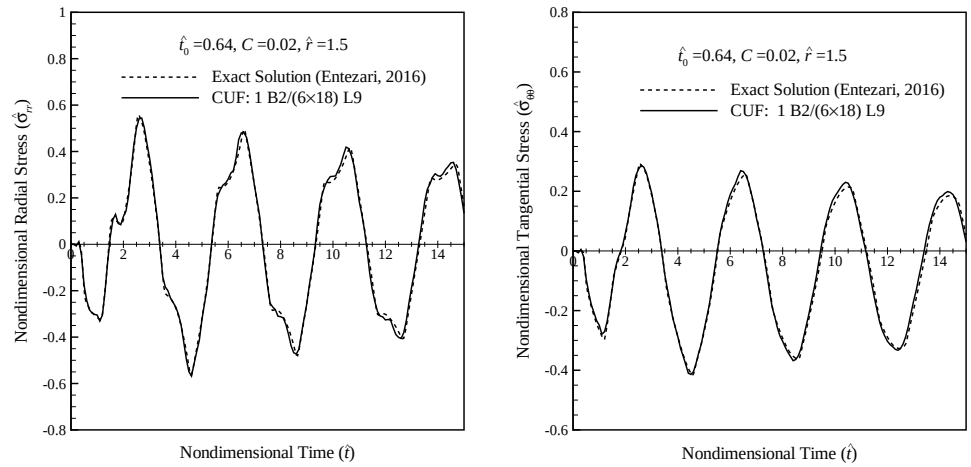

(a) (b)

Fig. 5.10 Time history of the nondimensional radial change and circumferential stresses at mid-radius of the disk.

It may be useful to visualize variations of field variables, like temperature and displacement, over a computational model as contour plots. Thus, recalling capability of the 1D FE-CUF models to provide 3D-like solutions, the obtained results can be shown as 2D or 3D contour plots by an appropriate postprocessing. Based on

the LS thermoelasticity theory, Figs 5.11-5.13 show the contour plots related to distribution of the temperature change and radial displacement on the computational model of the disk at different times. The propagation of the thermal and elastic waves along the time is clearly observed from these figures. Since the geometry and the boundary conditions of the disk are axisymmetric, the temperature change and radial displacement waves propagate in circular form along the radial direction. The velocity of the thermal wave propagation can be evaluated using the contour plots shown in Fig. 5.11. For instance, at the time $\hat{t} = 0.4$, the dimensionless value of the temperature change at the inner radius is about 0.4, while this value becomes zero from the radial position $\hat{r} = 1.5$ toward the outer surface. That is, the temperature wave front at the dimensionless time $\hat{t} = 0.4$ is at the radial position $\hat{r} = 1.5$. Accordingly, the velocity of temperature wave propagation is 1.25. This value can also be computed expectedly from Eq. (**??**) through the square root of the inverse of nondimensional relaxation time. It can be, therefore, said that the plots related to times $\hat{t} = 0.2, 0.4, 0.6$ and 0.8, in Fig. 5.11, show the radial propagation of the thermal wave, while those related to times $\hat{t} = 1$ and 1.2 represent the wave reflection from the outer surface of the disk.

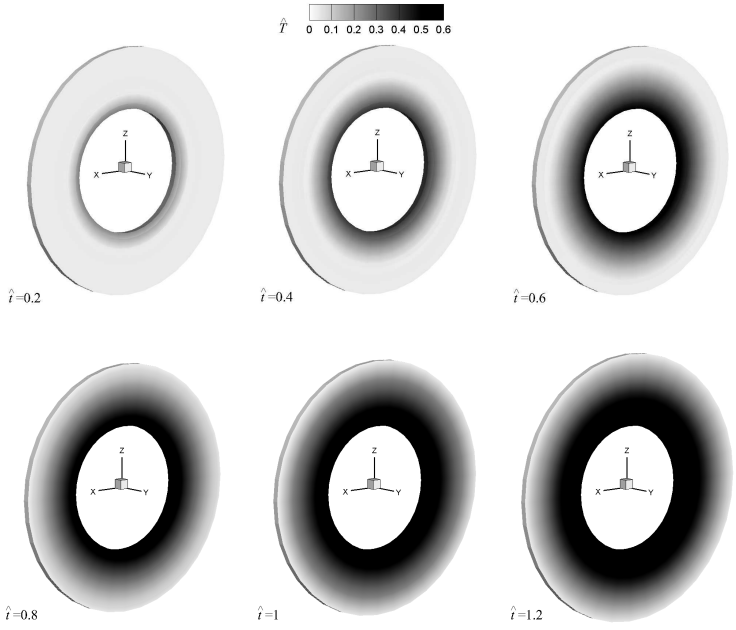

Fig. 5.11 Distribution of nondimensional temperature change for different values of the time.

Figures 5.12 and 5.13 show the distribution of nondimensional radial displacement on *yz* plane of the deformed model at several different times. According to Eq. (**??**), longitudinal elastic waves propagate at unit velocity. Hence, the nondimensional time at which the elastic wave front reaches any nondimensional radial position ($\hat{r}$) for the first time can be calculated using relation $\hat{t} = \hat{r} - a$. For instance, at the time $\hat{t} = 0.4$, the elastic wave front is at the radial position $\hat{r} = 1.4$. This occurrence can also be observed in Fig. 5.12, where the elastic wave reaches the outer surface of the disk at the time $\hat{t} = 1$. Moreover, as illustrated in this figure, under the propagating longitudinal elastic waves, in addition to changing the outer radius, the thickness of the disk also expands and contracts, which is known as the *Poisson effect*. This effect can be only detected through the 3D solution of the problem which is of capabilities of the 1D FE-CUF models. It may be further seen that during the wave propagation and before the wave front reaches the outer surface of the disk, although the thickness is changing, the disk does not expand in the radial direction.

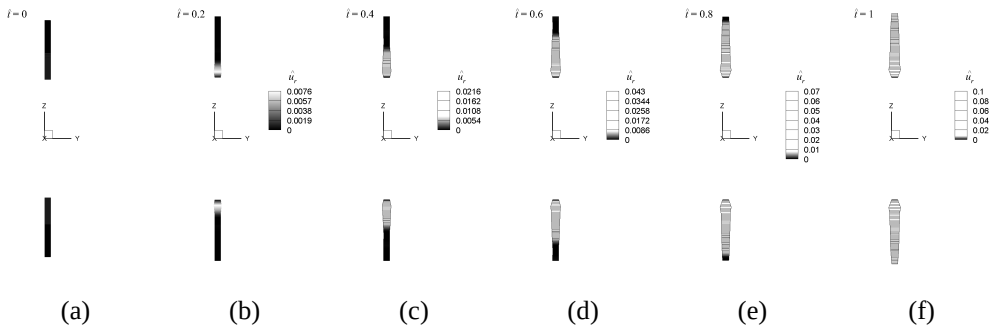

(a) (b) (c) (d) (e) (f)

Fig. 5.12 Distribution of nondimensional radial displacement for different values of the time.

Figure 5.13 shows distributions of the radial displacement, after the reflection of the elastic wave from the outer boundary, at the times $\hat{t} = 1.2, 2.7, 4.6, 6.5, 8.5$ and 10.5. In addition, to clarify how the thickness of the disk changes along the time, the percent change in the thickness at the mid-radius, named mid-thickness, is shown in Fig. 5.14. It may be seen from Fig. 5.13 that due to destruction of the wave front after the time $\hat{t} = 1$, the displacement gradient along the radius becomes smooth. Moreover, after the incidence of the wave on the outer surface to the time $\hat{t} = 2.7$, the disk begins to expand radially, and since the inner surface of the disc is assumed to be completely constrained, the outer radius of the disk increases.

As observed from Figs 5.13 and 5.14, after the wave reflection toward the inner surface, although the disk is radially expanding, the thickness at the mid-radius increases up to the time $\hat{t} = 1.2$. Then, with the increase of the outer radius, the mid-thickness decreases so that at the time $\hat{t} = 2.7$, the disk reaches the maximum expansion in the radial direction, while the mid-thickness reduces to about the initial value. After the time $\hat{t} = 2.7$, while the disk contracts radially to the time $\hat{t} = 4.6$, the mid-thickness increases. These deformations continue in a harmonic form along the time, because the equations of motion (see Eq. (**??**)) represent harmonic solutions for the displacements when the temperature is damped.

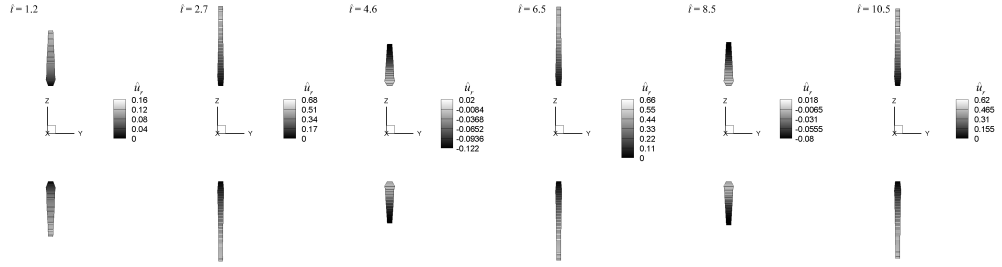

(a) (b) (c) (d) (e) (f)

Fig. 5.13 Distribution of nondimensional radial displacement for different values of the time.

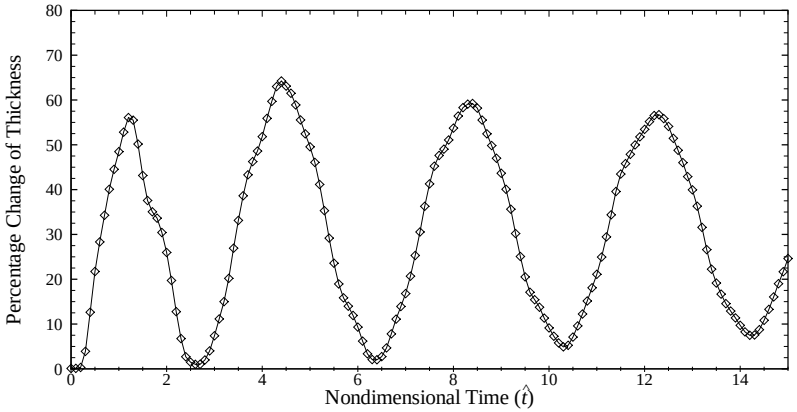

Fig. 5.14 Percentage change of thickness at the mid-radius of the plate along the time

5.2.2 Non-axisymmetric disk

To demonstrate the ability of the 1D FE-CUF models to provide 3D solutions of asymmetric problems, an annular disk with asymmetric boundary conditions can be analyzed. The geometry and material properties of the disk are considered to be the same as those of the previous example. The inner surface of the disk is assumed to be partially fixed in accordance with Fig. 5.15, while the other surfaces are stress free. As the thermal boundary conditions, the temperature change on the inner surface is equal to zero and two side surfaces of the disk are thermally insulated. Likewise, on the outer surface the temperature with respect to the reference temperature is suddenly changed by the function $T(t) = T_d(1 - e^{-tV_e/l})$ which, using the nondimensional parameters (4.43), can be expressed as $\hat{T} = 1 - e^{-\hat{t}}$.

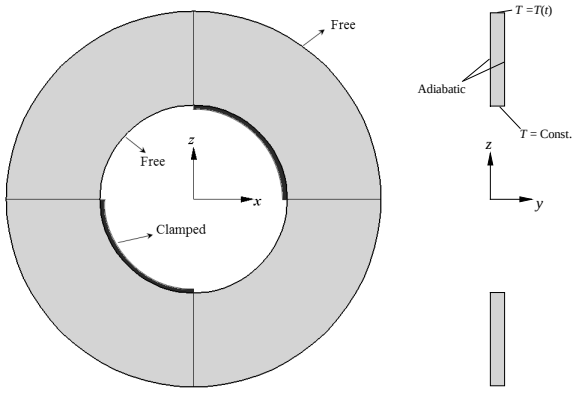

(a) (b)

Fig. 5.15 Boundary conditions (BCs) in the asymmetric disk (a) Mechanical BCs; (b) Thermal BCs.

Considering the model 1 B2/(6×18) L9 of the disk and based on the LS generalized theory of thermoelasticity, Figs. 5.16 and 5.17 show contour plots of the nondimensional temperature change and radial displacement distributions on the deformed model at different values of the time. Moreover, for further clarification, the time histories of the temperature change and radial displacement at the points $(\hat{x} = 1.06, \hat{y} = 0.05, \hat{z} = 1.06)$ and $(\hat{x} = -1.06, \hat{y} = 0.05, \hat{z} = 1.06)$ located on the mid-radius of the model are plotted in Fig. 5.18.

It may be seen in Figs. 5.16 and 5.17 that the elastic wave reaches the inner surface of the disk at the time $\hat{t} = 1$. After the incidence of the wave on the inner surface,

due to asymmetry of the mechanical boundary conditions, the displacement waves reflect asymmetrically from the boundary which causes the asymmetric deformations of the disk. Therefore, after the elastic wave reflection, the distribution of the temperature change on the deformed model is not axisymmetric as well. It is further observed from Fig. 5.18 that the amplitudes of oscillations of the displacement in the first quarter of the disk are smaller than those in the second quarter, however the frequency of these oscillations in the first quarter is higher than that in the second quarter. The reason is that the stiffness of the first quarter of the disk is larger due to its constrained inner surface.

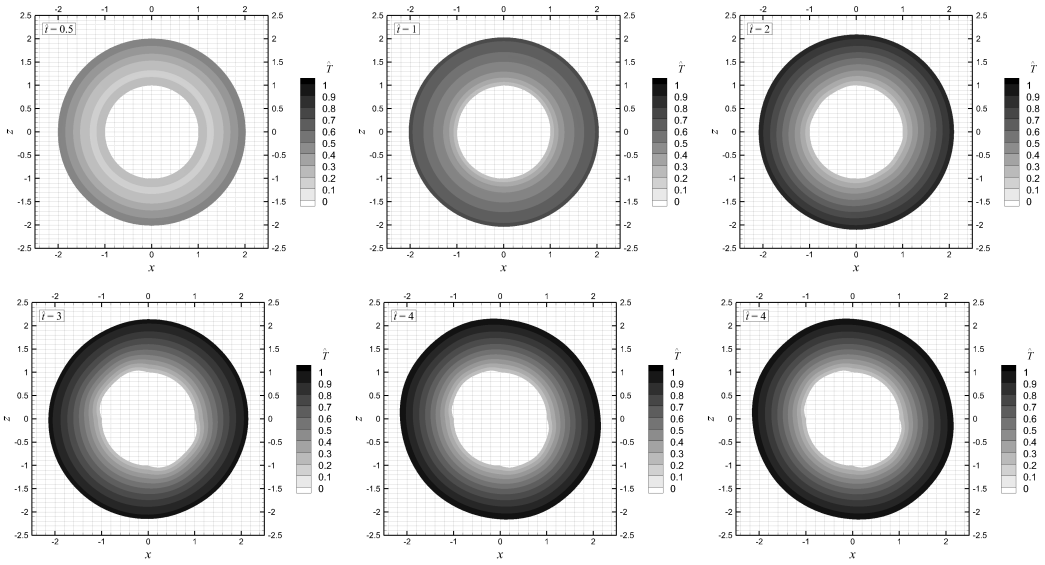

Fig. 5.16 Distribution of the nondimensional temperature change at different values of the time.

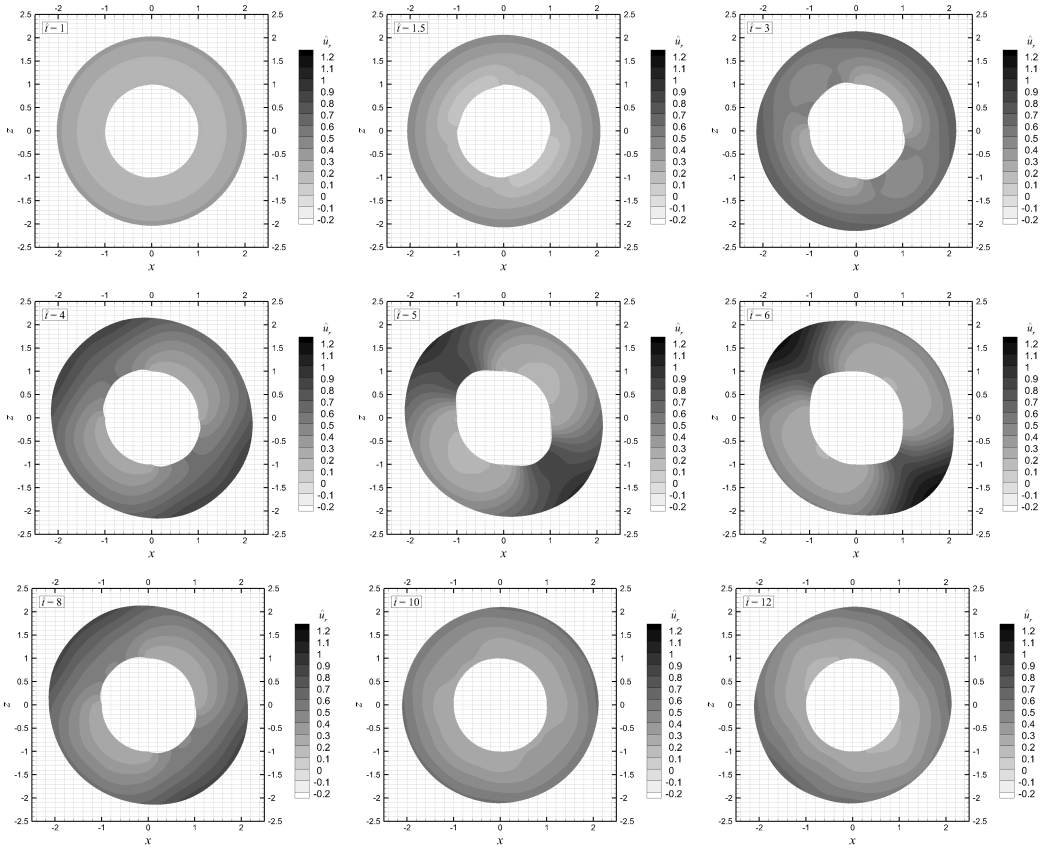

Fig. 5.17 Distribution of the nondimensional radial displacement at different values of the time.

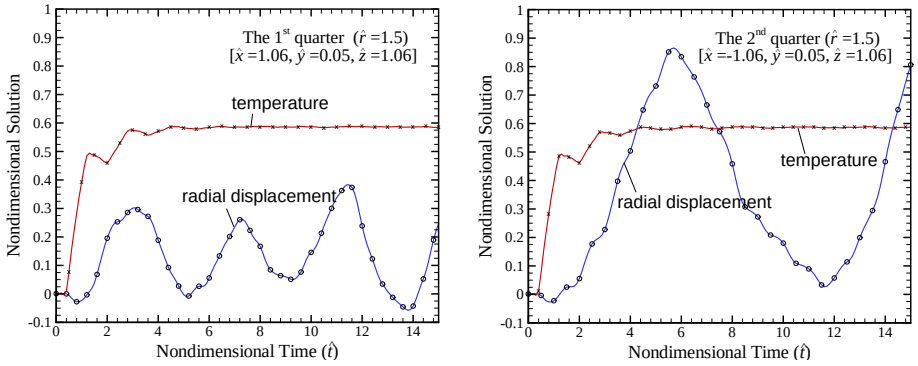

(a) (b)

Fig. 5.18 Time history of the nondimensional temperature change and radial displacement at mid-radius of the disk in the first (a) and the second (b) quarters .

5.3 Summary

The 1D FE-CUF approach developed in the chapter 4 has been validated through comparisons with available reference solutions considering static, quasi-static, and dynamic thermoelastic analyses. Simulations have been performed on isotropic and homogeneous structures. Comparison of the obtained results with the results reported in the literature verifies accuracy of the models for the disk problem. Indeed, as expected, the accuracy given by the 1D CUF models is extremely subordinate to the order of the Lagrange-type expansions. It was demonstrated that the FE-CUF models are quite efficient and have a very high rate of convergence, so that making use of an appropriate discretization, they are able to provide results with analytical accuracy. The propagation of thermoelastic waves and their reflection from the boundaries in an axisymmetric and asymmetric disk problem were investigated and it was shown that the Poisson effect can be detected in the 3D solution obtained by the models. It is hence concluded that the 1D FE-CUF approach can be effectively used to obtain 3D solution of the coupled thermoelastic problems in disks subjected to arbitrary boundary and loading conditions including the the body force and the heat source.

Chapter 6

Conclusion

The main subject of this dissertation has been to study of the coupled thermoelastic behaviors in rotating disks subjected to thermal loads. For this purpose, firstly, using an analytical procedure based on the Fourier-Bessel transform, the generalized coupled thermoelasticity problems in an axisymmetric rotating disk with constant thickness made of a homogeneous isotropic material are analytically solved. Then, closed-form formulations are presented for temperature and displacement fields.
Secondly, a 1D FE methodology refined through the Carrera unified formulation (1D FE-CUF) has been developed for the static uncoupled thermoelastic and the dynamic coupled thermoelastic analyses of structures made of nonhomogeneous anisotropic materials. In the unified FE formulation, indeed, addition to taking into account the mechanical damping effect, six theories of thermoelasticity, including coupled generalized (Green-Lindsay and Lord-Shulman) and classical theories as well as uncoupled dynamic, quasi-static and static theories, can be involved. The thermal and mechanical boundary conditions, the body force and the heat source are considered in the most general forms where no limiting assumption is applied. This generality allows to analyze varieties of more practical thermoelastic problems. Furthermore, The enhanced capabilities of 1D FE-CUF approach allowed to deal with problems that usually require sophisticated solutions with a low number of degrees of freedom. The validity and capabilities of the numerical procedure and convergence of results have been investigated in a number of numerical examples.
The obtained analytical and numerical solutions are in good agreement with the reference solutions. It is further shown that the proposed analytical and FE methods are quite efficient with very high rate of convergence. Distributions and time his-

tories of temperature, displacements and stresses, propagation of the thermoelastic waves, the wave reflection from the boundaries are shown and discussed. In addition, effects of coupling parameter, relaxation time on temperature, displacement and stress fields are investigated. Likewise, using the FE models, the solutions have been represented as contour plots to highlight 3D capabilities of the models.

6.1 Outline and contribution to the literature

The results obtained from the solution of the coupled thermoelasticity problems in disks can be outlined as:

- Before reaching the steady state condition, the transient displacement and stresses may be higher than the steady state. Therefore, for specialized applications involving sudden temperature changes in short periods of time, the disk should be designed with consideration of transient effects.
- Due to the presence of the thermoelastic damping parameter (coupling parameter) in heat conduction equation, the time history of the temperature is damped faster than the time history of the radial displacement.
- With increasing relaxation time, the maximum value of the curves of time histories of temperature and displacement increases, but occur at later times due to the decrease in the propagation speed of thermal waves.
- Comparison between different theories of thermoelasticity shows that under thermal shock loading, generalized coupled theory based on Lord–Shulman model predicts larger temperature and stresses compared to the other theories. Therefore, for specialized applications involving sudden temperature changes in short periods of time, the disk should be designed using some modified coupled thermoelasticity models with the finite speed of wave propagation such as Lord-Shulman (LS).
- When the coupling parameter takes a greater value, the amplitudes of oscillations of temperature increase. The reason is that with increasing coupling (or damping) parameter, the conversion between the mechanical and thermal energies increases.

In addition, some general points on the 1D FE-CUF modeling of disks can be outlined as follows:

- The 1D FE method refined by the CUF can be effectively employed to analyze rotating disks with variable thickness and reduce the computational cost of 3D FE analysis without affecting the accuracy.
- Since the presented 1D CUF model is invariant with respect to the order of the beam theory in the finite element axial discretization, the model provides a unified formulation that can easily consider different higher-order theories where large bending loads are involved in the problem.
- Increasing beam elements along the axis of disks may not have significant effect on accuracy of results and only leads to more DOFs. Thus, an appropriate distribution and type of beam elements or discretizing of disk profile into a proper number of cross-sections can significantly lead to a reduction in computational costs. In fact, the 1D FE model of a rotor should be selected so that it balance accuracy of results and DOFs reasonably compared to a similar solid model.
- To increase accuracy of a 1D CUF FE model along with optimized computational costs in a rotating disk problem, it would be preferable to tune a mesh refinement locally. Local refinements may be implemented straightforwardly through a finer mesh of elements on a cross-section of the disk where needed, for example, at vicinity of the problem boundaries.
- Since distribution refinements of LEs over a cross-section may cause computational costs to be increased, making use of higher-order Lagrange elements (like L9 and L16) can reduce DOFs, while preserving the accuracy.
- Due to quadratic interpolations in L9 element, the rate of convergence of L9 is higher than L4 element in which bilinear polynomials are used as interpolation functions of displacement field. Therefore, increasing numbers of L4 elements on a cross section can be effective in improving accuracy of the solution.
- A refinement of LEs along the radial direction is more effective than one in the circumferential direction. In other words, increase of number of elements

along the radial direction, compared to circumferential direction, is more effective in improving the results.

- The innovative FE procedure presented in this dissertation can be used as an accurate tool of structural-thermal analysis for complex rotors with arbitrary configuration and loading conditions to reduce the computational costs in an iterative design phase of rotors as well as an iterative solution process of the dynamic coupled thermoelasticity problems.

6.2 Future works

Within this work, the FE-CUF approach has shown excellent performance in the study of the coupled thermoelastic behavior in rotors, therefore, as future work, it is of interests to extend the study to more complicated problems as follows

- Nonlinear thermoelasticity problems (geometrical as well as material nonlinearities).
- Dynamic analysis of rotors subjected to transient thermal prestresses.
- Study of thermoelastic damping effect on dynamic behaviors of rotors.

References

[1] Abbas, I. A. (2008). Finite element method of thermal shock problem in a non-homogeneous isotropic hollow cylinder with two relaxation times. *Forschung im Ingenieurwesen*, 72(2):101–110.

[2] Abbas, I. A. (2012). Finite element analysis of the generalized thermoelastic interactions in an elastic half space subjected to a ramp-type heating. *Journal of Physics*, 1(2):3–9.

[3] Babaei, M. H., Abbasi, M., and Eslami, M. R. (2008). Coupled thermoelasticity of functionally graded beams. *Journal of Thermal Stresses*, 31(8):680–697.

[4] Bagri, A. and Eslami, M. (2004). Generalized coupled thermoelasticity of disks based on the lord–shulman model. *Journal of Thermal Stresses*, 27(8):691–704.

[5] Bagri, A., Eslami, M., and Samsam-Shariat, B. (2006). Generalized coupled thermoelasticity of functionally graded layers. In *ASME 8th Biennial Conference on Engineering Systems Design and Analysis*, pages 435–440. American Society of Mechanical Engineers.

[6] Bagri, A. and Eslami, M. R. (2007). Analysis of thermoelastic waves in functionally graded hollow spheres based on the green-lindsay theory. *Journal of Thermal Stresses*, 30(12):1175–1193.

[7] Bakhshi, M., Bagri, A., and Eslami, M. (2006). Coupled thermoelasticity of functionally graded disk. *Mechanics of Advanced Materials and Structures*, 13(3):219–225.

[8] Bargmann, H. (1974). Recent developments in the field of thermally induced waves and vibrations. *Nuclear Engineering and Design*, 27(3):372–385.

[9] Bathe, K. (1996). Finite element procedure. *Prentice hall*.

[10] Biot, M. A. (1956). Thermoelasticity and irreversible thermodynamics. *Journal of Applied Physics*, 27(3):240–253.

[11] Boley, B. A. and Weiner, J. H. (1960). *Theory of Thermal Stresses*. Wiley, New York.

[12] Bonello, B., Perrin, B., Romatet, E., and Jeannet, J. (1997). Application of the picosecond ultrasonic technique to the study of elastic and time-resolved thermal properties of materials. *Ultrasonics*, 35(3):223–231.

[13] Cannarozzi, A. A. and Ubertini, F. (2001). A mixed variational method for linear coupled thermoelastic analysis. *International Journal of Solids and Structures*, 38(4):717–739.

[14] Carrera, E., Brischetto, S., and Nali, P. (2011a). *Plates and Shells for Smart Structures: Classical and Advanced Theories for Modeling and Analysis*. Wiley.

[15] Carrera, E., Cinefra, M., Petrolo, M., and Zappino, E. (2014a). *Finite Element Analysis of Structures through Unified Formulation*. Wiley.

[16] Carrera, E., Cinefra, M., Petrolo, M., and Zappino, E. (2014b). *Finite Element Analysis of Structures through Unified Formulation*. Wiley.

[17] Carrera, E., Giunta, G., and Petrolo, M. (2011b). *Beam Structures: Classical and Advanced Theories*. Wiley.

[18] Carrera, E. and Petrolo, M. (2012). Refined one-dimensional formulations for laminated structure analysis. *AIAA journal*, 50(1):176–189.

[19] Carter, J. P. and Booker, J. R. (1989). Finite element analysis of coupled thermoelasticity. *Computers & Structures*, 31(1):73–80.

[20] Chakraborty, A. and Gopalakrishnan, S. (2004). Thermoelastic wave propagation in anisotropic layered media-a spectral element formulation. *International Journal of Computational Methods*, 1(03):535–567.

[21] Chakraborty, A., Gopalakrishnan, S., and Reddy, J. N. (2003). A new beam finite element for the analysis of functionally graded materials. *International Journal of Mechanical Sciences*, 45(3):519–539.

[22] Chen, H. T. and Lin, H. J. (1995). Study of transient coupled thermoelastic problems with relaxation times. *Journal of applied mechanics*, 62(1):208–215.

[23] Chen, T. C. and Weng, C. I. (1988). Generalized coupled transient thermoelastic plane problems by laplace transform/finite element method. *Journal of applied mechanics*, 55(2):377–382.

[24] Chopra, A. K. (1995). *Dynamics of Structures*, volume 3. Prentice Hall, New Jersey.

[25] Cinelli, G. (1965). An extension of the finite hankel transform and applications. *International Journal of Engineering Science*, 3(5):539–559.

[26] Darabseh, T., Yilmaz, N., and Bataineh, M. (2012). Transient thermoelasticity analysis of functionally graded thick hollow cylinder based on green–lindsay model. *International Journal of Mechanics and Materials in Design*, 8(3):247–255.

[27] Duhamel, J. M. (1837). Second memoire sur les phenomenes thermomecaniques. *J. de l'E "cole Polytechnique*, 15(1).

[28] Durbin, F. (1974). Numerical inversion of laplace transforms: an efficient improvement to dubner and abate's method. *The Computer Journal*, 17(4):371–376.

[29] Emami, A. and Alibeigloo, A. (2016). Exact solution for thermal damping of functionally graded timoshenko microbeams. *Journal of Thermal Stresses*, 39(2):231–243.

[30] Eslami, M. (2014). *Finite Elements Methods in Mechanics*. Springer International Publishing.

[31] Eslami, M. and Salehzadeh, A. (1987). Application of galerkin method to coupled thermoelasticity problems. In *Proc. of the 5th International Modal Analasis Conference*, London.

[32] Eslami, M. and Vahedi, H. (1992). Galerkin finite element displacement formulation of coupled thermoelasticity spherical problems. *Journal of pressure vessel technology*, 114(3):380–384.

[33] Eslami, M. R., Shakeri, M., and Sedaghati, R. (1994). Coupled thermoelasticity of an axially symmetric cylindrical shell. *Journal of Thermal Stresses*, 17(1):115–135.

[34] Eslami, M. R. and Vahedi, H. (1989). Coupled thermoelasticity beam problems. *AIAA Journal*, 27(5):662–665.

[35] Farhat, C., Park, K. C., and Dubois-Pelerin, Y. (1991). An unconditionally stable staggered algorithm for transient finite element analysis of coupled thermoelastic problems. *Computer Methods in Applied Mechanics and Engineering*, 85(3):349–365.

[36] Filopoulos, S. P., Papathanasiou, T. K., Markolefas, S. I., and Tsamasphyros, G. J. (2014). Generalized thermoelastic models for linear elastic materials with micro-structure part i: Enhanced green–lindsay model. *Journal of Thermal Stresses*, 37(5):624–641.

[37] Fujino, T. and Ohsaka, K. (1968). The heat conduction and thermal stress analysis by the finite element method. In *Proc. 2nd Conf. Matrix Methods Struct. Mech.*, pages 1121–1164. Wright-Patterson AFB Ohio.

[38] Guo, P., Wu, W.-H., and Wu, Z.-G. (2013). A time discontinuous galerkin finite element method for generalized thermo-elastic wave analysis, considering non-fourier effects. *Acta Mechanica*, 225(1):299–307.

[39] Hetnarski, R. (1964). The fundamental solution of the coupled thermoelastic problem for small times. *Arch. Mech. Stosow*, 16:23–31.

[40] Hetnarski, R. and Ignaczak, J. (2016). *The Mathematical Theory of Elasticity, Second Edition*. CRC Press.

[41] Hetnarski, R. B. and Eslami, M. R. (2009). *Thermal Stresses-Advanced Theory and Applications*, volume 158. Springer, New York.

[42] Hosseini, S. M. and Abolbashari, M. H. (2012). Analytical solution for thermoelastic waves propagation analysis in thick hollow cylinder based on green–naghdi model of coupled thermoelasticity. *Journal of Thermal Stresses*, 35(4):363–376.

[43] Hosseini Zad, S. K., Komeili, A., Eslami, M. R., and Fariborz, S. (2011). Classical and generalized coupled thermoelasticity analysis in one-dimensional layered media. *Archive of Applied Mechanics*, 82(2):267–282.

[44] Hostetler, J., Smith, A., and Morris, P. (1998). Simultaneous measurement of thermophysical and mechanical properties of thin films. *International journal of thermophysics*, 19(2):569–577.

[45] Ignaczak, J. and Ostoja-Starzewski, M. (2009). *Thermoelasticity with Finite Wave Speeds*. OUP Oxford.

[46] Jafarinezhad, M. and Eslami, M. (2017). Coupled thermoelasticity of fgm annular plate under lateral thermal shock. *Composite Structures*.

[47] Kant, S. and Mukhopadhyay, S. (2016). An investigation on coupled thermoelastic interactions in a thick plate due to axi-symmetric temperature distribution under an exact heat conduction with a delay. *International Journal of Thermal Sciences*, 110:159–173.

[48] Li, Y., Ghoneim, H., Chen, Y., and Davis, J. (1983). A numerical method in solving a coupled thermoelasticity equation and some results. *Journal of Thermal Stresses*, 6(2-4):253–280.

[49] Li, Z., Ma, Q., and Cui, J. (2016). Finite element algorithm for dynamic thermoelasticity coupling problems and application to transient response of structure with strong aerothermodynamic environment. *Communications in Computational Physics*, 20(03):773–810.

[50] Liu, W. and Chang, H. (1985). Unconditionally stable implicit-explicit algorithms for dynamic coupled thermoelasticity. *J. Appl. Mech*, 52:483–485.

[51] Manson, S. (1947). *Determination of elastic stresses in gas-turbine disks*. National Advisory Committee for Aeronautics.

[52] Nickell, R. and Sackman, J. (1968). Variational principles for linear coupled thermoelasticity. *Quarterly of Applied Mathematics*, 26(1):11–26.

[53] Papathanasiou, T. K., Gourgiotis, P. A., and Dal Corso, F. (2016). Finite element simulation of a gradient elastic half-space subjected to thermal shock on the boundary. *Applied Mathematical Modelling*, 40(23):10181–10198.

[54] Prevost, J. H. and Tao, D. (1983). Finite element analysis of dynamic coupled thermoelasticity problems with relaxation times. *Journal of Applied Mechanics*, 50(4a):817–822. 10.1115/1.3167151.

[55] Reddy, J. and Chin, C. (1998). Thermomechanical analysis of functionally graded cylinders and plates. *Journal of Thermal Stresses*, 21(6):593–626.

[56] Reddy, J. N. (2004). *Mechanics of laminated composite plates and shells. Theory and Analysis*. CRC Press, 2^{nd} edition.

[57] Shahani, A. R. and Bashusqeh, S. M. (2013). Analytical solution of the coupled thermo-elasticity problem in a pressurized sphere. *Journal of Thermal Stresses*, 36(12):1283–1307.

[58] Sherief, H. H. and Ezzat, M. A. (1994). Solution of the generalized problem of thermoelasticity in the form of series of functions. *Journal of thermal stresses*, 17(1):75–95.

[59] Tamma, K. K. and Namburu, R. R. (1992). An effective finite element modeling/analysis approach for dynamic thermoelasticity due to second sound effects. *Computational mechanics*, 9(2):73–84.

[60] Tian, X. and Shen, Y. (2005). Study on generalized magneto-thermoelastic problems by fem in time domain. *Acta Mechanica Sinica*, 21(4):380–387.

[61] Tsai, S. W. (1988). *Composites Design*. Dayton, Think Composites, 4th edition.

[62] Ugural, A. C. and Fenster, S. K. (2003). *Advanced strength and applied elasticity*. Pearson Education.

[63] Vullo, V. and Vivio, F. (2013). *Rotors: Stress analysis and design*. Springer Science & Business Media.

[64] Wilson, E. L. and Nickell, R. E. (1966). Application of the finite element method to heat conduction analysis. *Nuclear Engineering and Design*, 4(3):276–286.

[65] Zenkour, A. M. and Abbas, I. A. (2014). A generalized thermoelasticity problem of an annular cylinder with temperature-dependent density and material properties. *International Journal of Mechanical Sciences*, 84:54–60.

[66] Zhu, X., Villeneuve, D., Naumov, A. Y., Nikumb, S., and Corkum, P. (1999). Experimental study of drilling sub-10 μm holes in thin metal foils with femtosecond laser pulses. *Applied Surface Science*, 152(3):138–148.